December 2019

Graphene Based Ion Sensitive Field Effect Transistor for K+ Ion Sensing

Hongmei Li
Clemson University, lihongmei510@gmail.com

GRAPHENE BASED ION SENSITIVE FIELD EFFECT TRANSISTOR FOR K+ ION SENSING

A Dissertation
Presented to
the Graduate School of
Clemson University

In Partial Fulfillment
of the Requirements for the Degree
Doctor of Philosophy
Electrical and Computer Engineering

---

by
Hongmei Li
December 2019

Accepted by:
Dr. Goutam Koley, Committee Chair
Dr. W. Rod Harrell
Dr. Apparao M. Rao
Dr. Pingshan Wang

ABSTRACT

Graphene, discovered in 2004, has drawn great interest in the wide range of applications due to its distinctive 2-dimensional material property. Sensing is the one application has been developed extensively owing to graphene's ultra-high mobility, low electric noise, very high surface-to-volume ratio, and easy modulation of electrical characteristics. With these excellent properties, the present research explored graphene's ion sensing potential with the goal of developing graphene-based K^+ ion detector which can be applicable in implantable bio-sensors. As the major intracellular cation, potassium has very critical functions in various biological processes. Additionally, recent research found out that elevations in biological levels of K^+ ions precede the onset of sudden cardiac death, epileptic seizures, and other clinical problems. Therefore, the development of implantable K^+-sensitive sensor devices could be of great use in predicting the onset of those time-sensitive condition breakouts in medical applications.

To synthesize high quality graphene to investigate graphene's property and explore its ion sensing capability, a CVD system was built in the lab along with an automatic control program that can both control and monitor the synthesis process. Characterization was carried out with various tools (AFM, Raman spectroscopy, Hall measurement and etc.) and the results confirmed that the obtained graphene is high quality mono-layer graphene.

In order to have a deeper insight into graphene's sensing mechanism, graphene's interactions with typical donor/ acceptor gas molecules and strong donor molecules were investigated by observing its three important electrical properties – carrier mobility, carrier density, and sheet conductivity change upon molecular adsorption. From the investigation,

an empirical model was proposed to explain an interesting trend of graphene's transport property changes during its molecular interactions. On the other hand, an advanced surface functionalization method was developed to greatly enhance graphene's molecular sensing performance. A light oxygen plasma treatment can boost graphene's electrical response to NH_3 molecules both in response magnitude and response time. A systematic analysis was carried out and found an optimum power of oxygen plasma can induce a surface functionalization caused by graphene crystal grain size nano crystallization and oxygen species p-doping effect.

Graphene-based ion sensitive field effect transistors (GISFETs) with high sensitivity and selectivity for K^+ ion detection was demonstrated utilizing valinomycin based ion selective membrane. The performance of the GISFETs was studied in various media over a concentration range of 1 μM – 2 mM. The sensitivity of the sensor was found to be >60 mV/decade, which is comparable to the best Si-based commercial ISFETs, with negligible interference found from Na^+ and Ca^{2+} ions in high concentration. The performance of the sensor also remained unchanged when fabricated on a flexible and biocompatible PET substrate.

The sensor performance did not change significantly in Tris–HCl solution or with repeated testing over a period of two months highlighting its reliability and effectiveness for physiological monitoring. From Real-cell based extracellular K^+ ion assay, the GISFET sensor demonstrated good detecting performance confirmed the possibility of using in implantable bio sensing application. Additionally, GISFET sensor arrays fabricated using CMOS compatible technique also showed the same sensing performance which proves

mass production capability in the future. At the same time, graphene based ion sensitive diode (G-ISDiode) was also developed using graphene/silicon Schottky junction. Because of the exponential relation between diode current and graphene's Fermi level, the G-ISDiode sensor demonstrated an exponential sensing performance in ionic detection. This is different from G-ISFET's linear response to ion concentration, which can be a big advantage in certain applications where demand ultra-high sensitivity.

ACKNOWLEDGMENTS

First and foremost, I would like to express my deepest gratitude to my advisor, Dr. Goutam Koley, for his excellent guidance, insightful advice, and persistent encouragement during my doctoral program. His immense knowledge and enthusiasm always motivated me and have made me a better scientist and researcher. I am grateful as well to my dissertation committee members, Dr. Apparao Rao, Dr. Pingshan Wang, and Dr. Rod Harrell, for the time and effort they put into my research work.

I also appreciate Dr. Rao for allowing me to use the Raman spectroscopy, and also thanks to Anthony Childress and Sai Sunil Mallineni from Dr. Rao's group for assisting me with the Raman system. Also, I acknowledge Dr. Kenneth Walsh at the University of South Carolina for the collaboration in the living cell related research. I thank Dr. Chuanbing Tang group at the University of South Carolina for the collaboration in polymer matrix development.

A big thanks also go to cleanroom manager Bill Delaney and staff at AMRL and the ECE department especially Wendy Baldwin, Robert Hammett and Gale Black who was always ready to help me out over the years.

Financial support from the National Science Foundation (Grants Nos. IIP-1512342, CBET-1606882, and IIP-1602006) for the research is also thankfully acknowledged.

I would also like to thank all of my colleagues at NESL, both present and past, for supporting and assisting my study and research. Particularly, I thank Ahsan and Amol for helping me out with setting up CVD system and sharing with me their valuable research experience. Also, I thank Digangana and Ferhat, for being always very supportive and

around when needed. I also thank those undergraduate interns who once worked on my projects, especially Ryan Lemert-Smith and John Hardaway who greatly contributed to building automatic control systems for processing, measurement equipment.

Finally, I would like to express my love and gratitude to my husband Nan Xing, to my parents and my sister for their endless love, patience and encouragement when it was most required.

TABLE OF CONTENTS

Page

Table of Contents (Continued)

Page

LIST OF TABLES

LIST OF FIGURES

List of Figures (Continued)

Figure Page

List of Figures (Continued)

Figure Page

List of Figures (Continued)

Figure Page

List of Figures (Continued)

Figure Page

List of Figures (Continued)

Figure Page

List of Figures (Continued)

Figure Page

CHAPTER ONE

INTRODUCTION

Graphene is a single layer of carbon atoms arranged in a two-dimensional honeycomb shape in which one atom forms each vertex. It was discovered in 2004 for the first time by Geim and Novoselov at Manchester University, isolated from graphite in a micromechanical cleavage process called Scotch tape technique. This simple yet effective graphene isolation technique yielded access to extensive research on graphene, which followed with abundant interesting physical discovery in electronic, mechanical, optical, and quantum properties. Also, due to the pioneering research on graphene, Geim and Novoselov were awarded the 2010 Nobel Prize in Physics "for groundbreaking experiments regarding the two-dimensional material graphene." Later on, graphene's distinctive material property has drawn great interest in the wide range of application development, as a result, a variety of potential applications have been explored and investigated. Generally, its applications can be sorted in several fields such as sensor application, thermally or electrically conductive reinforced composite materials and related components, and high-speed and radio frequency logic devices. Among its various applications, this dissertation will investigate and demonstrate graphene's ion sensing application including its chemical sensing mechanisms and its ion sensor's potential for applying in the state-of-art medical devices in the future. Chapter one will start with the introduction of graphene's material properties and sensing applications.

1.1 Unique Material Properties of Graphene

1.1.1 Graphene's Atomic Structure

Graphene is a single layer of carbon atoms tightly arranged in a hexagonal structure, as shown in Fig. 1.1(Left). Carbon atoms are bonded in sp^2 hybridization C-C bond with a bond length of 1.42 Å. The real-space atomic resolution images are available via scanning tunneling microscopy (STM), as shown in Fig. 1.1 (Right), from where a clear hexagonal

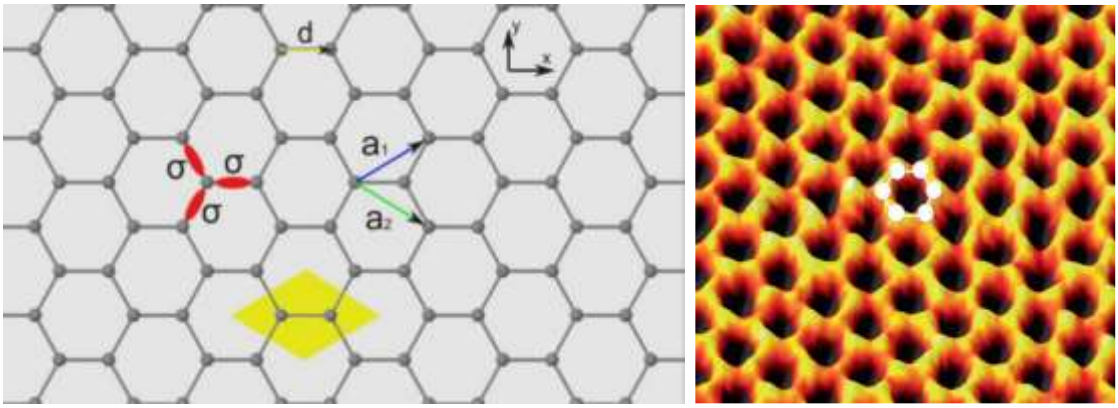

Figure 1.1 (Left) The atomic structure of a graphene surface where a_1, a_2 are lattice vectors, d is the vector joining the two atoms in the unit cell and σ are the sp^2-hybridized bonds that allow for the covalent bonding between neighboring atoms. The unit cell is highlighted in yellow. [2] (Right) Atomic resolution real-space images of single-layer graphene on SiO_2 substrates taken via scanning tunneling microscopy (STM).[1]

shape atomic structure can be seen. [1] Although graphene isolation from graphite was possible only until recently, graphite has been known as a naturally occurring mineral for nearly 500 years. Its weak dispersion forces between layers were utilized to make marking instruments (like pencils), and also adopted as a dry lubricant. There are two materials also possess similar structure like graphite, also used as dry lubricants with higher cost. They are hexagonal boron nitride (h-BN) and molybdenum disulfide (MoS_2). After graphene's

discovery, the two materials have also drawn a lot of interest on the way of exploring graphene's application. Mostly investigated to develop full 2-D material devices (h-BN is a good dielectric with 5.2 eV bandgap, MoS_2 as semiconductor 1.23 eV bandgap), or apply them as substrates of graphene which can bring different or exact lattice matching with graphene. Furthermore, graphene brought up various sp^2 bonds based carbon allotrope nano-systems: fullerenes are spherical molecules owing to pentagon working as curvature defects in a planar system (0D), carbon nanotubes (CNTs) are cylindrical nanostructure from rolled up graphene in a given direction then reconnected carbon bonds at the edge (1D), graphene nanoribbons (GNRs) are strips of graphene with width less than 50 nm. Each of them has attractive and unique physical, electronic, optical properties and related applications that have led to extensive research work. Conceptually considered as the parent material for most of the allotropes of carbon, the knowledge of graphene's electronic structure is essential for understanding their physical and chemical properties.

From the atomic structure of a graphene surface shown in Fig. 1.1 (Left), $\boldsymbol{a_1}, \boldsymbol{a_2}$ are lattice vectors, d is the vector joining the two atoms in the unit cell, and σ is the sp^2-hybridized bonds that allow for the covalent bonding between neighboring atoms. The unit cell is highlighted in yellow, there are two carbon atoms per unit cell in graphene. The primitive basis vectors $\boldsymbol{a_1}, \boldsymbol{a_2}$ are given by Equation 1.1, where a is the in-plane lattice constant, with a value shown in Equation 1.2. [2]

$$\boldsymbol{a_1} = \frac{a}{2}\left(\sqrt{3}, 1\right), \quad \boldsymbol{a_2} = \frac{a}{2}\left(\sqrt{3}, -1\right) \tag{1.1}$$

$$a = \sqrt{3}\, d \cong 2.46 \text{ Å} \tag{1.2}$$

A brief discussion on the bonding process of the graphene structure can give a better insight into its many significant properties. Each carbon atom has a total of 6 electrons with the configuration of $1s^2 2s^2 2p^2$ – two valence electrons in the 2s subshell and two in the 2p subshell. By energetically favorable, just a small excitation can promote an electron in the 2s subshell into the 2p subshell result in four orbitals ($2s^2$, $2p_x$, $2p_y$, $2p_z$) become exactly half full so they can form more strong covalent bonds, which therefore reduces the overall energy. In graphene, 2s orbital is combined with the $2p_x$ and $2p_y$ to form three sp^2 orbitals in one plane, separated by a bond angle of 180°. These sp^2 orbitals of each carbon then bond with the adjacent sp^2 orbital forming three strong covalent σ bonds. They primarily lie along the graphene plane and their strong covalent bonds between neighboring C atoms are responsible for the extremely high mechanical stability of graphene (see Figure 1.2). However, σ bonds do not contribute much to the graphene's electrical characteristics because their energies are too far away from the Fermi level. [2]

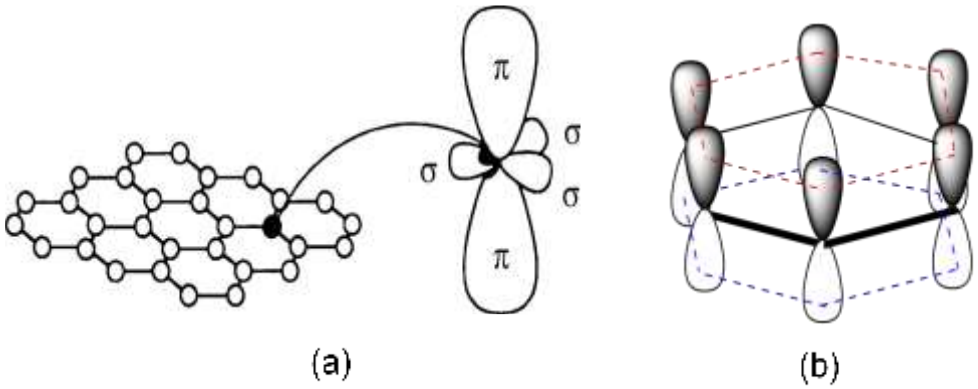

Figure 1.2 (a) The carbon atomic σ and π orbitals in the sp^2 honeycomb lattice (b) π electrons delocalized around the ring, above and below the plane. [2,3]

While three electrons from $2s^2$, $2p_x$, $2p_y$ consisting three sp^2 orbitals and forming σ bonds, the remained p_z orbital does not take part in the sp^2 hybridization, instead it forms delocalized a figure of eight-like orbital in the plane perpendicular to the lattice surface. [3] This p_z orbital on each carbon overlaps with its three neighboring carbons to form a band of filled π band (known as the valence band), and a band of empty π* band (conduction band). These delocalized π electrons are responsible for many interesting characteristics of graphene. The π electrons' ability to freely moving between carbon atoms gives graphene the peculiarity or its high electrical conductivity. Also, it is responsible for graphene's low-energy electronic properties which is one of the most important qualities for sensing applications.

1.1.2 Energy Dispersion of π Electrons

The energy structures of crystals depend on the interactions between energy orbitals in the lattice. Also, with the tight binding approximation (TB), the interactions between

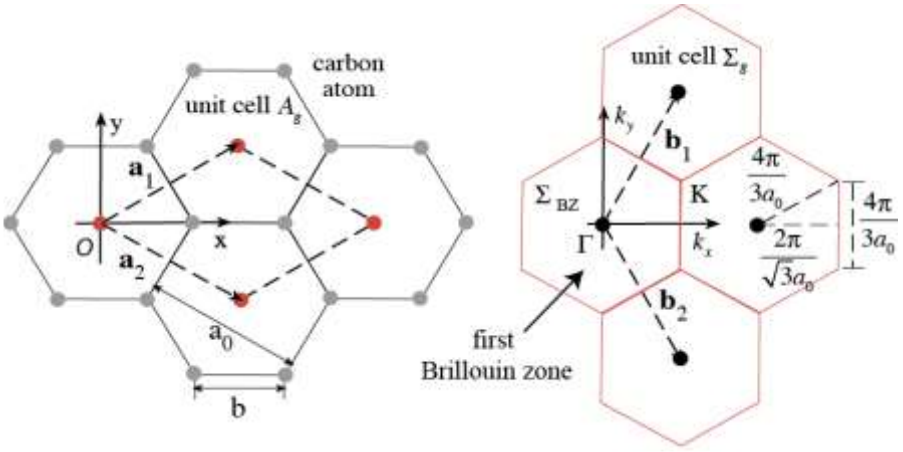

Figure 1.3 Structure of the graphene. (Left) Bravais lattice. (Right) Reciprocal lattice. [4]

atoms separated by large distances are neglected. In graphene, due to the calculation for the energy ranges of σ and π bands, only electrons in the π bond contribute to the electronic properties. Figure 1.3 shows graphene's Bravais lattice and reciprocal lattice. [4] The basic information of the Bravais lattice has discussed in the atomic structure introduction. In the reciprocal lattice (k-space), the graphene is spanned by the two vectors $\boldsymbol{b_1}, \boldsymbol{b_2}$ of length $b_0 = 4\pi/\sqrt{3}a_0$. In Figure 1.4, the energy dispersion of graphene for the first Brillouin zone

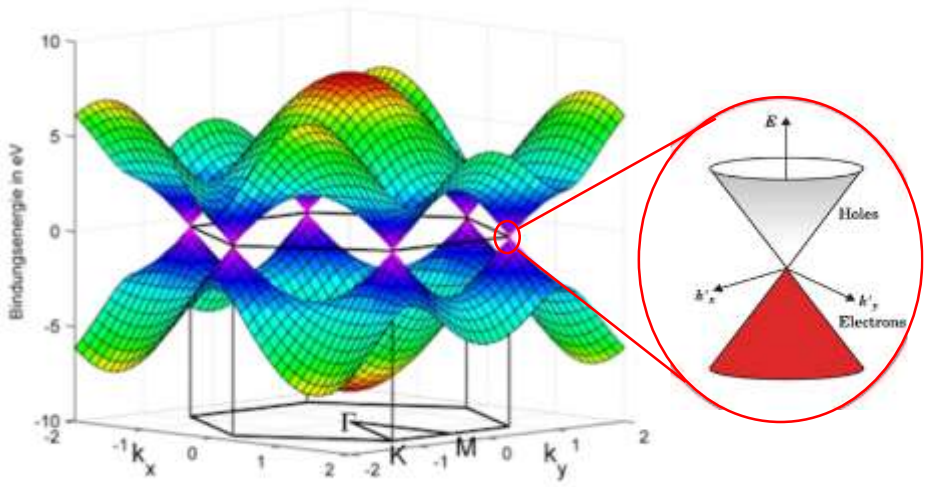

Figure 1.4 Energy dispersion of graphene around the Brillouin zone for the π and π* bands, in units of t. Inset shows energy dispersion of graphene close to the K and K′ points.

is depicted. The center of BZ (Brillouin zone) - Γ, six corners on each the conduction band and valence band meets - K, and the six points on the edge of the BZ at the center between K points - M can be found. The K point we also call it a Dirac point, that is where π band and π* band exactly touch at the Fermi level. This makes graphene a zero band-gap semiconductor. In particle physics, the electrons in graphene behave like Dirac massless chiral quasiparticles (relativistic fermions), in addition to the symmetric system of

graphene, they are described by the Dirac equation (for spin -1/2 particles) rather than the Schrodinger equation. With tight-binding Hamiltonian, the energy dispersion relation is given by Equation (1.3),

$$E(k_x, k_y) = \pm t \times \sqrt{1 + 4cos^2\left(\frac{k_y a}{2}\right) + 4cos\left(\frac{k_y a}{2}\right) cos\left(\frac{k_x\sqrt{3}a}{2}\right)} \quad (1.3)$$

where k_x, k_y are wavevector components along the *x, y* directions. According to Equation 1.3, we can know the valence band and conduction band meets at charge neutrality level at K, K′ points of the Brillouin zone. Near these Dirac points, in the low energy spectrum |E| < ~1 eV, the electron energy (E) depends linearly on the electron wave vector, with the following relation in Equation 1.4.

$$\boldsymbol{E_k} = v_F|\boldsymbol{k}| \quad (1.4)$$

In Equation 1.4, **k** is the wave-number and v_F is the Fermi velocity,

$$v_F \equiv \frac{3ta}{2\hbar} \approx \frac{c}{300} \approx 10^6\ m/s \quad (1.5)$$

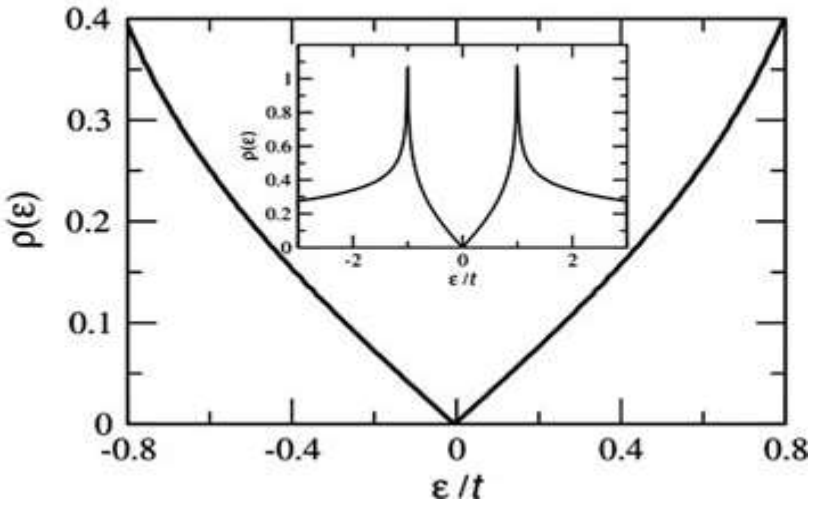

Figure 1.5 Density of state of graphene as a function of energy (in units of *t*) computed from energy dispersion. [6]

where t is a finite hopping amplitude ~2.8 eV, a is lattice constant ~1.42 Å. The Fermi velocity is independent of the carrier density behaves as an effective velocity of light. [5] Also derived from Hamiltonian, the density of states of graphene can be obtained as shown in Figure 1.5.[6] The linearity of the energy dispersion results in the vanishing of the density of states linearly at the Dirac points, at the Fermi level. This particular situation gives the benefit to the low noise electron transport. It inhibits instabilities, allows massless Dirac fermions immune to weak repulsive or attractive interactions whether long or short ranged.[7]

1.1.3 Graphene's Material Properties

With unique atomic and electronic structure, graphene has excellent mechanical, electrical, optical, and electrical transport properties. The properties are summarized in Table 1.1. Single layer graphene's thickness was measured to be ~3.7 Å using multi-parametric surface plasmon resonance, and this 2-dimensional material has been found out mechanically very strong and flexible.[8] The breaking strength of graphene is ~42 N/m, which is more than 100 times stronger than that of steel (with the corresponding Young's modulus of ~1.0 TPa).[9] In addition, graphene interacts strongly with light in a wide range of wavelengths. It shows 2.3% of light absorption per unit mass of the material, which is at least one (up to three) orders of magnitude higher than conventional semiconductor materials (Si, GaAs, etc.).[10] Graphene also revealed unusually high thermal conductivity, suspended single layer graphene experimentally proved to have a thermal conductivity in the range of 3,000 – 5,000 W/mK at room temperature (~36 times higher than Si and ~100 times higher than GaAs).[11] Good heat conduction is a desirable

property in low-dimensional materials to solve practical thermal management problems for future nanoelectronics. Another extraordinary electronic property of graphene for practical nanoelectronics, the breakdown current density is found to be on the order of 10^8 A/cm^2. [12] Furthermore, graphene has remarkably high carrier mobility that can be up to 200 000 cm^2/Vs in suspended configuration, it is more than 100 times higher than that of silicon. [13] A higher mobility of semiconductor always can bring a better device performance. As a typical characteristic for a 2-dimensional material, graphene has an extremely high surface-to-volume ratio, 2630 m^2/g, which is a big advantage for super capacitors, sensors, and devices that require high surface area.[14]

Table 1.1 Outstanding properties of graphene

Properties	Value	Ref.
Lattice constant	1.42 Å	[8]
Thickness	3.7 Å	[8]
Maximum current density	>10^8 A/cm	[12]
Thermal conductivity at room temperature	5000 W/mK	[11]
Breaking strength	42 N/m	[9]
Young's modulus	1.0 Tpa	[9]
Optical absorption coefficient	2.30%	[10]
Mobility (suspended)	200 000 cm^2/Vs	[13]
Specific surface area	2630 m^2/g	[14]

1.2 Graphene Sensors

Owing to graphene's outstanding material properties which have discussed in the previous section, it has a lot of promising application potentials. Its advanced applications have been developed in including but not limited to various sensors, bioengineering, graphene derivative materials, energy technology, and photonic technology. Among all of them, various sensing applications owing to its excellent mechanical property, chemical property, and optical property have attracted high interest in research.

1.2.1 Physical Sensors

Graphene has superior mechanical properties, has been reported to be the strongest materials ever tested. In addition to a high tensile modulus (stiffness) of 1 TPa, ~42 N/m breaking strength make graphene more than 100 times greater than that of steel. Also, it has a high spring constant in the range of 1 -5 N/m with Young's modulus of 0.5 TPa, which shows graphene's very strong and rigid mechanical properties. These excellent mechanical properties lead graphene applications in MEMS, mass sensors, pressure/strain sensors, resonators, and etc. Many research groups carried out theoretical analysis and simulation on graphene's potential working as ultra-high sensitive mechanical sensors including mass, strain and pressure. [15-17] Sakhaee-Pour et al. reported that using calculation and analysis of the vibrational behavior of defect free single-layer graphene sheet they obtained the possible sensitivity of graphene mass sensor can be in the order of 10^{-6} fg (10^{-21} g). While Ke Duan et al. obtained even higher sensitivity of 10^{-6} yg (10^{-24} g) using three-dimensional pillared vacant graphene structure (shown in Figure 1.6) by calculating the resonant frequency shift with capability of detecting the positions. [15]

Other than theoretical simulation, there are also reports on the experimental results. C-L Wong et al. investigated graphene drum structure with graphene obtained using mechanical exfoliation technique from graphite. By investigating its electrostatic deflection using atomic force microscopy (AFM), the structure was found to have up to 37.4 N/m spring

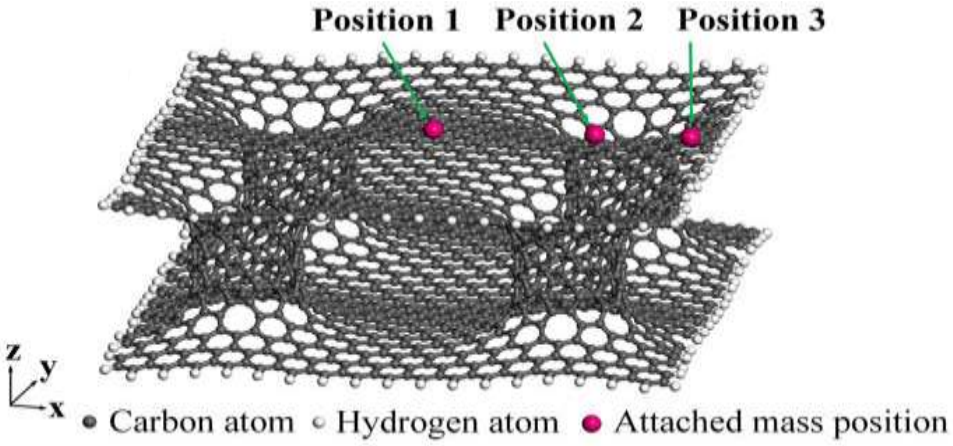

Figure 1.6 Schematic of the VACANT –graphene structure. [15]

constants which can have frequencies over 25 MHz and mass sensing sensitivity of 10^{-20} g/Hz. The sensitivity is two order magnitude higher than reported silicon-based structures. [18]

Other than mass/strain sensors, graphene's electro-mechanical property allows researchers to develop graphene-based MEMS/NEMS devices to explore its resonators, sensors and actuators applications.[19-21] Large-scale arrays of graphene resonators have been demonstrated by van der Zande et al. [21] They fabricated large arrays of suspended graphene membrane resonators using CVD graphene along with patterning and transfer

technique. (Shown in Figure 1.7) The resonator showed a capability of tunable frequency agrees well with their simulation and high quality factors up to 9000. This is one of the

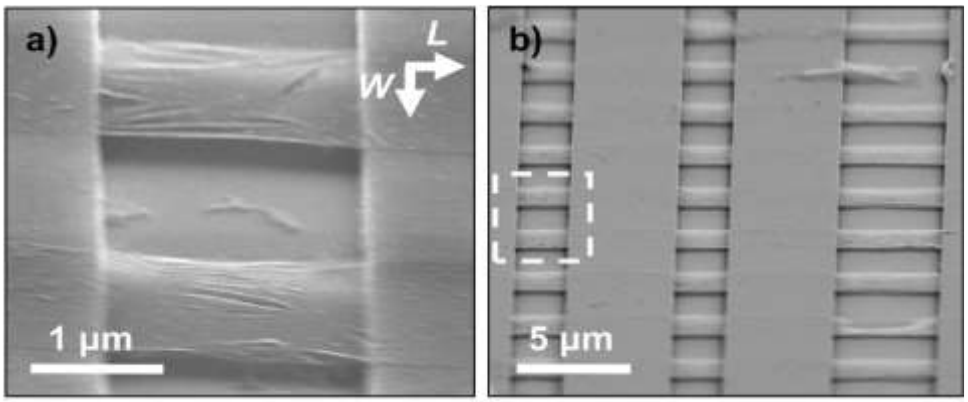

Figure 1.7 (a)Angled scanning electron microscopy (SEM) image of suspended graphene membranes over trenches in silicon oxide. (b) Angled SEM of an array of graphene membranes. [21]

breakthroughs for graphene technology development as CVD synthesized graphene can also be fabricated into reproducible devices showing excellent characteristics as the one from exfoliated graphene.

Due to more and more demand in extreme mass and strain sensitivity in advanced nano technological applications, graphene's excellent physical properties and its capability of ultra-high mechanical sensing have made itself to be a very promising material. With proof of many simulation results, further development in graphene's fabrication technique and analyzing method will realize its theoretical sensing performance in the near future.

1.2.2 Chemical Sensors

Among those exceptional material properties of graphene, its high electrical conductivity, high carrier mobility with low electrical noise, and large surface-to-volume ratio are greatly beneficial for gas sensor functions. Especially, due to its sturdy lattice

combined by σ bonds and delocalized π, π* bands out of lattice plane, graphene exhibits electrochemically very active characteristics. From experimental investigation, graphene showed a wide electrochemical potential window of ~2.5 V in 0.1 M PBS, and low charge transfer resistance (160-200 Ω).[22] The electronic structure and surface chemistry indicate graphene has an excellent electron transfer property that is beneficial for the detection of molecules when they approach the surface and interact with graphene. The molecule-surface interaction can change either the surface potential or conductivity (by changing carrier density resulted in oxidation or reduction), which will result in electrical property change as an output signal of sensing. Graphene's extremely high sensitivity has been proved by *K. S. Novoselov,* et al. in 2007 with the result of individual gas molecule detection.

To explore such a great sensing material's advanced detection potential, various electrical device configuration – chemiresistor, field effect transistor, Schottky diode, and etc. have been investigated, and/or with matching functionalization/ decoration layers – Pd, Pt, Au, oxide nanoparticles to obtain a better sensing quality in detection of various detecting targets. [23,24] After over a decade of extensive research and study, graphene's chemical sensing ability has been developed for various types of gas sensing, such as NH_3, NO_2, H_2, CO, SO_2, H_2S, and volatile organic compound sensing. [25] In this dissertation, to have a better insight into graphene's chemical sensing mechanism, molecular interactions between graphene and typical donor/acceptor gases are investigated by studying its carrier transport properties under gas exposure. The investigation methods and results will be discussed in detail in the following chapter.

1.2.3 Ion Sensors

Graphene, being essentially a surface, is extremely sensitive to changes in surface charge, or interaction with ionic adsorbates, presenting itself as an excellent material to develop ion sensors. Also, its semi-metal intrinsic characteristic makes any physical modification by adsorbates or surface interaction detectable by simply monitoring its conductivity change. An extensive study on graphene-based ion sensing applications has carried out, among what most ion sensing technologies developed so far focused on the detection of H^+ ions forming pH sensors, mainly in field effect transistor (FET) configuration. Different from a regular transistor structure in silicon based MOSFET devices, the ion sensitive field effect transistors (ISFET) use analytical solutions on top of the graphene sensing area as top gate. The device schematic and measurement setup of a graphene pH sensor developed in an earlier report is shown in Figure 1.8. [26] In early

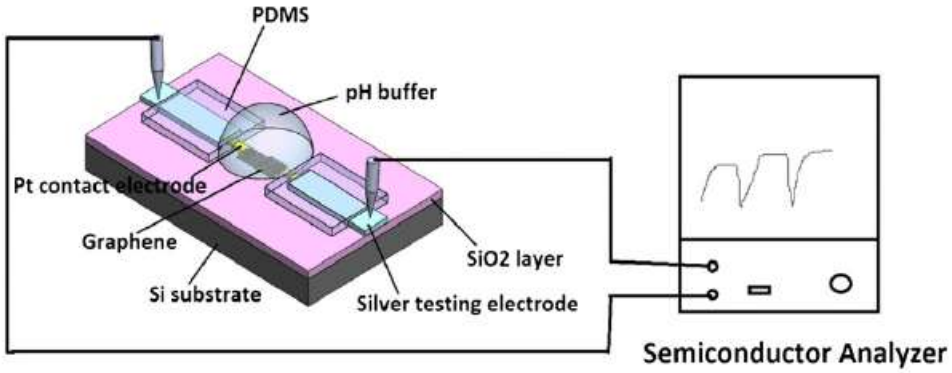

Figure 1.8 Schematic of graphene pH sensor and its measurement setup. [26]

studies, graphene used in pH sensor development was obtained from mechanical exfoliation of graphite, later on researchers can synthesize high quality graphene using

epitaxial growth method such as CVD synthesis.[27] CVD synthesis has made the fabrication process easier, repeatable, and CMOS process compatible. The ion sensor is one of the main research topics of this dissertation, thus more detailed fabrication technique will be discussed in following chapters.

The sensing mechanism of pH sensors is based on the adsorption processes of hydroxonium ions (H_3O^+) and hydroxyl ions (OH^-). [26-27] The hydroxonium ions make graphene n-doped and the other one make graphene p-doped. Therefore, graphene's conductance/resistance shift along with the concentration of the charges in the electrolyte solution and can be measured using electrical testing tools. The charge adsorption process during the sensing process is capacitive having an electrical double layer at the graphene/electrolyte interface working as a gate oxide. This also means the charges in the analytical solution cannot transmit across the interface or trap under the graphene layer. This is a big advantage of graphene-based sensors compared to traditional bulk material – based devices such as silicon based ISFET. Because while the device working in an aqueous environment, over the course of repeated operations, ion charges penetrate into gate oxide layer and accumulate at the interface between SiO_2 and Si. After less than two months, the sensor's performance degrades dramatically which makes devices life time very short. In addition to this advantage of graphene, with rising demand of ion sensors in various fields such as food, chemical industry, environmental monitoring, and medical application, more and more researches to develop graphene's sensing capability working in aqueous environment are carrying out, which includes graphene-based pH sensors, metal ion sensors (K^+, Hg^{2+}, Ca^{2+} etc.), and also Bio sensors. [28-29] Due to graphene's bio-

compatibility and high sensitivity there is also large amount of interest in developing graphene in bio-engineering applications,[30] which will be introduced in the next section.

1.2.4 Bio Sensors

Graphene's exceptional properties such as high surface-to-volume ratio, high conductivity, easy chemical modification, and excellent capability to bind with biomolecules also have drawn great interest in bio sensor development. However, due to its easy interaction with various biomolecules, a way to provide selectivity is needed to work as a sensor. To solve this problem, researchers conjugated some biomolecules such as DNA, protein, enzyme, and peptide on graphene to make itself selective only to intended analytical molecules.[31-33] With the help of such conjugated biomolecules, graphene not only can improve its biocompatibility but also make itself capable of selective detecting cells, proteins, DNA, neurotransmitters, and enzymes, antibody-antigen, and etc. in/outside of living cells. Moreover, researchers can design those binding molecules e.g. peptide sequences to provide graphene bio-sensor a unique selectivity to targeted bio-molecules. To give a better understanding, a schematic of the graphene-based biosensor is shown in Figure 1.9. [34]

An aptamer (red) is used in this sensing application to work as conjugating molecules on the graphene to detect targeted molecules/ions. From the schematic, the aptamers are connected to the graphene surface via linker molecules (green) which have a pyrene group for binding on the graphene. The pyrene group can make a strong π-π stacking with graphene thus be able to firmly attach onto the graphene. When the aptamer captured a target molecule, it undergoes a conformational change and forms a G-

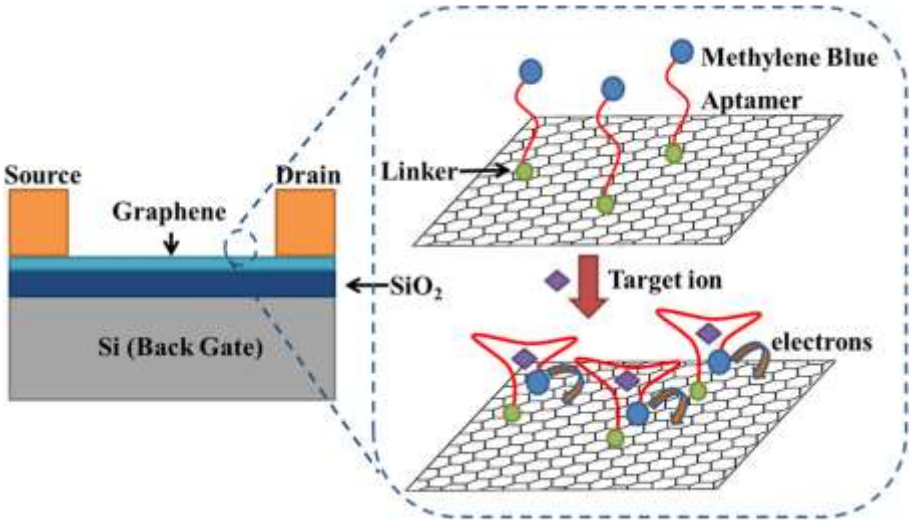

Figure 1.9 Schematic illustration of graphene-based biosensor. [34]

quadruplex structure due to consisting unit of aptamer - deoxyguanosine (G). As a result, methylene blue (blue) molecule at the end of aptamer, which is a strong electron donor brought close to the graphene surface. The approached methylene blue can interact with graphene and induce detectable Faradaic current. [34]

Other than assisted detection, there are also many studies have been reported on interaction modes between graphene-family materials and bio-molecules such as nucleic acids, lipid bi-layers, and small molecular drugs and dyes. [35-36] Due to the capability of graphene surface modification and design of binding molecules, the graphene's selectivity and sensitivity can be greatly enhanced for the bio sensing application. Furthermore, derivative materials such as graphene oxide, reduced graphene oxide (GO, rGO, etc.) are currently under an extensive study for its easier synthesis, handling, possibility of matrix composition with other materials.[37] Although there is still a big challenge to get

reproducible, stable graphene-based devices for commercialization, graphene still is a promising material for advanced future technology in various fields.

1.3 Outline of the Dissertation

This section will give an overview and the organization of this dissertation. Graphene, as called the parent material for most of the allotropes of carbon, its exceptional material properties and numerous applications have never ceased to amaze us. In this dissertation, starting with successful mono-layer graphene synthesis, the behavior of graphene-based electronic devices is investigated, then graphene's electrical transport properties are studied as well as how they were affected by surface adsorbates. Based on the graphene's prior research result, a graphene-based ion sensitive field effect transistor (G-ISFET) was designed and demonstrated highly sensitive and selective sensing performance. To verify G-ISFETs medical application, which is one of the motivations for this research, its working capabilities for implantable bio-sensor was examined. To present the contents systematically, the dissertation is composed of six themed chapters.

Chapter 1 has introduced graphene and related background information for this study. It started with graphene's unique physical nature and properties have been discovered in the past 15 years since the first graphene isolation. Which included graphene's atomic structure, energy dispersion characteristic and its exceptional material properties. Based on the understanding of its characteristics, graphene's excellent sensing applications have adopted in various fields were introduced with some typical examples.

Synthesis of high quality, large area graphene is still a remaining challenge for graphene's mass production. In Chapter 2, synthesis methods of graphene developed to today and especially the CVD epitaxial technique used in this research are discussed. Then, the prerequisite step of the graphene device process – the graphene transferring technique is introduced following with most widely used graphene characterization methods including Raman spectroscopy, atomic force microscopy (AFM), Hall measurement, and X-ray photoelectron spectroscopy (XPS).

Chapter 3 will give an overview of an apparatus first which was combined the Hall measurement system with a gas distribution system. Employing this apparatus, a study is carried out to investigate graphene's interaction with molecular surface absorption. According to many study results, graphene's interacting ability to the surrounded environment becomes higher with defect or functionalization introduced to it. In this research, defects are intentionally introduced to the graphene in the way of plasma treatment. The graphene's electrical properties show a very interesting change along with different intensities and the gas types of plasma. The effect of plasma on the graphene is observed with Hall measurement, and a theoretical mobility model by changing time of plasma treatment is proposed.

With the knowledge of graphene's ionic interaction and graphene-based device fabrication skills, in Chapter 4, a G-ISFET is fabricated and integrated onto a PCB board to allow the device to perform in an aqueous environment. While high sensitivity can be obtained from graphene's exceptional property, the selectivity is needed to be attained from an ion selective membrane (ISM). Valinomycin is the ionophore in the ISM brought K^+

ion selectivity to the G-ISFET. A brief working mechanism and the composition of ISM are given in the chapter for a better insight. Characterization of the G-ISFETs is carried out, the results show very high sensitivity and selectivity to K^+ ions as well as excellent repeatability and reliability.

To verify G-ISFETs sensing performance is suitable for an implantable bio-sensing application, Chapter 5 shows G-ISFETs measurements in various background solutions mimicking a physiological environment. Furthermore, a real cell based assay was conducted and the result is compared with that of commercial ion detector. Then, an array of G-ISFETs is designed and fabricated with CMOS process compatible technique, which also showed good sensing performance. Concerning a possible demand for a much higher ion sensitivity in future applications, a new diode-based device concept is proposed and graphene-based ion sensitive diode (G-ISDiode) is fabricated. The G-ISDiode showed very high sensitivity that agrees with the theoretical expectation demonstrated exponential sensitivity to ion concentration.

Finally, Chapter 6 consists of the conclusion of the research and future outlook. It summarizes the important accomplishments of this work and its contributions to the scientific community, along with potential directions and recommendations for future work.

CHAPTER TWO

GRAPHENE SYNTHESIS AND CHARACTERIZATION

2.1 Synthesis of Graphene

Graphene's synthesis technique has been developed for 15 years since from the first time graphene isolation, and now there are various techniques to obtain graphene. Except for those unpopular techniques such as unzipping nanotube, microwave synthesis, and pyrolysis of sodium ethoxide, the most commonly used synthesis techniques can be categorized into three different types. They are mechanical exfoliation (cleaving), chemical synthesis, and epitaxial growth. [38-39]

The first mono-layer graphene was obtained by Andrei Geim and Kostya Novoselov in a mechanical exfoliation technique. They peeled graphene layers using scotch tape from graphite and transferred them onto SiO_2 substrates. By this technique, although they only could obtain graphene flakes that are in the size of several microns in irregular shapes, the graphene is almost non-defective and high-quality. So, the technique quickly opened the way for early research of graphene's basic physics, where a low-defect high-quality material is more critical than the size of the film. Later on, various methods have been developed as the family of mechanical exfoliation, such as ultrasonication aided cleavage,[40] electric field aided exfoliation,[41] transfer printing,[42] and liquid-phase/chemical aided exfoliation.[43] However, those exfoliated graphene is not sufficient for graphene's further application requirement. For technological applications that take advantage of graphene's extraordinary material properties, the structure of graphene needs to be on a large scale, or in an oriented array of flakes to get a patterned and integrated

device. Thus, a better method for large scale and shape controllable graphene is needed. In less than two decades, a number of techniques have been developed to synthesize large area graphene and we can divide them into two categories, the first one is chemical synthesis and the other one is epitaxy.

2.1.1 Chemical Synthesis of Graphene

Chemical synthesis has been rapidly developed to become one of the best appropriate methods for large scale graphene. Other than the chemical exfoliation that increases the interlayer spacing of graphite and then exfoliates graphene layers by rapid heating or sonication, chemical synthesis involves oxidation of graphite with strong chemicals of oxidants. The strong oxidizing agents used in the technique include potassium permanganate ($KMnO_4$) and $NaNO_3$ in concentrated H_2SO4/H_3PO_4, or potassium chlorate ($KClO_3$) and fuming nitric acid (HNO_3). Then the oxidized graphite (GO) goes through a sonication process in the solution to form a homogeneous dispersion of graphene oxide layers. Lastly, the obtained graphene oxide needs a reduction process to remove excess oxygen-containing functional groups and other hetero-atoms to obtain graphene-like properties. Thermal, chemical, photo, electrochemical or microwave reduction techniques are available to get reduced graphene (rGO) from graphite oxide, and they showed a similar reduction effect producing a comparable quality of graphene.[38-39] Among these reduction techniques, the chemical reduction is the most widely used technique so far, and a variety of inorganic and organic chemical reducing agents have been tried and applied. For example, there are phenyl hydrazine, hydrazine hydrate, sodium borohydride, ascorbic acid, glucose, hydroxylamine, hydroquinone, pyrrole, amino acid, strongly alkaline

solutions, high temperature alcohol, and urea have been explored for the chemical reduction of GO.[44] Figure 2.1 shows the schematic of the preparing process in typical

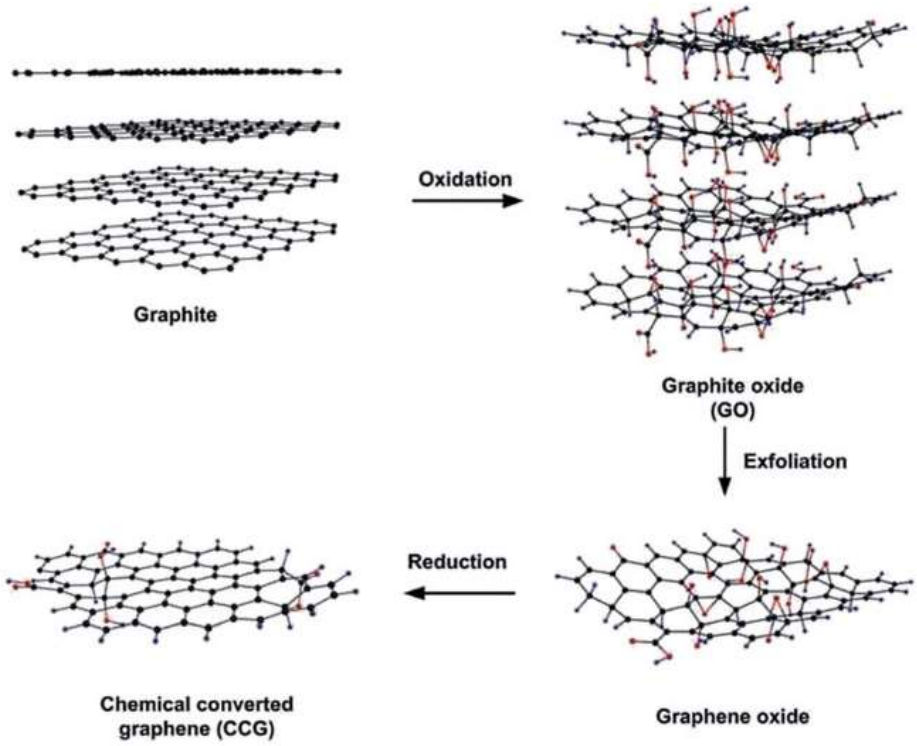

Figure 2.1 Preparation of reduced graphene oxide (rGO) in a typical chemical synthesis technique. [45]

chemical synthesis of GO. [45] Even though chemical synthesis is a possible way to produce large scale graphene, the reduced graphene oxides (rGO) usually contain a certain amount of residual defects caused by an incomplete reduction of graphite oxide. And the different degrees of reduction greatly affect the electrical properties and the number of layers of graphene, which is difficult to precise control in chemical processes. In the next

section, a graphene synthesis technique that can grow high-quality large scale graphene, epitaxial growth.

2.1.2 Epitaxial Growth of Graphene

Since neither mechanical exfoliation nor chemical synthesis can produce high quality and large scale with controllable film size and thickness, there has been an effort to develop other approaches. Epitaxial growth is the method regarded as having the most potential, and also the one currently maintains the popularity. One of the intensively studied epitaxial growth is high temperature SiC decomposition. A single crystalline SiC(0001) substrate is heated up to a temperature higher than 1000 ˚C in an ultrahigh vacuum chamber, which results in the sublimation of silicon atoms on the SiC surface. The surplus carbon atoms on the surface go through graphitization and consequently forms graphene film. The graphene grew in this technique has shown a single orientation owing to self-limiting sublimation of Si and corresponded self-limiting graphene growth, also in a large area. However, the limitation of the method is high process temperature and difficulty of graphene transferring on other substrates due to SiC's high resistance to chemical etchants.[39][46] Although the good insulating SiC substrates can be used directly into device architecture in some cases, there are always a large number of applications require the graphene's transference onto other substrates.

Chemical vapor deposition (CVD) is another epitaxial way to get high-quality, large area graphene. So far, CVD synthesis is believed to be the most efficient technique to produce graphene for industrial applications, for its high-quality, low-cost, large-area device fabrication availability. The mechanism of CVD growth is different from the one of

SiC epitaxial growth that decomposes the substrate at high temperatures. In a general CVD synthesis process, hydrocarbon precursors (CH_4) flow into a chamber where the temperature and pressure can be controlled, the precursors decompose under the set condition and then the carbon atoms deposit or aggregate on a metal substrate which is also a kind of catalyst in the process. Many metal substrates have been used in the CVD graphene synthesis, such as Fe, Ru, Co, Ir, Ni, Pt, Au, and Cu. Among these substrates, considering the material cost, the degree of difficulties of chemical etching (for later transferring process), and the quality of synthesized graphene, Cu and Ni are the most widely adopted substrates. Single crystal Ni (111) is a good substrate candidate in CVD graphene growth, as its atomically smooth surface can produce a uniform and thin graphene. However, due to its high solubility of carbon atoms at high temperatures, the decomposed CH_4 form a concentration gradient of carbon species at the Ni surface. When the process starts to cool down, the saturated carbon in the Ni precipitates out and segregate at the metal surface, which resulted in multiple layers of graphene formation. Also, different cooling rates determine different carbon segregation behaviors making the process difficult to control the graphene film thickness and quality. Unlike Ni, Cu has minimal solubility of carbon which is over 1000 times less than that in Ni (~0.001 atom% at 1000 °C in Cu comparing to ~1.3 atom% at 1000 °C in Ni). The low solubility lets the graphene growth a self-limiting process, practically stops further growth more than one layer. In addition to the relatively low cost of material and easily etching away completely, Cu became the most popular and promising substrate in CVD graphene growth for future technological applications. So, the graphene used in this research is also synthesized using

Cu foil substrates with a home-built CVD system, and the detailed steps and conditions will be discussed in the next section.

2.1.3 Graphene Synthesis on Cu Substrate with CVD System

As mentioned in the previous section, the low solubility of C prevents the dissolution of carbon species into the bulk Cu substrate, thus a monolayer graphene form on the Cu surface. The first graphene layer formed on the Cu covers the Cu catalyst surface, which will inhibit further dissociation of the hydrocarbon gas precursor and the growth of multilayer graphene. This graphene growth mechanism that only occurs at the Cu catalyst surface has defined as surface adsorption process, which in contrast to the process combined with segregation and precipitation process which is resulted in a bulk dissolution of C as on Ni substrate.[47] The adsorption process has been proved by Li *et al*. by the carbon isotope labeling method. They sequentially applied $^{12}CH_4$ and $^{13}CH_4$ as the precursors in the graphene growing process and investigated the isotope distribution of the

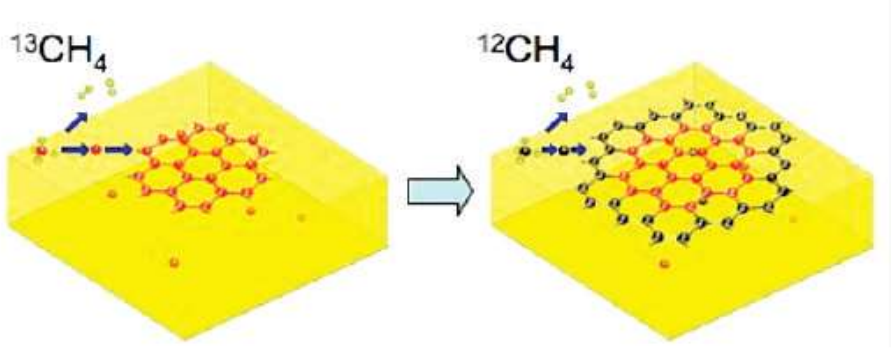

Figure 2.2 Surface adsorption process of graphene growth on Cu catalyst substrates. [47]

grown graphene film. Using the micro-Raman characterization, the graphene film showed separated domains of ^{12}C and ^{14}C-graphene corresponded to the sequential precursor

application. Therefore, it can be concluded that the graphene on Cu grows in a two-dimension configuration and this is owing to the surface-adsorption process as shown in Figure 2.2.[47]

The Graphene used in this research was synthesized using chemical vapor deposition (CVD) in a semi-automated quartz tube furnace system as shown in Figure 2.3. The apparatus consists of 4 basic components: gas delivery part, furnace, vacuum control, and control panel. Quarter-inch stainless steel tubing connects each component and delivers gases. Three compressed gas tanks for high-purity CH_4, H_2 and Ar are purchased from Airgas. Inc, and each of them connected to the corresponded mass flow controller (MFC). Through MFCs, the gases can flow with set amount of flow rates into a 60 mm O.D. quartz process tube where the Cu substrate placed. As the second component of the CVD system, the furnace (MTI, OTF-1200X) holds the process tube and controls its temperature, which is powered by 220 V AC. Thirdly, the vacuum of the quartz tube is

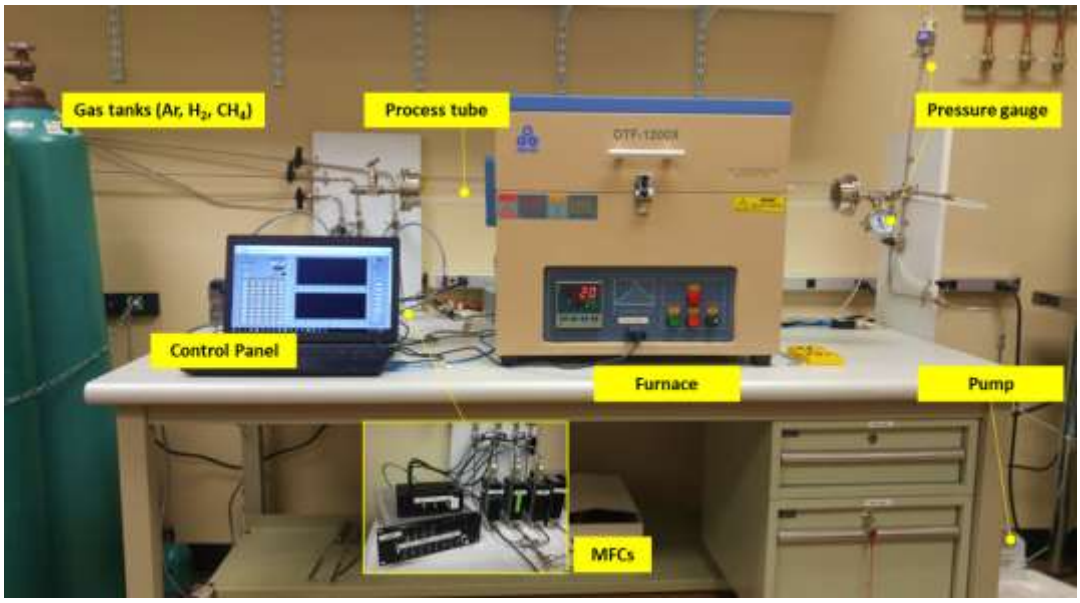

Figure 2.3 Home-built semi-automated CVD system for graphene synthesis.

provided by a mechanical rotary vane pump (Pfeiffer Vacuum, Duo 10M). The tubing connects the outlet of the process tube to the pump's inlet, then the pump's outlet is connected to a room exhaust line. To control and monitor the pressure of the process quartz tube, two pressure gauges are attached to the system. One is a general liquid filled pressure gauge attached at the quartz tube and the other is a digital Pirani gauge (MKS 901P, loadlock transducer) attached at tubing line before pump inlet in between two manual valves. Two manual valves have functions not only a general avoidance of gas backflow from pump into the process tube, they are also used for controlling the process pressure of the quartz tube during graphene synthesis.

Lastly, we set up a control system that can both monitor and set value for process temperature, chamber pressure, gas flow rate, and valves' on/off. Since the whole synthesis process takes 3~4 hours, the automated control system enabled the parameter optimization of the graphene synthesis process easier to control and monitor, also more efficient in terms of time and labor. To make the gas delivery system controlled on a computer, digital type MFCs (MKS, GE50A) are used to set parameters (gas type, set flow rate, read flow rate), each of them is connected to a computer through an Ethernet cable. Additionally, three solenoid valves are installed in between MFCs, they are powered (12V DC) and controlled using a microcontroller (Arduino, Micro) so that we don't need to manually open or close the gas tanks during the synthesis process. The microcontroller is programmed and wired on a PCB board, then a micro-USB cable connected it to the computer. So, gas deliveries for all three types of gas (CH_4, H_2, and Ar) can be controlled by their flow rates, and on/off through the computer via solenoid valves, digital MFCs, and microcontrollers. For set and

monitor process temperature, the furnace is connected to the computer with USB cable,

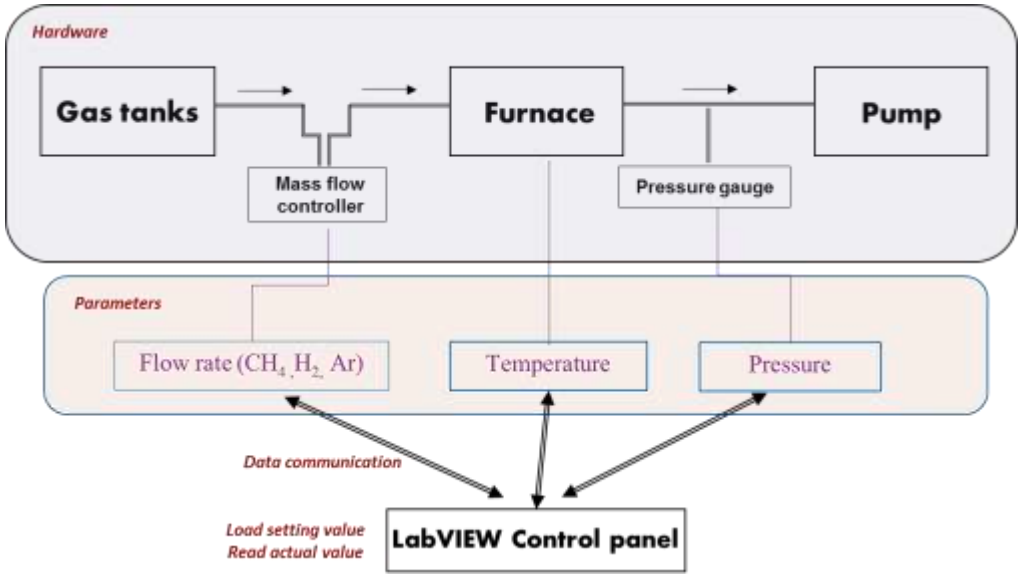

Figure 2.4 Schematic diagram of CVD control system.

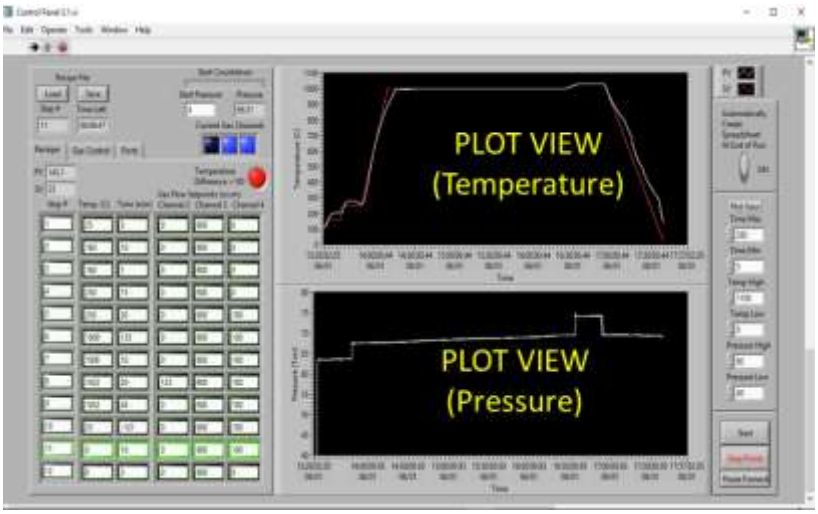

Figure 2.5 LabVIEW control panel of CVD system.

while the digital Pirani pressure gauge is also connected to the computer for monitoring the process pressure. From the schematic in Figure 2.4, all three parameters can be communicated to a computer and they are controlled using LabVIEW program. Figure 2.5

shows the LabVIEW control panel. The block diagram can be found in Appendix A at the end of the dissertation.

With the built CVD and automated control system, monolayer, uniform graphene over a large area was obtained on a copper foil (Alfa Aesar, 99.999% purity), which acted both as the substrate and catalyst. Ultra-high purity methane (CH_4) was used as the growth precursor, along with H_2 and Ar as the carrier gases, which were flown into the furnace through mass flow at nominal flow rates of 100, 100 and 900 sccm, respectively. The copper substrate was annealed at 1000 ◦C for 2 h under a continuous flow of H_2 and Ar gases prior to growth, which was followed by the graphene growth at 1035 ◦C over a duration of 20 min under a continuous flow of methane. The synthesis process steps are shown in Figure 2.6. The whole process starts with a Cu foil preparation step which

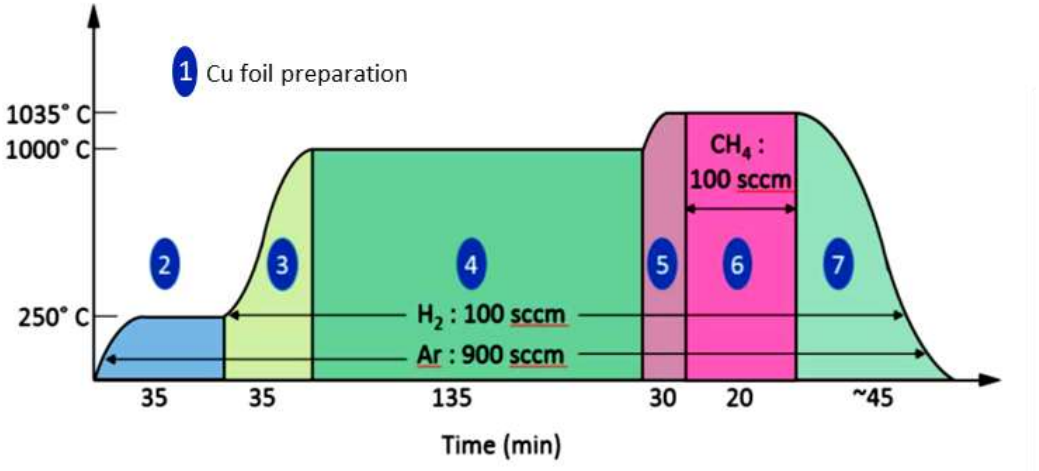

Figure 2.6 Optimized process parameters and sequence of steps for graphene synthesis with CVD.

includes making a mark at the corner of Cu foil to distinguish top/bottom side, flattening foil with two glass slides, and a chemical cleaning procedure. In the cleaning process, the

Cu foils were first cleaned in acetone and isopropanol to clean organic contamination, then etch in HNO_3 (10 ~20 %) solution (~3 s) followed by sonication in acetic acid for 10 min to remove copper oxides (CuO and Cu_2O) presenting on Cu foil surface.

2.2 Graphene Transfer to an Arbitrary Substrate

The CVD grown graphene on metal substrate needs a transference procedure to conduct any characterization or further device fabrication. The transferring technique used in this research is shown in Figure 2.7. (a) In our graphene growth on Cu foil it grows on both sides and the bottom side graphene is in general inferior quality as compared to the one gown on the top side of the foil. So, the copper foil was marked to distinguish the side of foil in the cleaning process, which has described in the earlier section. (b) The top side graphene is protected by spin coating of poly methyl methacrylate (PMMA) twice at 5000 rpm for 40 sec resulting in approximately 800 nm thickness of the film. It also provides mechanical strength to graphene in the subsequent processing steps. (c) The sample is then kept in concentrated Cu etchant ammonium persulfate ($(NH_4)_2S_2O_8$) overnight for complete removal of Cu. (d) This results in graphene/PMMA layer floating in the etchant and resultant byproducts which is mostly copper ion turning the solution bluish. (e) The floated graphene is rinsed multiple times in deionized water (DI). A prepared substrate can then be slid underneath the floating graphene/PMMA (f) and scooped off from the liquid solution. The figure (g) is a picture of transferred graphene/PMMA on SiO_2/Si substrate. The substrate containing transferred graphene/PMMA is allowed to dry in air and then baked at 220 ˚C above the glass transition temperature of PMMA to allow its reflow in

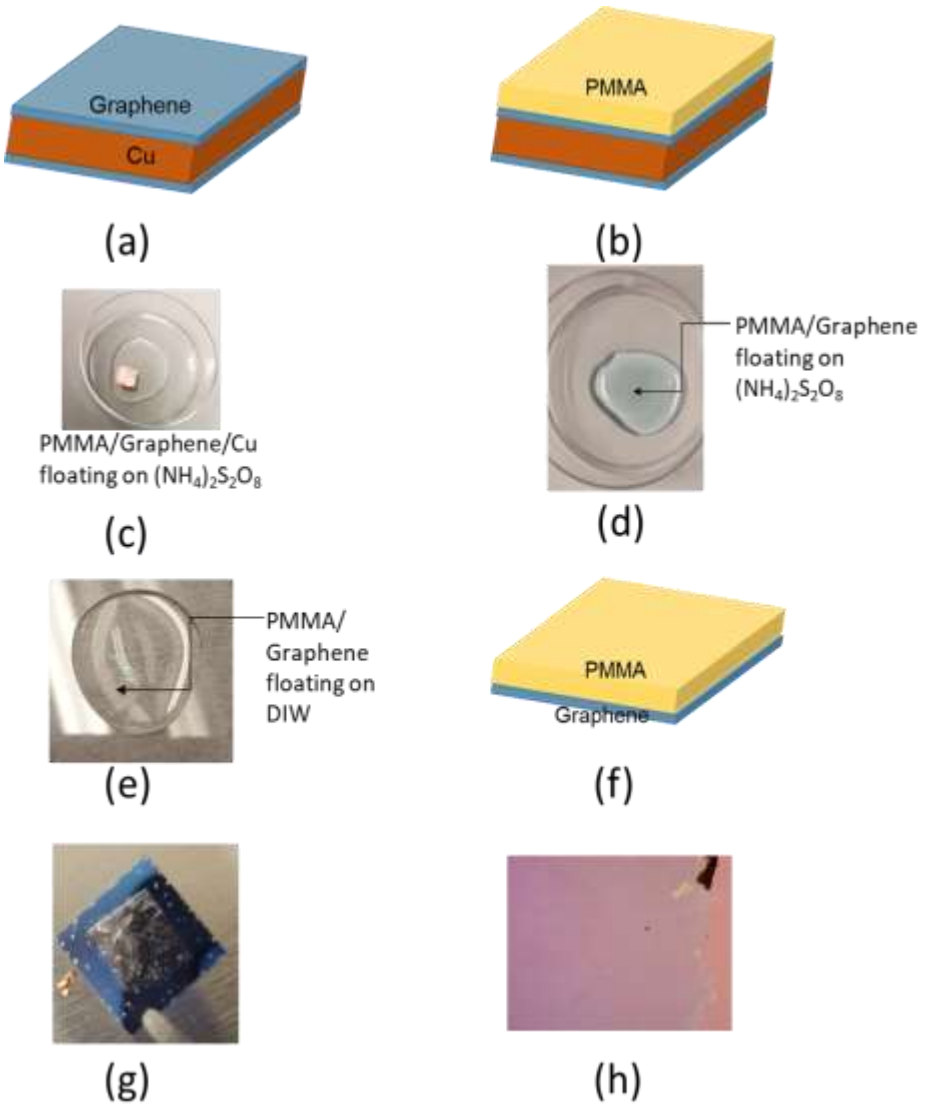

Figure 2.7 Graphene wet transferring process steps.

order to reduce the wrinkles in graphene originated while transferring on substrate. The sample is then dipped in acetone for 2-3 hours to remove PMMA from top of transferred graphene. Figure (h) shows the transferred graphene under optical microscope.

Due to the particularity of CVD graphene in the synthesis process, lower quality graphene can be found on the bottom side of the copper. Even though the bottom layer of

graphene does not interfere during the wet-transferring process, the graphene residue will attach at the top layer of graphene during copper etching process at step (C) and be transferred on the target substrate as well. The optical image of transferred graphene with bottom side graphene residue is shown in Figure 2.8 (a). So, to get a clean mono-layer graphene film on a targeted substrate, a bottom-side graphene removal process is conducted after PMMA coating (step (b)). In a plasma etch system PE25-JW (Plasma Etch, Inc.), the Cu/graphene/PMMA was placed with bottom-side of Cu facing up. Then, 150 W of O_2 plasma for 1 min was used to etch away all of the bottom-side graphenes. Figure 2.8(b) shows a clean and uniform graphene's optical image on SiO_2/Si substrate after the bottom-side graphene removal in comparison with the one without additional etching process.

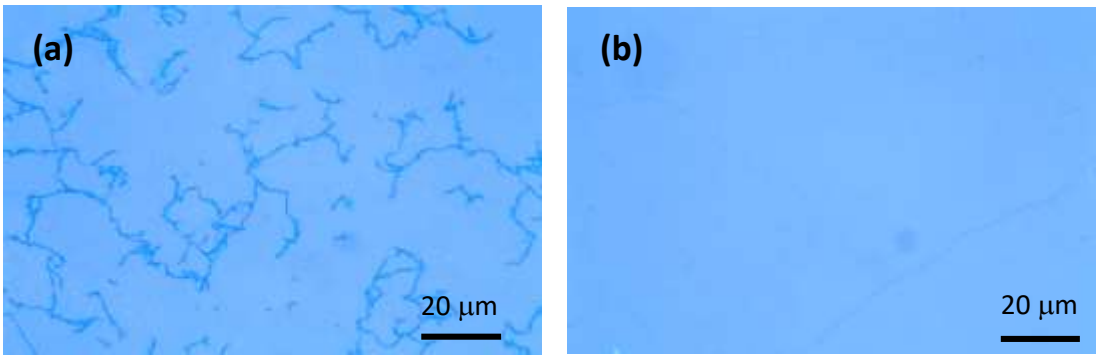

Figure 2.8 Optical image of wet-transferred graphene on SiO_2/Si substrate (a) without bottom-side graphene removal and (b) with bottom-side graphene removal. (Optical microscopy Olympus BX41M is used to take images.)

The graphene web transferring technique described above applies to an arbitrary substrate that does not dissolve in acetone. In this research, we tried the technique on glass, SiO_2, sapphire, quartz, and PET flexible film as the substrate, successfully transferred graphene without damage its high uniformity and film quality.

2.3 Characterization of graphene

After the graphene is isolated from the catalytic metal substrate by the transference technique, the graphene needs reliable and quick feedback for its film quality before proceeding to next step device preparation. Raman Spectroscopy and atomic force microscopy (AFM) are two most widely used inspection tools to determine graphene's crystalline property, defect information, film morphology and thickness. On top of it, Hall measurement is a powerful method to determine graphene's electrical property. Without complex preparation steps, we can obtain many important carrier transport properties of graphene – majority carrier type, carrier mobility, carrier concentration, and sheet conductivity – simultaneously in one measurement system. Furthermore, to take further insight into graphene's sensing mechanism, we need to analyze the elemental composition of the graphene on some occasions. X-ray photoelectron spectroscopy (XPS) can provide the information of empirical formula, chemical state, and electronic state of the elements that exist on the graphene surface. In this section, graphene's various characterization methods and analysis tools will be discussed along with the obtained results from the graphene used in this study.

2.3.1 Raman Spectroscopy

Raman spectroscopy is commonly used to provide a structural fingerprint by which molecules can be identified. It relies on inelastic scattering, or Raman scattering, of monochromatic light from a laser. The laser light interacts with molecular vibrations, phonons or other excitations in the material, resulting in the energy of the photons being shifted up or down. Then the shift in energy gives information about the vibrational modes

in the material system. By analyzing Raman spectroscopy, we can characterize graphene's crystallite size, clustering of the sp^2 phase, the presence of sp^3 hybridization, defects, and crystal disorders. Raman spectroscopy plays an important role in the study and characterization of graphitic materials. [3] Figure 2.9 shows the Raman spectra from various crystalline and disordered sp^2 carbon nanostructures, [48] which is a good example to understand how different sp^2 carbon structures can be distinguished by Raman spectra analysis. The very top spectrum is the Raman spectrum for monolayer graphene with a low G-band and high G′-band. G-band is a common peak at ~1580 cm^{-1} in graphitic materials as it rises by the stretching of the C-C bond for all sp^2 carbon system. In the Brillouin zone, the G peak is from the doubly degenerate zone center E_{2g} mode.[49] G′-band at ~2700 cm^{-1} is the second most prominent peak that always can be observed in graphite materials. However, it does not relate to G-peak, instead, it is the second order of zone-boundary phonons. Two phonons with opposite momentum the highest optical branch near the **K** induce G′ peak. Such phonons give rise to a peak at ~1350 cm^{-1} in defected graphite which is called D peak. So, after researchers found out the relationship G′ peak has also been called 2D peak. Compared to the monolayer graphene, the Raman spectrum for 3D highly oriented pyrolytic graphite (HOPG) shows a distinctly different spectrum (second spectrum from the top) with lower, split G′ band. In the multiple graphene layers, the interaction of the graphene planes causes the π and π^* bands to divide into multiple bands (e.g. for bilayer graphene, divide into four bands), which results in 2D peak splitting, peak density reduction. Single wall carbon nanotubes (SWNTs) also showed its distinguishable Raman spectrum features in Figure. 2.9. Its radial breathing mode (RBM) and G-band splitting

into G^+ and G^- -bands are the typical Raman features for SWNT that are different from any other sp^2 carbon nanostructures.

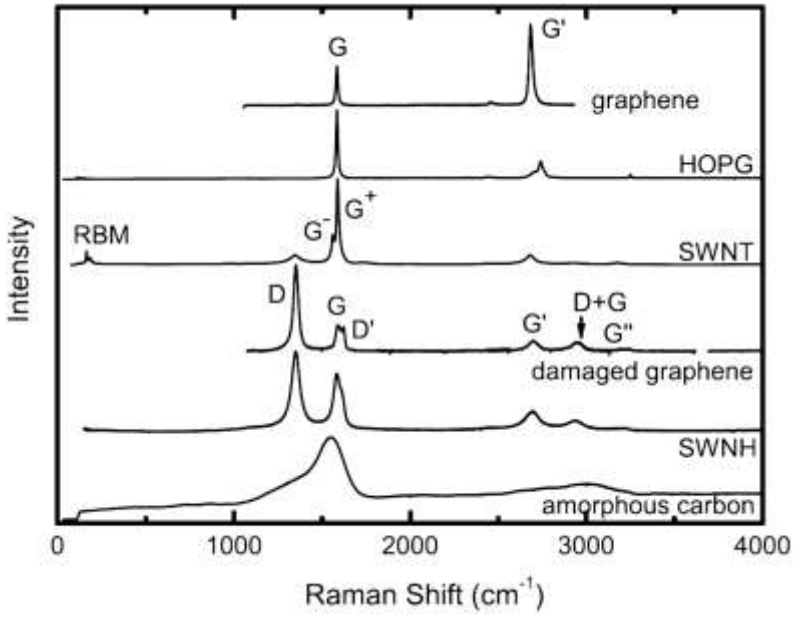

Figure 2.9 Raman spectra from several sp^2 nanocarbons. From top to bottom: crystalline monolayer graphene, highly oriented pyrolytic graphite (HOPG), a single-wall carbon nanotube (SWNT) bundle sample, damaged graphene, single-wall carbon nanohorns (SWNH) and hydrogenated amorphous carbon. The most intense Raman peaks are labeled in a few of the spectra. [49]

On the contrary, damaged graphene or defected graphene introduce disorders in the crystal symmetry and activate corresponded vibrational modes, which can be observed in the Raman spectrum as D-band, D′-band, and their combination D + D′ mode. From the defect peaks, one can estimate or predict different types of defects in the graphene crystalline structure. Materials such as single wall carbon nanohorns (SWNH) and amorphous carbon show two different degrees of disorder of carbon crystal structures. When the disorder is so dominant that only very neighbor structural correlations are

present, even though both sp^2 and sp^3 bonding exist, none of the sharp peaks rises in the Raman spectrum, instead, broad first- and second-order features present as shown in amorphous carbon.

Figure 2.10 shows a typical Raman spectrum of graphene (on SiO_2/Si substrate) used in this study marked with signature D, G and 2D peaks. The I_D/I_G ratio of ~0.17 indicates the good quality of the graphene layers. The 2D peak full width at half maximum (FWHM) value of ~26.8 cm^{-1}, and the intensity ratio of the 2D band (at 2682 cm^{-1}) and G band (at 1585 cm^{-1}) was 3.2, indicating the presence of a single layer of monolayer graphene.

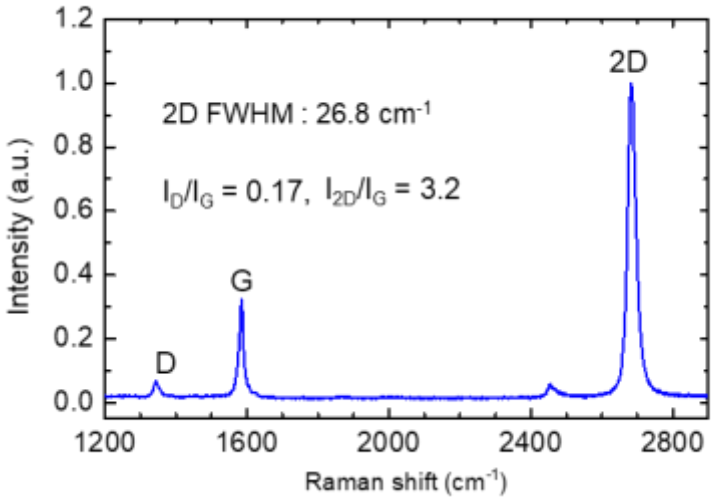

Figure 2.10 Raman spectroscopy of graphene on SiO_2 used in this study.

Raman spectroscopy is a fascinating tool for understanding sp^2 carbon systems, thus the tool has been used intensively in this study to characterize graphene and determine graphene's qualities during graphene synthesis development, before device fabrication, and in carrier transport investigation as well.

2.3.2 Atomic Force Microscopy (AFM)

Atomic force microscopy (AFM) is a high resolution type of scanning probe microscopy that can quantify surface roughness of samples up to atomic resolution which is on the order of fractions of a nanometer. This resolution is over 1000 times higher than the optical diffraction limit thus has been widely used in nanomaterial research including graphene research. To obtain the surface image, AFM uses a piezoelectric element to oscillate a cantilever while a sharp tip located at the free end of cantilever brought in close proximity to the sample surface (non-contacting/tapping mode) or in contact with the surface (contact mode). Due to graphene's delicate structure tapping mode has been adopted to investigate its morphology. When the system scans over the sample surface in raster fashion, the probe tip interacts with the sample and the interaction force caused by surface topography is measured in terms of correspondent deflection of the cantilever. The

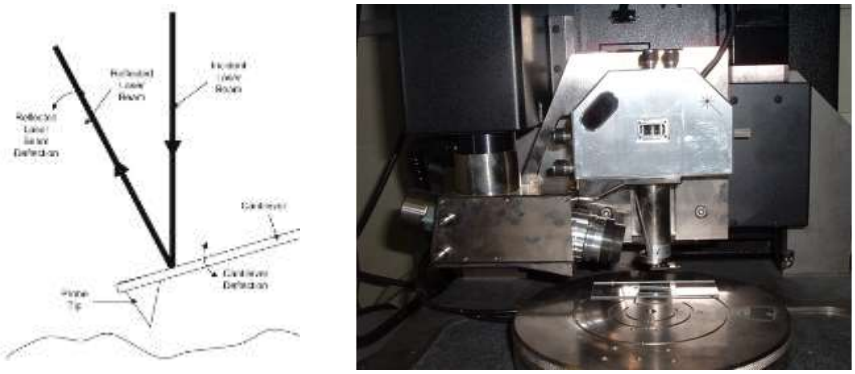

Figure 2.11 (Left) AFM schematic and (Right) a part of AFM system including scanning head, camera and sample stage. [50]

deflection of the cantilever is recorded using a laser beam reflected off the top surface of the cantilever and detected by a position-sensitive photodiode detector (PSPD). [50] AFM

schematic and a part of AFM system (scanning head, camera, sample stage) are shown in Figure 2.11.

An AFM system Dimension 3100 from Veeco Instruments Inc. is used in this study. An AFM image of graphene (on SiO_2 substrate) on SiO_2/Si substrate taken using the Dimension 3100 system is shown in Figure 2.12 along with the graphene's Raman spectrum. From the Raman spectrum as introduced in the previous section, a much larger intensity of the 2D-peak relative to the G-peak, $I_{2D}/I_G = 4.0$ indicates the presence of monolayer graphene. [51] The D-peak was also very low ($I_D/I_G < 0.1$) indicating high-quality graphene. The AFM image (2.5 μm × 2.5 um) shows a smooth and uniform surface

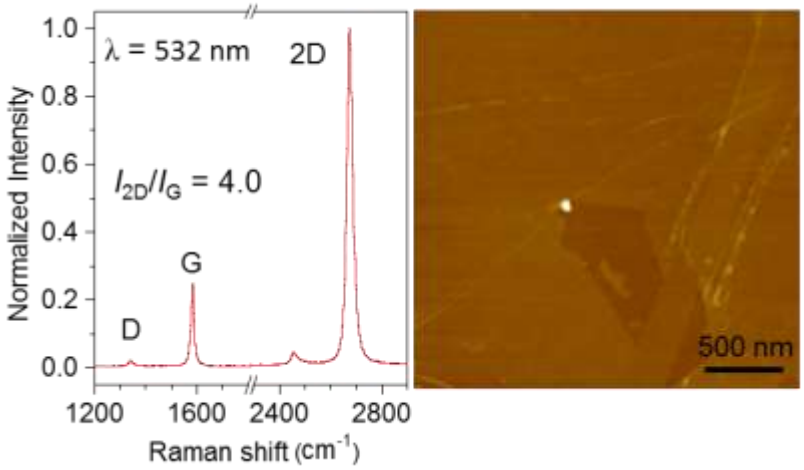

Figure 2.12 (Left) Raman spectroscopy (Right) AFM image of graphene transferred on SiO_2/Si substrate.

of mono-layer graphene with occasional wrinkles and small tears arising from the transfer process. By profiling the edge of graphene layer, the measured thickness of mono-layer graphene used in this study ranged between 0.6 – 1.1 nm. Although the theoretical mono-layer graphene thickness is 0.335 nm, which is layer-to-layer carbon atom distance of graphite crystal, a wide range of thickness values obtained by AFM has been reported (0.4

– 1.7 nm). The discrepancy is often caused by tip-surface interactions, image feedback settings, and surface chemistry. [52] Even though AFM cannot provide an accurate thickness of graphene, it still is a powerful tool to observe nanoscale details of graphene morphology and plays an important role to determine graphene's quality.

2.3.3 Hall Effect Measurement

One way to independently determine the variation in mobility and conductivity caused by molecular adsorption is by fabricating a graphene based field effect transistor in a back-gated configuration.[28][53] This allows one to extract the conductance (σ) and transconductance (g_m) from the $I_d - V_d$ and the $I_d - V_g$ plots, respectively, which can then be used to find the field effect mobility and the carrier concentration.

However, a large back gate voltage may be required to obtain an appreciable change in I_{ds} (or more preferably the "V-shaped" characteristics), depending on the insulator (typically SiO_2) thickness and the carrier density in graphene, which may also cause the insulator to leak and even breakdown. Even if the insulator does not break, there is always a chance of charge injection and accumulation in the insulator layer, causing the slope of the $I_d - V_g$ characteristics to be altered leading to an erroneous determination of mobility. Additionally, this technique only works when it is possible to use a back gate (or a top gate, which is more cumbersome to realize) and is not suitable for graphene transferred to arbitrary substrates. An alternative technique to simultaneously determine changes in carrier mobility and concentration in graphene transferred onto an arbitrary non-conductive substrate is based on Hall Effect measurement. At low magnetic fields, and in presence of

a majority carrier (away from the Dirac point) in graphene, this is a reliable technique to independently and simultaneously measure carrier mobility and concentration.

The basic physical principle of the Hall effect is the Lorentz force, by which electron subjects to the force and moves along the electric field direction perpendicular to an applied magnetic field. This induced drift current under the magnetic field results in an excess surface electrical charge on the side of the sample, consequently, a potential drop across the two sides of a sample can be measured which is Hall voltage V_H. Due to the magnitude of V_H is equal to IB/qnd (where I is current, B is the magnetic field, d is sample thickness, and q (1.602×10^{-19} C) is the elementary charge sheet), carrier density of the material can be obtained. On top of it, with easily measurable sheet resistance R_s, Hall mobility can be determined from the equation of $\mu = |V_H|/R_sIB = 1/(qn_sR_s)$. When the conducting layer thickness d is known, then its bulk resistivity can be calculated as $\rho = R_sd$ and the bulk density as $n = n_s/d$. [54]

The van der Pauw method was first reported in 1958 by Leo J. van der Pauw of Philips Research Laboratories to measure sheet resistivity and Hall coefficient of thin-films.[55] The sample employs a four-point probe placed around the perimeter of the sample, in contrast to the Kelvin technique with a linear four point probe configuration. To accurately measure the properties, the most preferred sample shape is cloverleaf which will have the lowest error due to its smaller effective contact size as shown in Figure 2.13. However, due to the complexity of cloverleaf shape make the fabrication more difficult, a square shape van der Pauw method is widely used in the semiconductor industry.

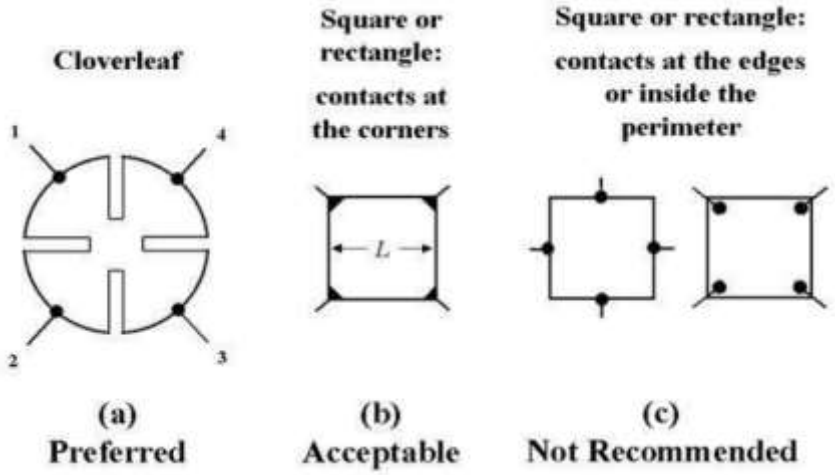

Figure 2.13 Sample geometries for van der Pauw technique. [55]

In this work, a rectangle shape for van der Pauw technique is employed to measure graphene's electrical properties including Hall carrier mobility, sheet carrier density and sheet conductivity with Hall measurement system Ecopia HMS 3000 (using 0.55 T magnetic field) shown in Figure 2.14. The graphene Hall samples were prepared using In/Sn alloy dots (95%-In, 5%-Sn) pressed at four corners of a square-shaped graphene layer forming Ohmic contacts (on a SiO_2/Si substrate).

2.3.4 X-ray photoelectron spectroscopy (XPS)

In the introduction of graphene's sensor applications (Chapter 1, section 2), it has been mentioned that engineering of the graphene surface can enhance graphene's sensing performance. Thus, there is a lot of interest in the study of derivative materials such as graphene oxide and reduced graphene oxide (GO, rGO, etc.). Those materials are not only

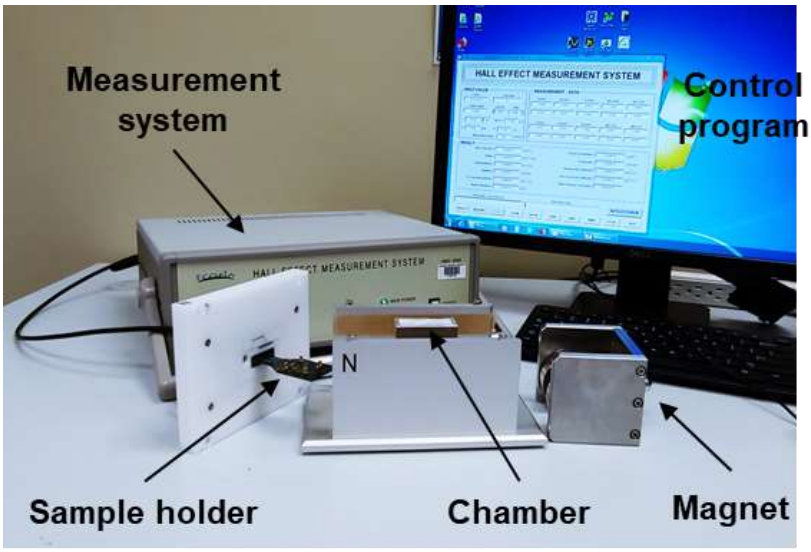

Figure 2.14 Set up Hall measurement system used in this study. Ecopia HMS 3000

can be engineered to improve designated sensing properties but also have advantages including easy synthesis, handling, and the possibility of matrix composition with other materials.[37] As a result, information on functionalized graphene's elemental composition and its chemical and physical interactions occurring on graphene's surface became very important in the graphene research. For this, XPS is an ideal characterization tool to investigate graphene's surface chemistry providing information such as surface elemental composition, empirical formula, and electronic state of the elements present. In XPS characterization, a sample surface is excited using a beam of x-rays and this excitation causes photoelectrons emitted from the sample surface (top 10 nm). By analyzing the energy of emitted electrons, the system will produce a photoelectron spectrum (energy intensity vs. binding energy) as measurement data, then we can determine materials characteristics from the spectrum. [56]

In an earlier report, Al-Gaashani et al studied C 1s XPS spectra of chemically synthesized graphene oxide and compared it with original graphite before oxidation. [57] The spectra are shown in Figure 2.15. Figure 2.15 (a) shows high-resolution XPS C1s region spectrum of graphite with curve fitting carried out at peak binding energies of 284.76 eV (C-C), 287.00 eV (C-O), 288.28 eV (C=O), 289.50 eV (O-C=O). Among these bonds, C-C is the main bond with an atomic ratio of 92.61 % also can be seen from the plot. This means the graphite used in the study as raw material was quite pure with very

little oxygen bonded as defects in the material. On the other hand, after the graphite was treated with acid, other peaks C-O, C=O and O-C=O increased significantly (Fig. 2.14(b)), with atomic ratio of 29.46 %, 16.63 % and 5.21 %, respectively, while C-C atomic ratio

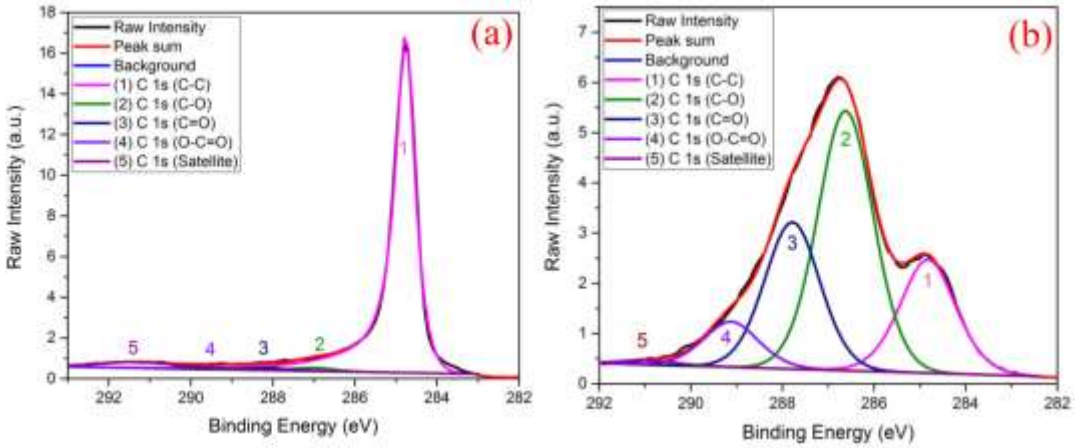

Figure 2.15 (a) C 1s XPS spectra of graphite and (b) graphene oxide (GO). [57]

was only 13.06 %. From this XPS analysis, we can have a deep insight into the graphene oxidation process and the elemental composition and chemistry of the graphene-oxide, which can help researchers to have a better understanding of chemical functionalization in graphene and material engineering, as well as optimization and development of GO synthesis methods.

CHAPTER THREE

INVESTIGATION OF GRAPHENE CARRIER TRANSPORT PROPERTIES DUE TO SURFACE ADSORBATES

3.1 Introduction

Since the first discovery of the Graphene in 2004, extensive research has been carried out worldwide to investigate its unique material properties and device applications. [13,35,36,37,38] Among the numerous potential applications of graphene reported, inexpensive yet high-performance gas sensor development has emerged as one of the most attractive in terms of practical applicability in the short term. There are several unique attributes of graphene, such as high surface-to-volume ratio, high carrier mobility, and unsaturated sp^2 bonds, which make it very attractive for sensing applications.[62] Although numerous reports on graphene's excellent sensing behavior exist, there are many instances where the sensing mechanism is not completely understood.[24] For example, while many of sensing applications are based on the change in conductivity or Dirac point in graphene, measured in various device configurations (resistor, FET, Schottky diode), and/or with functionalization layers (Pd, Pt, Au), those simple measurements are not sufficient to provide detailed understanding of the sensing mechanisms in graphene.[23][25][53][63] This is because conductivity is a product of two basic charge carrier properties, mobility and concentration, so information regarding the change in conductivity (due to molecular adsorption) does not offer insight into their individual changes. On the other hand, the measurement of Dirac point shift directly correlates with changes in charge density but does not provide direct information on mobility. Although fairly obvious, mobility and

carrier concentration can change independently of one another depending on the characteristics of the adsorbing molecules, and knowledge of the change in both parameters (especially with time dependence) can be helpful in determining the type of the molecules adsorbed.

This chapter will investigate simultaneous and temporal variations in carrier mobility and concentration caused by molecular adsorption on graphene systematically using the Hall measurement technique. Graphene was exposed to two different types of gas molecules, NH_3 and NO_2, which typically behave as donors and acceptors in graphene. It was observed that exposure to the gases changed the conductivity in opposite directions, however, the temporal variations in carrier concentration and mobility were found to be intriguing. A simple physical model has been proposed to explain the observations. Effect of heavier doping, through exposure to an organic chemical (trimethyl hexamethylene diamine ($C_9H_{22}N_2$)) carrying two amine groups, was also investigated, which first reduced and then flipped the doping of graphene from p-type to n-type, which eventually recovered close to the initial doping level upon removal of the exposure.

3.2 Molecular interaction with graphene

3.2.1 Electrical characterization and measurement setup

One way to independently determine the variation in mobility and conductivity caused by molecular adsorption is by fabricating a graphene based field effect transistor (FET) in a back-gated configuration.[28][53] This allows one to extract the conductance (σ) and transconductance (g_m) from the $I_d - V_d$ and the $I_d - V_g$ plots, respectively, which

can then be used to find the field effect mobility and the carrier concentration as in Figure 3.1, where a representative $I_{ds} - V_g$ characteristics measured from graphene FET is shown. (The structure fabrication details will be discussed later) From the plot, the positively shifted Dirac point at ~23.3 V indicates the graphene is p-type, which is expected for graphene transferred on SiO_2 substrates.[64-65] The transconductance $g_m = \partial I_{ds}/\partial V_g$ is calculated (see dotted straight line in the p-type region of the curve) as 3.2×10^{-5} S. Using the relationship $\mu_{FE} = g_m L/(WC_{ox}V_{ds})$ (where C_{ox} is the gate oxide capacitance, G is the

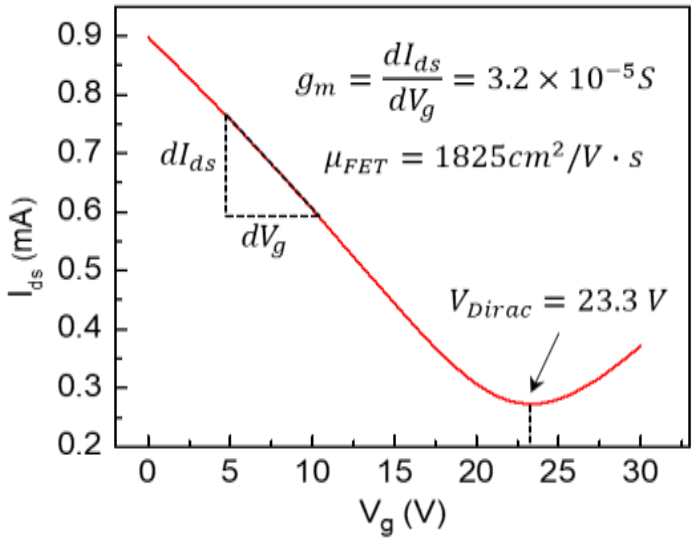

Figure 3.1 $I_{ds} - V_g$ characteristic measured from back-gated graphene FET device showing typical V-shaped characteristic.

conductance, L and W are the material's length and width between source and drain, respectively) [28], the field effect mobility (μ_{FE}) can be calculated as 1,825 $cm^2V^{-1}s^{-1}$.

However, a high back gate voltage may be required to obtain an appreciable change in I_d (or more preferably the "V-shaped" characteristics), depending on the insulator (typically SiO_2) thickness and the carrier density in graphene, which may also cause the

insulator to leak and even breakdown. Even if the insulator does not break, there is always a chance of charge injection and accumulation in the insulator layer, causing the slope of the $I_d - V_g$ characteristics to be altered leading to an erroneous determination of mobility. Additionally, this technique only works when it is possible to use a back gate (or a top gate, which is more cumbersome to realize) and is not suitable for graphene transferred to arbitrary substrates. An alternative technique to simultaneously determine changes in carrier mobility and concentration in graphene transferred onto an arbitrary non-conductive substrate is based on Hall Effect measurement. At low magnetic fields, and in the presence of a majority carrier (away from the Dirac point) in graphene, this is a reliable technique to independently and simultaneously measure carrier mobility and concentration.

In this work, 6 × 6 mm shape of graphene transferred on thermally grown 300 nm SiO_2/Si (n^+) substrates is employed to measure graphene's properties using van der Pauw Hall measurement technique. In/Sn alloy dots (95%-In, 5%-Sn) are pressed at four corners of a square-shaped graphene layer forming Ohmic contacts (on a SiO_2/Si substrate). To simultaneously measure film properties – carrier mobility, sheet carrier density, and sheet conductivity during gaseous exposure, a quarter-inch gas flow tube was connected to the sample loading chamber of Hall measurement system (Ecopia, HMS 3000) as shown in the schematic diagram of measurement setup in Figure 3.2. Two high purity (99.999 %) calibrated gases from Praxair Inc., 475 ppm NH_3 and 5 ppm NO_2 (both diluted in N_2) were used for the gas sensing experiments.

3.2.2 Gas molecules (NH_3, NO_2) interaction with graphene

To investigate the adsorption induced property change in graphene, the graphene was exposed to a typical electron donating NH_3 (475 ppm) gas molecules and to a typical electron withdrawing NO_2 (5 ppm) gas molecules. During the gas exposure, the change in

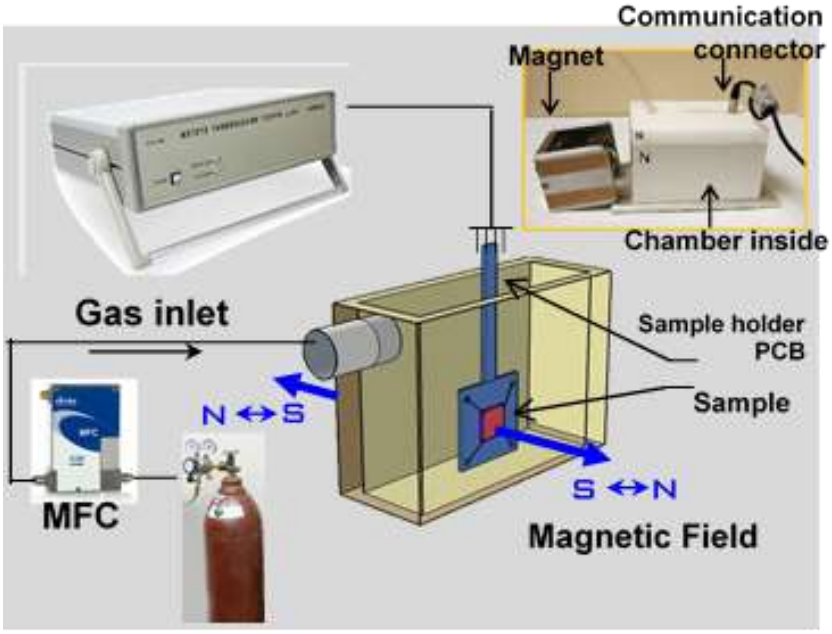

Figure 3.2 Schematic diagram of the Hall measurement set up. The test sample was placed in the closed measurement chamber fitted with a gas inlet.

carrier density and carrier mobility was recorded as a function of time. First, NH_3 gas was introduced into the chamber (consider Fig. 3.2) at a constant flow rate of 50 sccm for 65 min until the electron density and mobility reached steady state values. Then the sample was taken out of the chamber and left to recover in ambient air for over 2 hours. Throughout the exposure and recovery processes, conductivity (σ_{Hall}), carrier density (n_{Hall}) and

mobility (μ_{Hall}) measurements were conducted consistently at intervals of 10 – 30 minutes.

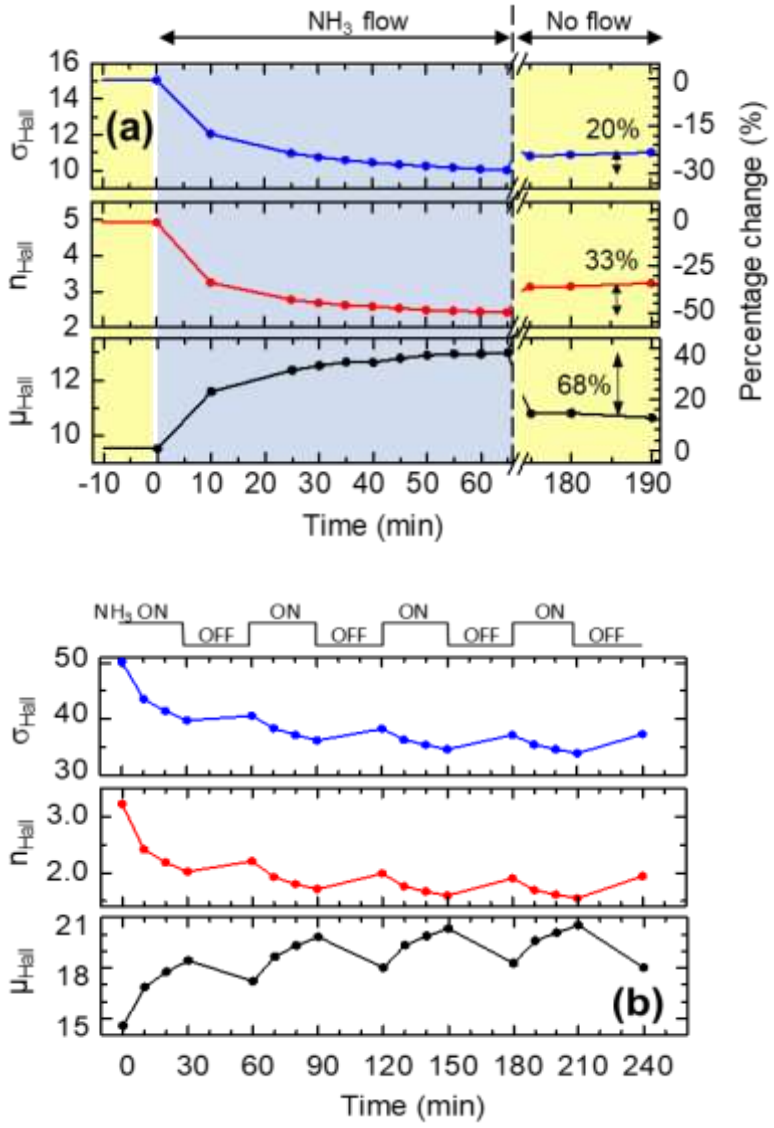

Figure 3.3 Temporal variation in conductivity (σ_{Hall} /10^2 $\Omega^{-1}cm^{-1}$), carrier mobility (μ_{Hall} / 10^2 $cm^2V^{-1}s^{-1}$) and density (n_{Hall} / $10^{12}cm^{-2}$) recorded in response to switching ON and OFF of 475 ppm NH_3 gas flow. a) The gas was flown until their steady state values were reached, followed by recovery in ambient for over 2 hours. The left axes show the actual measured value for each parameter, while the right axes show the corresponding percentage change. b) Variation in conductivity, carrier mobility and density to 4 cycles of NH_3 gas exposure (30 min) alternating with periods of recovery (30 min).

On the plots in Figure 3.3(a), the left axes show the measured values for each parameter, while the right axes show percentage changes. From the plot, we find that the conductivity and carrier concentration monotonically decreases with the time of exposure, and reaches values that are ~30% and ~50% lower than the pre-exposure values, respectively. Since the NH_3 molecule contains $–NH_2$ (amine) group, which is highly electron donating in nature, its adsorption on graphene (originally p-type) upon exposure results in n-type doping [66] and consequent reduction in hole concentration. In contrast to the conductivity and carrier concentration, mobility increases with the duration of NH_3 exposure. This is contrary to the normal expectation that charged impurities, no matter nature, would always result in a reduction of the carrier mobility due to enhanced scattering. Response to cyclical (alternate switching on and off of the gas flow every 30 min) NH_3 exposure to graphene was further studied, and the results are shown in Figure 3.3(b). Once again the conductivity (σ_{Hall}), sheet carrier concentration (n_{Hall}) changed in similar fashion while the Hall mobility (μ_{Hall}) behaved differently.

To investigate the response caused by adsorption of electron withdrawing molecules, we exposed the graphene sample to 5 ppm NO_2 in the same Hall measurement setup. The temporal variations in conductivity, carrier mobility, and concentrations are shown in Figure 3.4. As expected, the carrier concentration (hole) increased upon exposure to NO_2, which is caused by their electron withdrawal nature. The conductivity also increased, however, the mobility showed a decreasing trend. Interestingly, even after stopping the gas flow over 2 hours, the properties of the graphene did not recover, unlike the NH_3 case. This is likely due to the higher adsorption binding energy (by a factor of 2 –

4) of NO_2 compared to NH_3, which results in its desorption rate to be much slower.[67] To facilitate general comparison with other gas sensing results in the literature [68-69] that

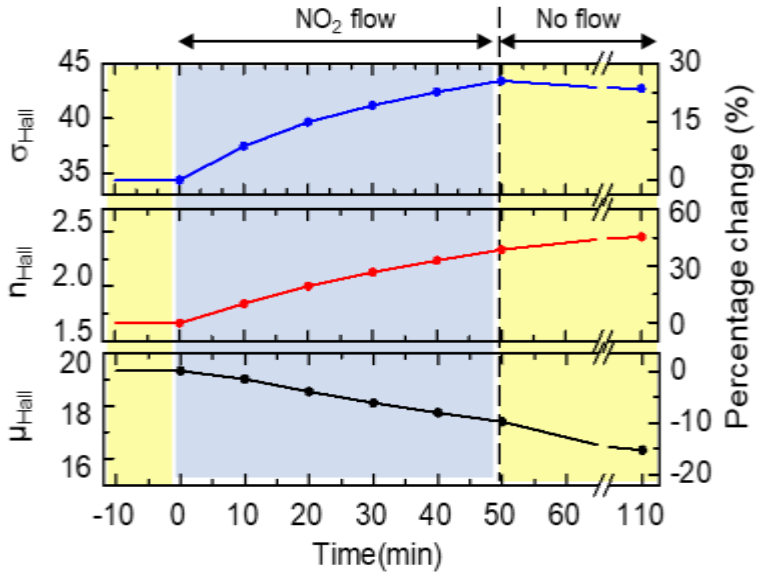

Figure 3.4 Temporal variation in conductivity (σ_{Hall} /10^2 $\Omega^{-1}cm^{-1}$), carrier mobility (μ_{Hall} / 10^2 $cm^2V^{-1}s^{-1}$) and density (n_{Hall} / $10^{12}cm^{-2}$) recorded in response to switching ON and OFF of 5 ppm NO_2 gas flow. The left axes show the actual measured value for each parameter, while the right axes show the corresponding percentage change.

often show the variation in Dirac point as a function of time (upon gaseous exposure), we calculated graphene's Dirac point shift due to molecular doping by NH_3 or NO2 using the correlation between carrier density change Δn and Dirac point shift ΔV_{Dirac}, given as: $\Delta V_{Dirac} = (\Delta n \cdot q \cdot t_{ox}) / \varepsilon\varepsilon_0$ [70], where q is the electron charge, t_{ox} is the SiO_2 thickness (100 nm), ε and ε_0 are the dielectric constant of SiO_2 and vacuum permittivity, respectively. After NH_3 and NO_2 gas exposure for 50 minutes, graphene's Dirac point shifts are calculated to be ~-11 V and ~3 V, respectively, using the above equation (which of course can also be used to plot the Dirac point shifts as a function of time from the Δn variations).

The direction of Dirac point shifts upon NH_3 and NO_2 gas exposures are as expected, since the electron donating nature of the former reduces the Dirac point, while the electron withdrawing nature of the latter does the opposite. The magnitude of Dirac point shifts is also in agreement to those reported by Singh et. al [70] (-6 V and -8 V, respectively for similar concentrations of NH_3 and NO_2) measured directly in a back-gated FET configuration with the same SiO_2 thickness.

From Figures 3.3 and 3.4, we note that the adsorption of NO_2 reduces carrier mobility in graphene, while NH_3 results in an increase. Clearly, the charge on the adsorbed molecules is affecting the mobility. Indeed, it is commonly accepted that the carrier mobility in graphene transferred to SiO_2 is strongly affected by long-range scattering from charged impurities near graphene or trapped at the interface of graphene/SiO_2 (graphene on the SiO_2 substrate participates in a redox reaction that takes place with molecules adsorbed from ambient environment following: $O_2 + 2H_2O + 4e^-$ (from graphene) = $4OH^-$). [55][64][71][72] It is, therefore, reasonable to expect that the charged gas molecules adsorbed on the graphene's surface (after transferred the charge to the graphene) would act as scattering centers affecting the carrier mobility. However, it is interesting to note that the mobility increases as the surface density of positively charged NH_3 molecules increases, and decreases as the negatively charged NO_2 molecular density increases. We propose a simple explanation for this observation considering that the carrier mobility in graphene is affected by an interaction between the following quantities: (i) the total charge density near graphene surface or on SiO_2 substrate (σ_{sub}), (ii) the graphene's charge carrier density (n_s), and (iii) density of ionized gas molecules (σ_{mol}) adsorbed on graphene. The addition of

positively charged NH_3 ions on the surface screens the effect of net negative charge surrounding graphene (which gives rise to its p-type behavior), hence enhances the carrier mobility. On the other hand, the addition of negatively charged NO_2 ions on the surface enhances the electrostatic interaction of the already existing net negative charge around graphene and enhances scattering. Figures 3.5 (a) and (b) show arrays of electrostatic charges σ_{sub}, n_s and σ_{mol}, where the charges on adsorbed NH_3 and NO_2 molecules can reduce or enhance the scattering effect of pre-existing (mostly substrate), charges surrounding graphene.

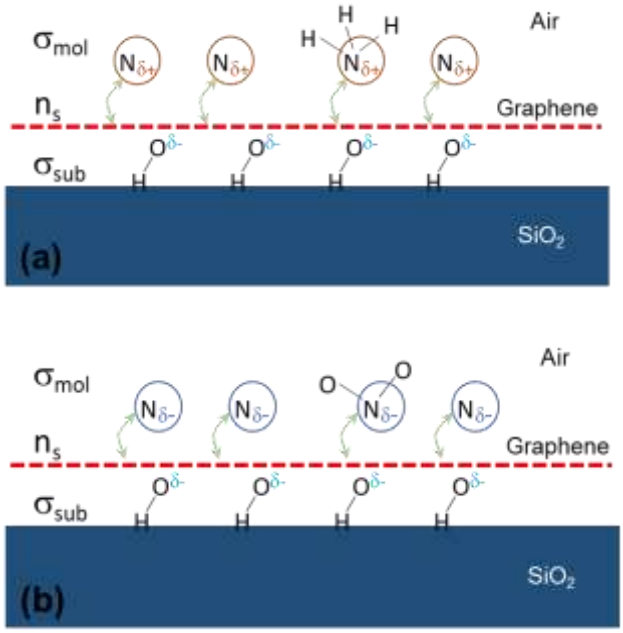

Figure 3.5 Schematic diagram showing electrostatic charge distribution with ionized (a) NH_3 and (b) NO_2, ionized adsorbates, respectively. Pre-existing charged impurities from the interface and substrate (σ_{sub}), the graphene carrier density (n_s), and the charged gas molecules (σ_{mol}) on graphene surface are shown.

The effect of adsorbate charge and dipole moment on screening the effect of scattering electric field from surrounding charges in graphene has been theoretically

modelled by Liang, et al. (Phys. Rev. B, 2014). [73] They found that indeed adsorbate charge or dipole moments can significantly screen the effect of pre-existing charged impurities. However, their work (or any other work to the best of our knowledge) did not investigate the mobility change directly (instead, focusing on conductivity variation) and independently, or compared with experimental results. Additionally, their model is limited to considering only dipolar interaction from NH_3 and NO_2 adsorbates (so that charge density remains constant), which is directly contradicted by our experimental findings of both conductivity and mobility variations.

3.2.3 Response to strong donor type molecules

To further verify our above observations and assertions, we exposed graphene to a much stronger electron donor (than NH_3) trimethyl hexamethylene diamine ($C_9H_{22}N_2$), which has two electron donating functional amine groups (its chemical structure is shown in the inset of Figure 3.6). The idea was to surface dope the normally p-type graphene so strongly n-type that it is transformed to n-type graphene, which offers the opportunity to the study of the electrical parameter variations and their inter-correlations, as a function of time, as the transformation happens. [53] The graphene sample (transferred to a Si/SiO_2 substrate like other discussed above) was exposed to $C_9H_{22}N_2$ vapor by putting a drop in its close proximity, which was followed by measurement of conductivity, mobility and carrier concentration as a function of time approximately 10 mins after exposure. From Fig. 3.6, we find that the exposure started reducing the hole density of graphene quickly which kept dropping and until after ~30 minutes the graphene switched over from p- to n-type. It is important to note that when the graphene was still p-type, the carrier density and

mobility changed in a way similar to what we saw with NH_3 gas exposure i.e. the mobility increased while the carrier density (hole) reduced. After the graphene changed to n-type, and the adsorbed molecules started to desorb, the same trend of mobility and carrier density

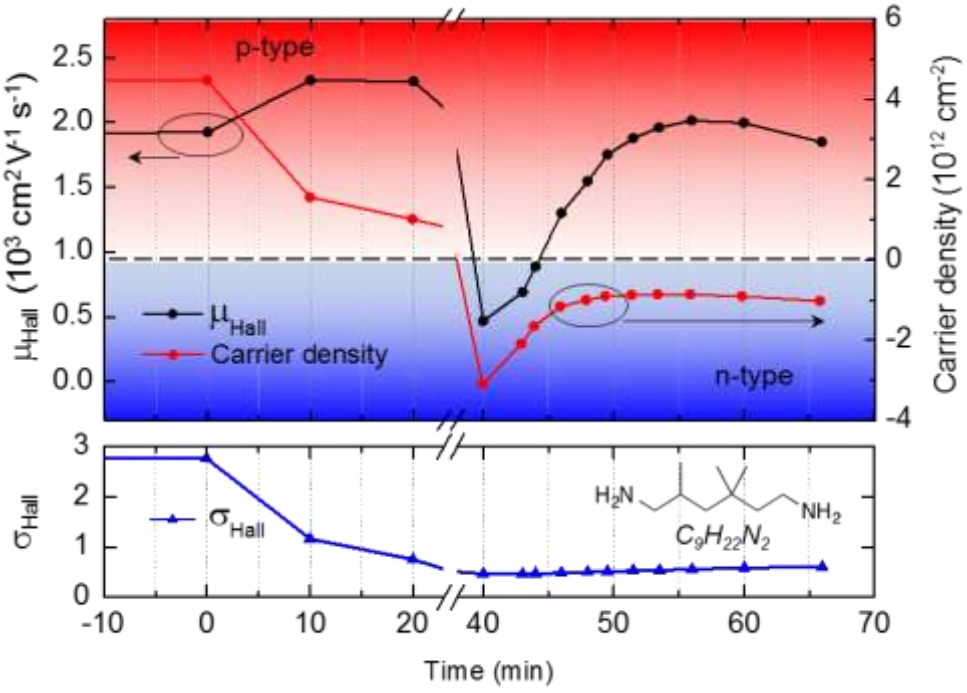

Figure 3.6 Temporal variation in conductivity (σ_{Hall} / 10^2 $\Omega^{-1}cm^{-1}$), carrier mobility (μ_{Hall} / 10^2 $cm^2V^{-1}s^{-1}$) and density (n_{Hall} / $10^{12}cm^{-2}$) recorded in response to exposure to trimethylhexamethylenediamine ($C_9H_{22}N_2$). The top graph shows carrier concentration (n_{Hall}) and Hall mobility (μ_{Hall}) variations, while the bottom one depicts changes in conductivity (σ_{Hall} / 10^2 $\Omega^{-1}cm^{-1}$).

variation was observed. But now with the electron as the majority carrier, when the electron density reduced the mobility found to be increased. It should be noted that this trend has been exhibited for all the three exposures considered in this study, i.e. increase in majority carrier density leads to a strong decrease in mobility, which clearly indicates ionized impurity scattering as a major factor limiting mobility in these devices, which is commonly

observed. [72][74] With mobility increasing more rapidly than the decrease in carrier concentration, the conductivity has a slightly increasing trend, contrary to expectations and observations for NO_2 and NH_3. This exception, however, underscores that the carrier transport properties of electrons and holes in graphene, in response to ionized surface adsorbates, cannot be presumed to follow a simple trend, as has often been assumed in the past; and future sensor development or theoretical modeling efforts must take into account the independent variations of these parameters to gain a deeper understanding of the transport phenomena and benefit from it.

In summary, this chapter reported on individual variations in conductivity, mobility and carrier concentration of graphene under the effect of NH_3 and NO_2 gases and $C_9H_{22}N_2$ vapor exposure, using the Hall measurement technique. It was observed in all three cases of exposure, involving an acceptor (NO_2), a weak (NH_3) and a strong donor ($C_9H_{22}N_2$) that a reduction in majority carrier density resulted in an increase in mobility, and vice-versa, regardless of the type of carriers, as expected for ionized impurity dominated carrier transport. Exposure of p-type graphene to electron donating NH_3 resulted in the screening of negatively charged pre-existing impurities around graphene, resulting in an increase in carrier mobility associated with a reduction in p-type carrier density. On the other hand, exposure to electron accepting NO_2 caused a decrease in carrier mobility with an accompanying increase in carrier density. Exposure to a strong electron donor $C_9H_{22}N_2$ resulted in transformation of p-type graphene into n-type, along with an increasing trend in mobility observed for both n-type and p-type phases as the carrier density reduced. The result clearly underlines the importance of independent determination of carrier mobility

and density, and their impact on understanding transport in graphene, especially in presence of ionic adsorbates. In the following section, this work investigated an intentionally introduced defects' enhancement effect on graphene's gas sensing ability.

3.3 Impact of oxygen plasma treatment on carrier transport and molecular adsorption

As mentioned in the chapter introduction, graphene's unique material properties have led to the investigation of a large variety of sensors for many different applications including chemical and biomolecular detection, ionic detection, as well as infrared and radiation detection.[28][75-78] However, In spite of its widely observed interaction with molecules leading to their physisorption or chemisorption, it is believed that such pristine, not-defective graphene is not very interactive with molecules, and cannot be used to develop highly sensitive sensors.[79] In other words, the defects in graphene contribute to its observed strong interaction with molecules. Indeed, the sensitivity of graphene to analyte molecules is often enhanced with surface functionalization, which may themselves lead to defects in the graphene layer given its atomically thin nature. Using either a solvent assisted process, or sputtered metal oxide or nanoparticle decoration on the graphene's surface, researchers have attempted to modify graphene's electrical properties, and, as such, it's sensing characteristics.[79-81] However, the surface functionalization methods are generally associated with various issues including the agglomeration of graphene layers, bad uniformity for large area dispersion, and processing complexity.[82] Alternatively, plasma treatment of graphene, which also generates defects, can be a simple,

clean, and very effective alternative approach to functionalizing the graphene surface, with the goal of enhancing its sensitivity. Although there are existing reports addressing the chemical and physical effect of plasma treatment on graphene, studies on the direct impact of plasma treatment on the enhancement of molecular interaction capability of graphene and its sensing ability have not been reported yet.

In this section, we conducted a systematic study on the effect of defect introduction in graphene through O_2 plasma treatment, utilizing Raman spectroscopy, Hall measurements, and XPS analysis. A carefully controlled O_2 plasma exposure of graphene led to significant changes in transport property and a strong improvement in the rate and extent of interaction with NH_3 molecules. An empirical model proposed to estimate carrier mobility in plasma treated graphene showed very good agreement with experimental results.

The graphene used in this study was synthesized using CVD as discussed in Chapter 2. The graphene was then transferred onto a SiO_2/Si substrate using the wet transfer process. For Hall measurements, Ti/Ni metal stacks were deposited at the four corners of 6×6 mm graphene on SiO_2 substrate using a shadow mask. Hall measurements were conducted using a commercial set up HMS 3000 (Ecopia, Inc.) retrofitted with gas flow tubes and mass flow controllers. This system allows Hall measurements to be conducted in desired gaseous environments. Further details about the setup can be found in an earlier report.[83] To study the effect of plasma treatment on the molecular interaction property of graphene, it was exposed to 475 ppm NH_3 gas diluted in N_2 sequentially after various durations of plasma treatment. The oxygen plasma was generated with a plasma etch

system PE25-JW (Plasma Etch, Inc.) with a starting pressure of 200 mTorr before flowing oxygen gas. The graphene was plasma treated for 2 – 14 s at a power of 37.5 W, with a constant 15 sccm oxygen flow. To determine the quality of post-exposure graphene, Raman spectra were obtained with 532 nm excitation wavelength (InVia, Renishaw plc.) before and after various durations of O_2 plasma treatment and compared. Also, X-ray photoelectron spectroscopy (XPS) (VersaProbe III, Physical Electronics, Inc.) was used to investigate the graphene's surface chemical composition variation caused by the plasma treatment.

3.3.1 Domain Size Change Induced by Plasma Treatment

Figure 3.7 compares the Raman spectrum of the initial untreated graphene with O_2 plasma treated graphene with exposure durations of 2, 6, and 10 seconds. The three main peaks of graphene, i.e. D, G and 2D can be found in each spectrum. The initial graphene exhibits intensity ratios of $I_{2D}/I_G \approx 2.2$ and $I_D/I_G \approx 0.06$, which indicates that its monolayer nature and high quality are preserved even after transfer to the SiO_2/Si substrate. [51] When exposed to low power O_2 plasma (carefully avoiding over damage), a gradual change in Raman spectroscopic characteristics is observed as a function of exposure time. We find that the I_{2D}/I_G is reduced monotonically from initial 2.2 to 1.7, 1.3, and finally to 1.2; while the I_D/I_G values increased from 0.06 to 0.35, 0.68, and 1.05 corresponding to the exposure durations of 2, 6, 10 s, respectively. Even though $I_{2D}/I_G \approx 1$ is widely accepted as an indication of double-layer graphene, in this case, it is caused by suppression of the lattice vibration mode induced by defects in single layer graphene.[84] Along with disordered sp^2-bond induced high rising of D peak, two other peaks D' (~1620 cm^{-1}) and D+D' (~2940

cm^{-1}) can also be observed after 6s plasma exposure, which is consistent with previous observations.[84] From the increasing disorder peaks, we can conclude that even though with very low plasma exposure power and duration, it induced significant damage to the graphene's atomic structure. The domain size in defective graphene, which is an important parameter determining short-range scattering, can be calculated from the intensity ratio I_D/I_G. Using the relationship $I_D/I_G = C'(\lambda)/L_d^2$, proposed by Lucchese et al. [85] and utilizing the Tuinstra-Koenig relation (where $C'(\lambda)$ is given as 102 nm^2 for 514 nm laser excitation), we estimate the defective graphene's nanocrystalline domain size, L_d, of 49.0, 17.0, 12.3, 9.8 μm for 0, 2, 6, 10 s plasma treatment, respectively.

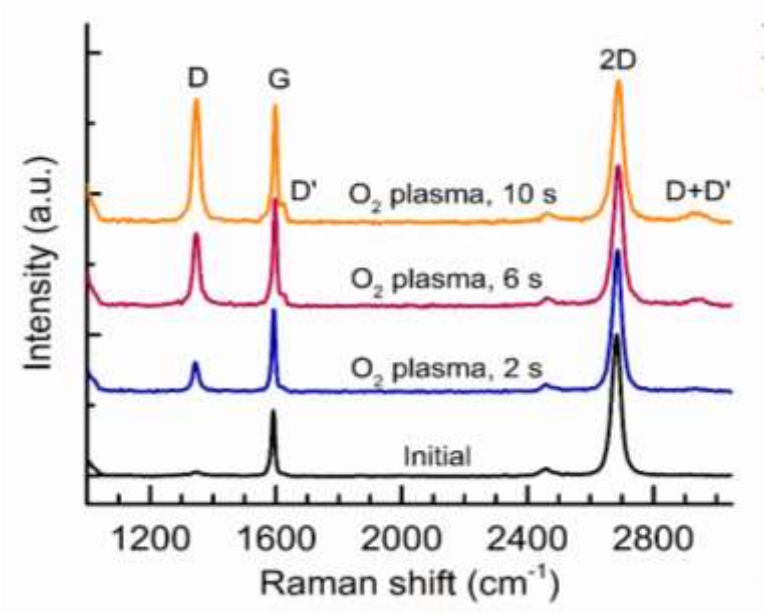

Figure. 3.7 Raman spectra of initial graphene (bottom), and O_2 plasma treated graphene for durations of 2 s, 6 s, 10 s, are compared. The observed reduction of 2D/G peak intensity ratio and increase in the magnitude of the D peak is by O_2 plasma treatment induced disorder in graphene's atomic structure.

3.3.2 Carrier Transport Property Change Under NH_3 Exposure

To further investigate the effect of O_2 plasma treatment on the graphene's interaction with gaseous molecules, its response to 475 ppm NH_3 exposure was recorded using the Hall measurement system, which simultaneously yields conductivity (σ), carrier density (n_s) and mobility (μ_{Hall}). NH_3 gas was flown over the sample and alternately switched on and off for 10 mins duration, to record the changes in electrical characteristics and recovery. The values of conductivity, carrier density, and mobility measured after every few minutes using the Hall system are plotted in Fig. 3.8. From the plot, graphene's carrier (hole) density drops with the NH_3 exposure, which is expected since NH_3 is a typical electron donor for graphene.[63][83][86] Interestingly, mobility increases with NH_3 adsorption on graphene, which is consistent with what has been discussed in the previous section. When NH_3 molecules interact with graphene, they lose electrons and become positively charged impurities. Typically, ionized impurities on graphene's surface affect its carrier transport properties by inducing carrier scattering which can cause a reduction in mobility. However, in this case, instead of decreasing mobility, the positively charged NH_3 ions screen the scattering effects of the negatively charged ionized impurities present initially on graphene (commonly observed in graphene transferred on SiO_2 [65]). This screening process and consequent increase in mobility have been explained in detail in the last section 3.3. The conductivity, which is proportional to the product of carrier density and mobility, follows the same trend as carrier density, which shows a proportionally higher change compared to mobility. Comparing the responses corresponding to the

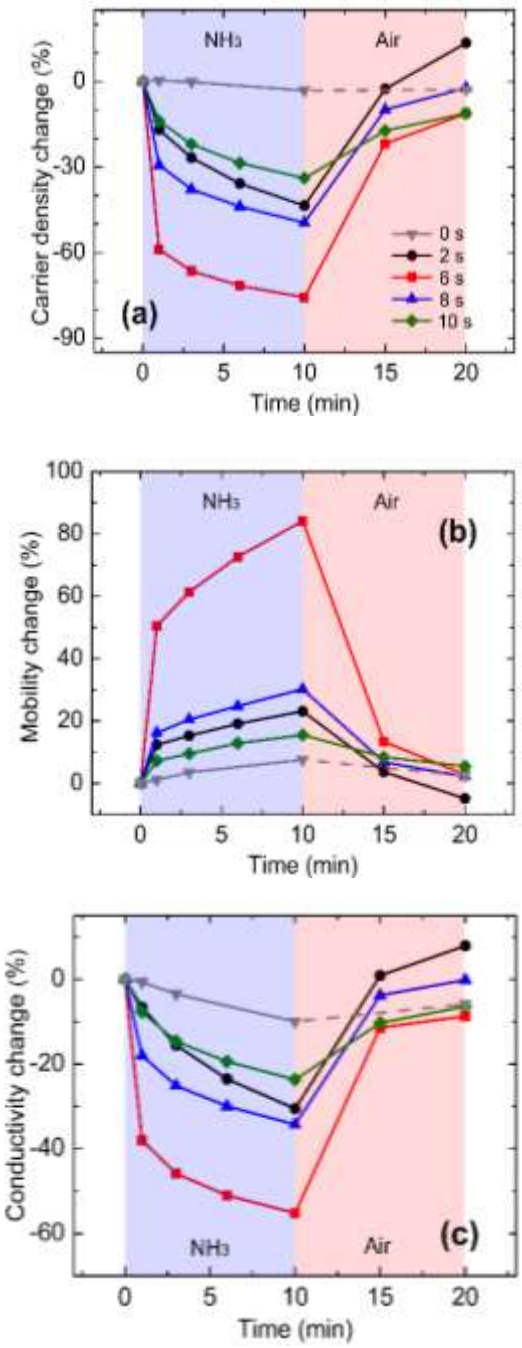

Figure. 3.8 O_2 plasma treated graphene's response to 475 ppm NH_3 gas in terms of (a) carrier density, (b) mobility, and (c) conductivity, for 0 – 10 s of plasma exposure. Maximum response is observed for 6 s exposure for all three parameters. Dotted grey line indicate expected recovery transient estimated from longer duration measurements.

various duration of plasma treatment, we find that the changes in conductivity, carrier

density, and mobility increased initially, reached the highest level (55%, 76%, and 84%, respectively) for the 6s plasma treated graphene, and then kept reducing for 8 and 10 s exposure durations. Figure 3.8 shows that the response rate for 6s plasma treated graphene is the fastest, with more than half of the maximum response occurring within the first minute, while the response magnitudes (for all three parameters) are also comparatively much higher. The transients for initial graphene is also shown for reference (recovery

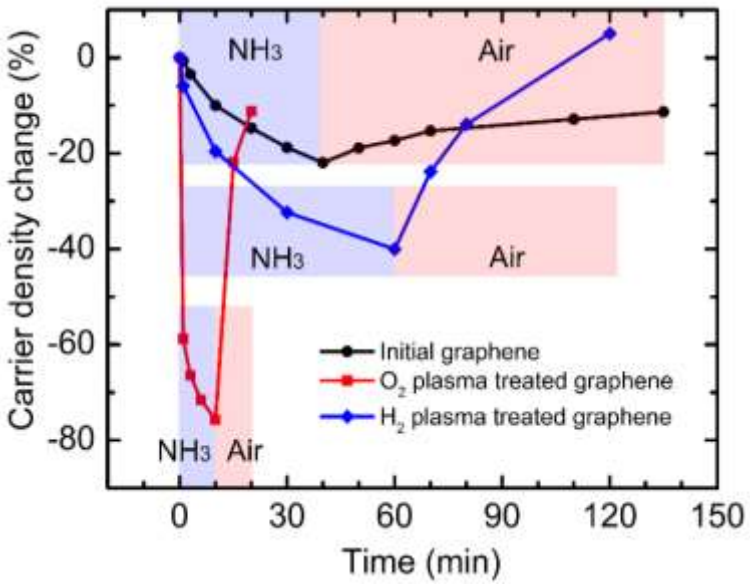

Figure. 3.9 Comparison of the response (percentage carrier density change measured by Hall system) toward 475 ppm NH_3 between untreated graphene, 6 s O_2 plasma and 2 s H_2 plasma treated graphene. Both the magnitude and rate of response are very significantly enhanced after O_2 plasma treatment, while only a minor improvement is noticed after H_2 plasma treatment.

transient estimated from longer duration measurements, which is discussed below).

Although the 6s exposure led to the best response and exposing graphene for more or less time to O_2 plasma led to a reduced response to NH_3, those are still better than the untreated graphene's response. Indeed, comparing the initial untreated graphene's and

plasma treated (6 s) graphene's responses to NH_3 gas (shown Fig. 3.9 with moderate sensing performance for each sample), we find that O_2 plasma treated graphene's sensing performance improved dramatically both in response magnitude (increased over 750 % over the first 10 min exposure) and response rate (reduced 40 times considering the initial 20 % change). H_2 plasma treatment also showed some enhancement effect on graphene's

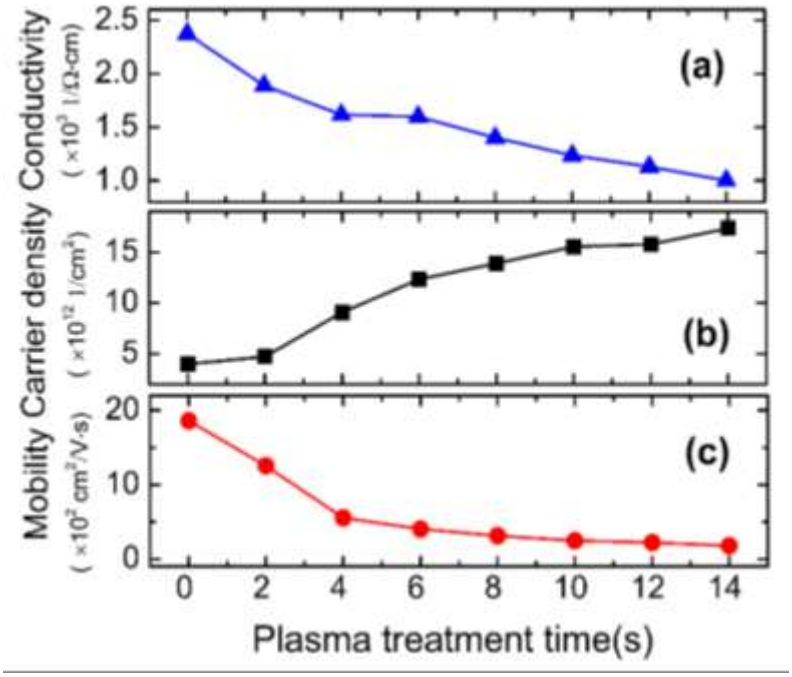

Figure. 3.10 Variation in (a) conductivity, (b) sheet carrier density, (c) carrier mobility in graphene as a function of O_2 plasma treatment time. We find the carrier (hole) density increases, while the mobility and conductivity (proportional to the product of mobility and carrier density) decreases monotonically with exposure time.

NH_3 sensing as shown in Fig. 3, the details will be discussed further in the following sections.

3.3.3 Carrier Transport Property Change by Plasma Treatment

Figure 3.10 shows the variation in graphene's electrical properties due to O_2 plasma treatment as a function of treatment time. We find that the carrier density increases monotonically while conductivity and mobility decrease as the treatment time is increased from 0 to 14 s. From the Raman spectroscopy results discussed above, a reduction in mobility is expected, due to increased scattering effect from increased disorder and nano-crystalline domains formed in graphene due to plasma treatment. On the other hand, the increased carrier density can be attributed to an increase in oxygen adsorption on the graphene surface following plasma treatment, as reported in earlier studies.[84][87-88] Keeping in mind the very low power and plasma exposure time, XPS studies were carried

TABLE 3.1. Changes in carrier mobility, density, and conductivity of graphene following 4 s O_2 and H_2 plasma treatments.

Graphene Parameter		μ ($cm^2V^{-1}s^{-1}$)	n_s ($10^{12}/cm^2$)	σ ($\Omega^{-1}cm^{-1}$)
H_2 plasma treatment	Before	1.7×10^3	2.9	1.6×10^3
	After	7.3×10^1	1.8	4.1×10^1
O_2 plasma treatment	Before	1.7×10^3	3.0	1.7×10^3
	After	2.8×10^2	12.5	1.1×10^3

out to confirm if indeed such an increase in oxygen bonding on the graphene surface occurred. In addition, since exposure to H_2 plasma is expected to act in an opposite way to O_2 plasma exposure, we also performed electrical and XPS characterization on H_2 plasma treated graphene samples, and the XPS spectra and carrier transport characteristics were compared between initially untreated, O_2 plasma treated, and H_2 plasma treated graphene.

Table 3.1 summarizes the effects of O_2 and H_2 plasma treatment (at 37.5 W power level for a duration of 10 s and 4 s, respectively) on the conductivity, mobility, and density of the carriers in graphene. We find from Table 3.1 that both O_2 and H_2 plasma treatment reduces carrier mobility in graphene. In contrast, however, the H_2 plasma exposure reduces carrier density by ~39% in graphene, while O_2 plasma exposure increases it by ~310%. As discussed above, the mobility reduction can be attributed to an increase in disorder and nano-crystalline domains formed in graphene, as revealed through Raman spectroscopy, and is expected to result, in general, from plasma exposure irrespective of the gaseous species (and corresponding ions) involved. On the other hand, a reduced carrier density by H_2 plasma treatment (unlike an increase in case of O_2 plasma treatment) can be explained considering the formation of C-H bonds or removal of oxygen bonds through reacting with pre-adsorbed oxygen on the graphene surface, both of which can result in an n-doping effect. [89-90]

3.3.4 Elemental Composition Analysis and Comparison

The validity of the proposed mechanisms for change in carrier density due to an increase or decrease in adsorbed oxygen (due to O_2 and H_2 plasma treatments, respectively) was tested through XPS spectroscopic studies. For this, a graphene sample (on SiO_2 substrate) was split into two pieces, with one subjected to O_2 plasma and the other to H_2 plasma treatment. C1s XPS spectra of initial graphene, O_2 plasma treated graphene, and H_2 plasma treated graphene were taken and are shown in Fig. 3.11. The spectra are fitted to Gaussian curve peaks of sp^2 bonds, sp^3 hybridization, as well as, C-OH, and O-C=O at binding energies of ~284.6, ~285.6, 286.6 and 288.8 eV, respectively. The ratios of area

under the respective Gaussian curve (for C-OH and O-C=O curves) were calculated and the percentages are shown in the figure, from which we find that the O_2 plasma treatment caused an increase in the ratio of adsorbed oxygen (15.5 + 13.0 = 28.5%) in graphene while

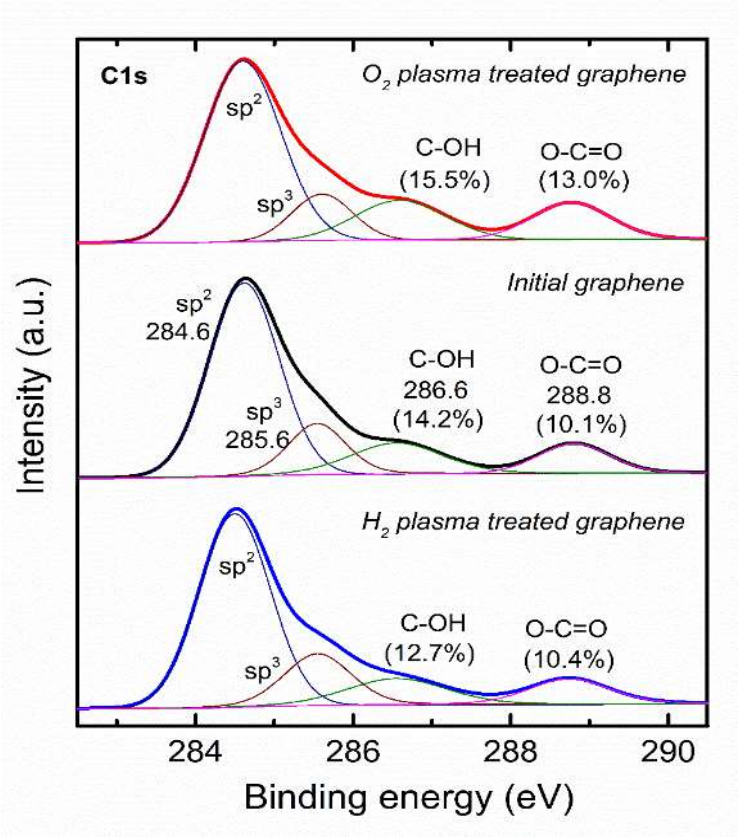

FIG. 3.11. Comparison of the C1s XPS spectra of untreated graphene (black, center panel), O_2 plasma treated graphene (red, top panel), and H_2 plasma treated graphene (blue, bottom panel). The fraction of area of the curves showing adsorbed oxygen in graphene (C-OH and O-C=O bonds) can be seen to be significantly higher after O_2 plasma treatment, but lower after H_2 plasma treatment.

H_2 plasma treatment reduced it (12.7 + 10.4 = 23.1%), compared to the initial untreated graphene (14.2 + 10.1 = 24.3%). These results clearly indicate that even with very low power and short duration of plasma exposure, both O_2 and H_2 plasma could significantly

affect the ratio of pre-adsorbed oxygen on the graphene surface, causing the observed change in carrier density as discussed above. The relative magnitude of changes in carrier density (which are in opposite directions), following O_2 and H_2 plasma treatments (Table 1), also correlate well with the changes in the ratio of oxygen in graphene following the plasma treatments. We also note that a similar approach for inducing p-doping graphene, through the formation of carbon-oxygen bonds (C-O or C=O), by activation of O_2 with UV light, has been reported recently. [90]

As discussed earlier, plasma treated graphene exhibit a significant enhancement in its interaction with NH_3 molecules. The Raman and XPS studies indicate that after plasma treatment the graphene crystalline structure gets significantly altered, as well as the ratio of absorbed oxygen on graphene increases. The enhancement in interaction with NH_3 and related enhancement in sensing property can be attributed to two major factors: structural damage and consequent enhancement in adsorbed oxygen caused by plasma treatment, and change in Fermi level due to enhanced p-type doping. From earlier reports, the domain edges of graphene (offering so-called "dangling bonds") created by plasma treatment can provide a large number of additional vacant sites for NH_3 molecules to attach, and the ensuing higher charge transfer can strongly change the conductivity as well as sensitivity. [91] In addition, an increase in bonded oxygen species on graphene (see earlier discussion on XPS results) also plays a significant role in enhancing graphene's sensitivity to NH_3. *Lee et al.* reported density functional theory (DFT) calculations on graphene in which they found a much lower NH_3 adsorption energy (E_{ads}) at bonded oxygen species (-0.16 ~ 0.25 eV) sites compared to the vacancy sites (-1.48 eV) in graphene (see the referred paper for

schematic structures of adsorption).[91] A lower E_{ads} indicates a faster and easier adsorption process for the NH_3 molecules. Thus, the oxygen plasma treated graphene facilitates adsorption of NH_3 molecules on its surface, and when coupled with water vapor (from ambient as well as at the graphene/SiO_2 interface due to wet processing) they subsequently interact with graphene and transfer charges. [92] Indeed for H_2 plasma treated graphene, which led to a decrease in adsorbed oxygen (see above discussion) the carrier concentration was reduced leading to only slightly higher sensing performance (20% change in 10 min, 32% change in 30 min; refer to Fig. 3.9) compared to that of the pristine graphene (10% change in 10 min, 19% change in 30 min). Here the effect of the increase in domain edge dangling bonds contributed to enhanced sensitivity, but the reduction in adsorbed oxygen (from H_2 plasma treatment) did not offer any additional enhancement in sensitivity (unlike O_2 plasma treatment), and may even have reduced it to some extent.

The second factor causing sensitivity improvement is related to the downward movement of the Fermi level in graphene due to enhanced p-type carrier density (Fig. 3.10). In earlier research, Singh et al. reported that the graphene's sensitivity to NH_3 can be enhanced by increasing the p-type doping in it by application of a negative gate voltage in a back-gate transistor configuration. [70] This is because the energy gap between the defect state induced by adsorbed NH_3 and the Fermi level in graphene increases as the latter one moves down due to high p-type doping. Since the carrier density in the graphene increases significantly after O_2 plasma treatment, the Fermi level also moves lower significantly, increasing the gap with NH_3 donor states, and hence enhancing sensitivity. Following the similar argument, NO_2, which is a well-known acceptor molecule in graphene, shown

having its sensitivity affected only minimally after oxygen plasma treatment, as the energy gap between the acceptor state induced by NO_2 reduces as the graphene becomes more p-type, which reduces the charge transfer between those states.[70] This was indeed observed experimentally, where graphene's sensitivity to NO_2 molecules did not show noticeable improvement as to NH_3 with oxygen plasma treatment.

In conclusion, this section has demonstrated a strong influence of oxygen plasma treatment on carrier transport properties of graphene and its ability to interact with gaseous molecules such as NH_3. Raman spectroscopic measurements indicate the formation of smaller nanocrystalline domains with increasing duration of plasma exposure of graphene, while, XPS measurements indicate an enhancement in the fraction of adsorbed oxygen. Hall measurements demonstrate a carrier mobility reduction following plasma treatment that is attributable to enhanced short-range scattering and an increase in carrier density resulting from a higher fraction of adsorbed oxygen on graphene. The magnitude and response rate for NH_3 molecule sensing, increased dramatically with plasma exposure, with a peak enhancement recorded after 6 s of exposure. With the knowledge of graphene's carrier transport characteristics, the graphene-based field effect transistor has been fabricated in this study and demonstrated highly sensitive ion sensing application, which will be discussed in the following chapter.

CHAPTER FOUR

GRAPHENE BASED ION-SENSITIVE FIELD EFFECT TRANSISTOR

4.1 Why K^+ ion sensor?

A variety of important functions are closely dependent on electrolytes in the living body. They regulate the fluid levels in the blood plasma, assist in nerve system excitability, aid in endocrine secretion, control membrane permeability, balances pH level, and adjust transmission of fluids between compartments. The levels of electrolytes can be observed in the blood, urine, tissues, and other body fluids. As mineral electric charges, the variety of electrolyte is determined by the type of ions it contains, which includes sodium, calcium, potassium, chlorine, phosphate, magnesium, copper, zinc, bicarbonate, iron, manganese, molybdenum, and chromium in living systems. Among those ions, six electrolytes or ions

Table 4.1 Important ions in the human body and their reference values[93]

Name	Chemical symbol	Plasma	CSF* (mM)	Urine
Sodium	Na^+	136.00–146.00 (mM)	138.00–150.00	40.0–220.0 (mM)
Potassium	K^+	3.50–5.00 (mM)	0.35–3.5	25.0–125.0 (mM)
Chloride	Cl^-	98.00–107.00 (mM)	118.0–132.0	110.0–250.0 (mM)
Bicarbonate	HCO_3^-	22.00–29.00 (mM)	——	——
Calcium	Ca^{2+}	2.15–2.55 (mM/day)	——	Up to 7.49 (mM/day)
Phosphate	HPO_4^{2-}	0.81–1.45 (mM/day)	——	12.9–42.0 (mM/day)

*Cerebrospinal fluid

are most important in terms of body functioning. The ions and their reference values for blood plasma, cerebrospinal fluid (CSF), and urine are listed in Table 4.1. Disorders of electrolytes levels can cause corresponding symptoms and sickness, also a certain disease

can result in an imbalance of electrolytes normal value. Therefore, the information on ion concentrations in physiological fluids is important for disease diagnosis and prognosis. As potassium ion sensor is one of the main interests of this paper, more detailed biological functions of potassium ions in human body will be discussed in the following few paragraphs.

Heart disease has been the leading cause of death worldwide, taking up almost 25 % of the mortality rate in the United States (from CDC, 2017). This is also because of its unpredicted occurrence outside a hospital, and short react time (3~4 hours) before causing permanent death of heart muscles. Due to the data released from the American heart association (AHA) in 2018, only 27.5% was survived from sudden cardiac arrest when the patients were in homes/residences. There are widely known several signs prior to a heart attack including nausea, cold sweat, fatigue, tightness of muscle and etc., however these symptoms are sometimes can be very confusing with other diseases and couldn't bring enough attention. Other than the subtle signs, there is a more accurate way to warn a heart failure directly from extracellular fluid from heart muscles. It is the rapid rise of K^+ ion concentration.

As the major intracellular cation, potassium has very critical functions in various biological processes, like regulation of membrane potential of biological cells, maintenance of the acid-base balance of cells, regulating heart rate, and action potential in nerve cells. When the potassium level is too low in blood, also called hypokalemia, it can cause hyperpolarization of the cell membranes of neurons, reducing the responses to stimuli. On the other hand, when the potassium level is abnormally elevated in blood

(Hyperkalemia) it can result in a partial excitation of the plasma membrane of skeletal muscle fibers, neurons, and cardiac cells of the heart, and can also lead to an inability of cells to repolarize. So a person with hyperkalemia may exhibit mental confusion, numbness, and weakened respiratory muscles. Especially for the heart, this means that it won't relax after a contraction, and will effectively "freeze" and stop pumping blood, which is fatal within minutes as discussed its high mortality rate in earlier paragraph. Similarly, another very dangerous and unpredictable sudden trigger of loss of awareness is epilepsy or seizures. Because of the recurrent, unprovoked, it affects patient safety, work, driving and many aspects of life. As a kind of disorder of central nervous system, a neuronal discharge induced high K^+ accumulation precede the symptoms, which means by K^+ ion monitoring for the extracellular of brain cells epilepsy can be predicted prior to people losing full awareness.[93] So there is more and more demand for potassium ion concentration monitoring of human body on prevention and rehabilitation purposes in clinic and medical care.

To understand the traditional method of K^+ ion concentration in the cellular base, here is a brief introduction of biophysics and the role of K^+ ions in cellular base. First of all, the heartbeat, muscle contraction, and eyes processing of light and color are all controlled by excitable cells. A variety of excitable cells exists in the human body, specialized for different type of performance. Then, to perform activities, those excitable cells change their electrical properties – action potential, which is a transient, rapid rise and fall of the membrane voltage that can modulate cells excitability or contractility or other corresponded mechanical functions. Ion channels are pore-forming membrane proteins

located on the cell membrane, in charge of ion transportation through the channel pore. There are tremendous kinds of ion channels in living body and they modulate the ionic concentrations either in or outside of membrane, which is also through what the excitable cells obtain action potentials. [94] K^+ ion channels are the most widely distributed type of ion channel and play essential and critical functions in a wide variety of biological processes.

To study the ion transition in the medical, toxicological, and drug discovery research, a number of measurement techniques have been developed. Among all of them, binding assay, ion flux assay, fluorescent dyes based assay, and patch-clamp are widely used techniques, while patch clamp is the most popular and adopted one. Most of the techniques that need scintillation in the process are susceptible to a huge imaging artifact, which also means indirect measurement of ion channel activities. On the other hand, patch-clamp directly measures the electrical signal of ion channels without any assisting molecules diffused in the target cells, which make it as the "gold standard". [95] A diagram of a commonly used whole cell patch-clamp technique is shown in Figure 4.1.[96] There are two electrodes in the patch-clamp set-up, one is a recording electrode inside the glass pipette and the other one is a reference electrode in the bath solution. A micro positioner is used to move the micropipette tip (1~3 μm) onto the surface membrane of an individual cell. Then a mild suction is applied to form a high resistance electrical seal between the glass and the patch of membrane, by which electrical isolation of the membrane patch is obtained (consider inset of figure 4.1). This managed to have electrical continuity between the pipette electrode and the cell, therefore allows the membrane potential to be precisely

controlled. The currents passing through the cell membrane can be recorded with reference electrode in the bath medium, while the recorded value represents the overall activity of all

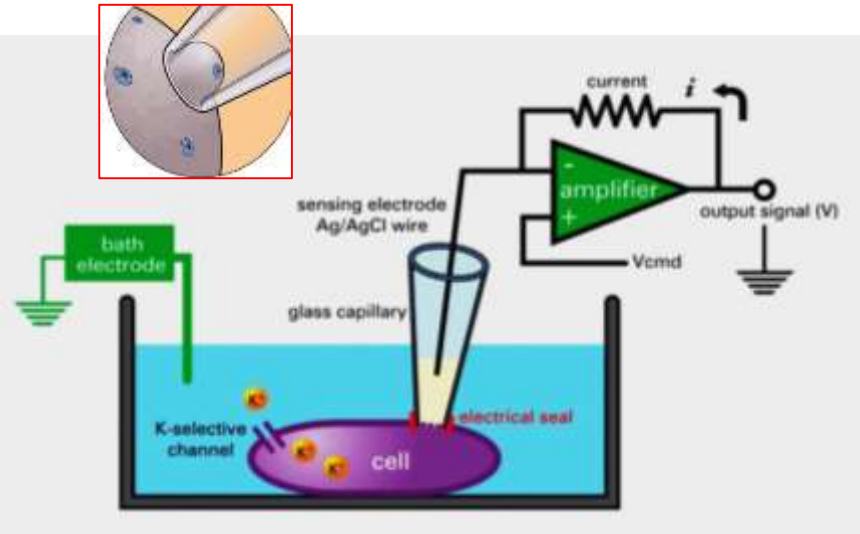

Figure 4.1 Schematic diagram of whole cell patch clamp technique. [19]

channels expressed in the plasma membrane. However, even though patch clamp is a very powerful technique to investigate the kinetics of ion channels directly with electrical signal, this traditional technique is far from suitable for multiple compound screening due to it is too highly specialized, technically demanding skillful operation, very low throughput, and labor-intensive for large number processes. So a new alternative assay technique to meet the high throughput need in pharmaceutical industry for drug discovery was demanded.

In 1970, the first ion sensitive field effect transistor (ISFET) was introduced in a short communication, following a full paper in 1972 with recorded data of ionic signal in the effluxes around a nerve.[97-98] Since these first historical publications, this noninvasive approach to study ion channel activities, that not only measures electrical

potentials but also ion concentrations, has drawn a lot of interest. The ISFET basic structure

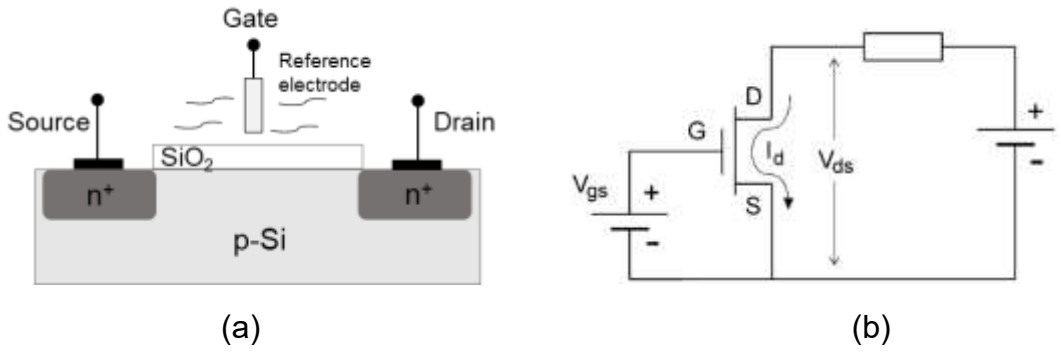

Figure 4.2 Schematic of (a) ISFET, and (b) its electronic model diagram. [99]

diagram and its electrical model are shown in Figure 4.2.[99] From the diagram, we can find that the ISFET is, in fact, nothing but a MOSFET with the gate replaced by a reference electrode in an aqueous solution from a back gate on the chip. So the general expression of the drain current for both MOSFET and ISFET in the non-saturated mode is given by Equation 4.1,

$$I_d = C_{ox}\mu\frac{W}{L}\left[\left(V_{gs}-V_{th}\right)V_{ds}-\frac{1}{2}V_{ds}^2\right] \tag{4.1}$$

where C_{ox} is the oxide capacity per unit area, W and L are the width and the length of the channel, respectively, and μ is the electron mobility in the channel. And the following Equation 4.2 is the general expression for the threshold voltage of MOSFET.

$$V_{th} = \frac{\Phi_M - \Phi_{Si}}{q} - \frac{Q_{ox}+Q_{ss}+Q_B}{C_{ox}} + 2\phi_f \tag{4.2}$$

Where the first term describes the difference in work function between metal and silicon, the second term is due to the accumulated charge in the oxide, at the oxide-silicon interface, and the depletion layer in the silicon, respectively. In case of the ISFET, following the electrical model (Figure 4.2 (b)), similarly, the interfacial potential induced from remote

gate in aqueous medium (reference electrode) is described in terms of threshold voltage V_{th}. Thus, the backside metal's work function is not there anymore, instead the constant potential of the reference electrode (E_{ref}), and the interfacial potential at the solution/oxide interface was given as the sum of the surface dipole potential of the solvent (χ^{sol}), and the surface potential (Ψ) induced from electrical double layer and surface proton buffer at oxide-water interface. As a result, the expression for the ISFET threshold voltage is given as Equation 4.3.[99]

$$V_{th} = E_{ref} - \Psi + \chi^{sol} - \frac{\Phi_{Si}}{q} - \frac{Q_{ox} + Q_{ss} + Q_B}{C_{ox}} + 2\phi_f \qquad (4.3)$$

From the basic theoretical introduction, we can conclude that similar to MOSFETs in the structure and operating principle, the ISFETs threshold voltage can be modulated by the oxide/solution interface potential. Thus, the ion concentration of the solution can be measured by the means of ISFETs electrical property (current, threshold voltage) by changing its interface potential. The introduction of the FET concept in the ion sensing application opened a new research field of ion sensors, and furthermore, new techniques for the ion channel activity study. The ISFETs have not stopped at the primary silicon oxide based pH sensing device, a variety of insulating materials have been investigated for a better sensing performance. Later, polymer-based ion selective membrane was combined to the ISFET concept, provided a very important feature of sensors – ion selectivity. In addition, the introduction of a bio-recognition layer at the surface, ISFETs were developed to BioFETs to detect biomolecules or chemical analytes. Furthermore, on the purpose of high throughput, CMOS technology was used in ISFETs fabrication to get micro- ISFET array, which can perform multiple-cell, synchronized assays.

This chapter will present a highly sensitive and selective graphene-based ISFET (GISFET) capable of detecting K^+ ions down to 1 µM (utilizing valinomycin based membrane coating), showing excellent selectivity with respect to common interfering Na^+ and Ca^{2+} ions at several orders of magnitude higher concentration. The feasibility of using graphene-based ISFETs for bio-implantable applications was also studied by testing them in the Tris-HCl solution and fabricating them using PET substrate, which is inert and highly bio-compatible. The devices showed high repeatability and reliability in sensing experiments conducted over a period of two months.

4.2 Fabrication of Graphene FET

Charge carrier mobility is an important parameter directly affecting the sensitivity of the graphene ISFET device. Therefore, a back-gated FET is fabricated and measured the

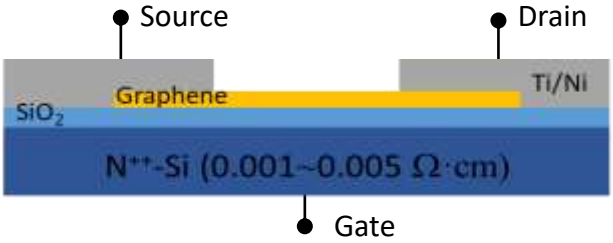

Figure 4.3 Schematic of graphene FET with n^{++}-Si back gate.

graphene's FET mobility first before moving on to GISFET device fabrication. For measuring FET mobility, Ti/Ni metal stacks were deposited on the transferred graphene to form source and drain contacts with a graphene channel of dimension 2.8 x 1.5 mm. The highly doped silicon substrate with a resistivity range between 0.001 and 0.005 Ω·cm was

used as the back gate with 300 nm SiO_2 as the gate oxide. The schematic of the cross-section is shown in Figure 4.3. This FET's transfer characteristic $I_{ds} - V_{bg}$ and $I_{ds} - V_{ds}$ are measured and the plotted in Figure 4.4. From Figure 4.4 (a), the $I_{ds} - V_{bg}$ curve is ambipolar

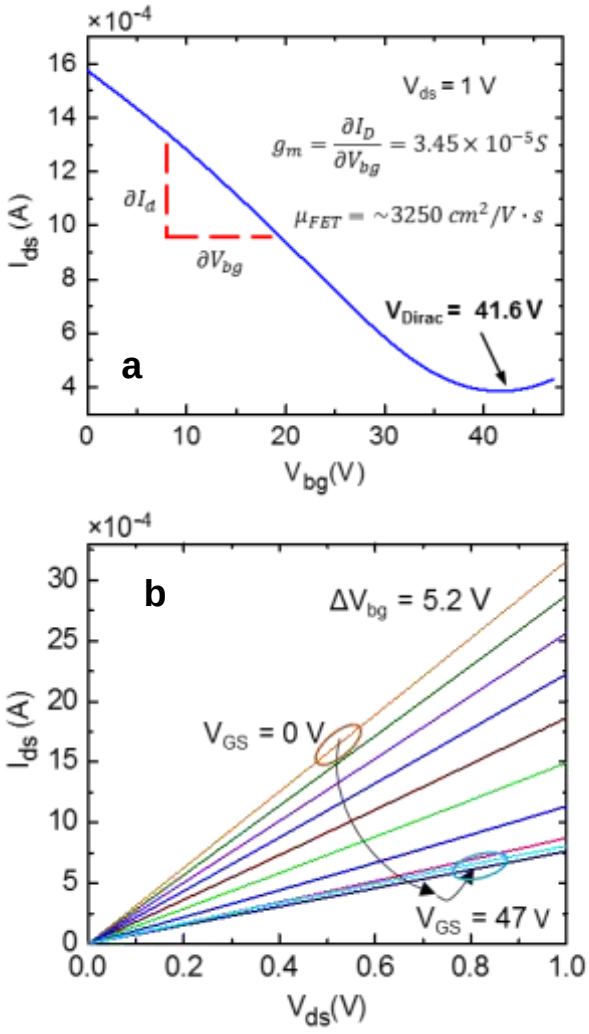

Figure 4.4 (a) Graphene FET mobility extraction. Graphene's $I_d - V_{bg}$ characteristic is measured from graphene FET device; the plot showing graphene's typical V-shaped characteristics. (b) A family of $I_{ds} - V_{ds}$ plots is shown with varying back gate voltage (V_{bg}).

in nature which is a direct consequence of linear dispersion relation in graphene with zero bandgap (discussed in Chapter 1). The Dirac point was observed at V_{bg} = 41.6 V. A positive

Dirac point indicates that CVD grown graphene transferred on SiO_2 is p-type in nature, which is expected and commonly observed.[23][53] The Figure 4.4(b) shows a linear I_{ds} – V_{ds} family of curves where the back-gate bias varies from 0 to 47 V at a V_{bg} increment of 5.22 V. A good back gate modulation was observed (supporting expected p-type graphene behavior), and the FET hole mobility was calculated using the formula $\mu_{FET} = (g_m L)/(WC_{ox}V_{DS})$.[100] Here g_m is the transconductance ($\partial I_{DS}/\partial V_{GS}$) at the p-type graphene side, L and W are the length and width of the graphene channel, respectively, and C_{ox} is the oxide capacitance per unit area. Using an extracted g_m value of 3.45×10^{-5} S from the I_{ds} – V_{ds} characteristic, the mobility was found to be 3,250 cm^2/Vs, which is comparable to the mobility of typical high quality graphene transferred on SiO_2. [101]

4.3 G-ISFET Chip Fabrication and Measurement Setup

4.3.1 Fabrication Process Steps

Graphene films synthesized on Cu foils (discussed in Chapter II) were used to fabricate GISFET devices following a sequence of processing steps as shown in Fig. 4.5. To begin with, the graphene was transferred on SiO_2 (300 nm)/Si (n^+ doped) substrate with the wet-transfer technique introduced in Chapter 2. To fabricate GISFETs, Ti (30 nm)/Ni (150 nm) source/drain contacts were deposited on the transferred graphene using an electron beam evaporator, with the contact areas defined by a metal mask. The graphene channel formed had dimensions of 2 x 1 mm. We used high-quality SiO_2 grown through a dry thermal oxidation process to minimize any leakage current between the metal contacts and the silicon substrate.

For stable operation in an electrolytic environment, the fabricated GISFET chip was mounted on a printed circuit board (PCB) and the source/drain ohmic contacts were wire bonded to the contact pads on the PCB. To isolate and protect the metal contacts and the bonding wires from the conducting aqueous environment, epoxy glue (Epo-tech 301) was

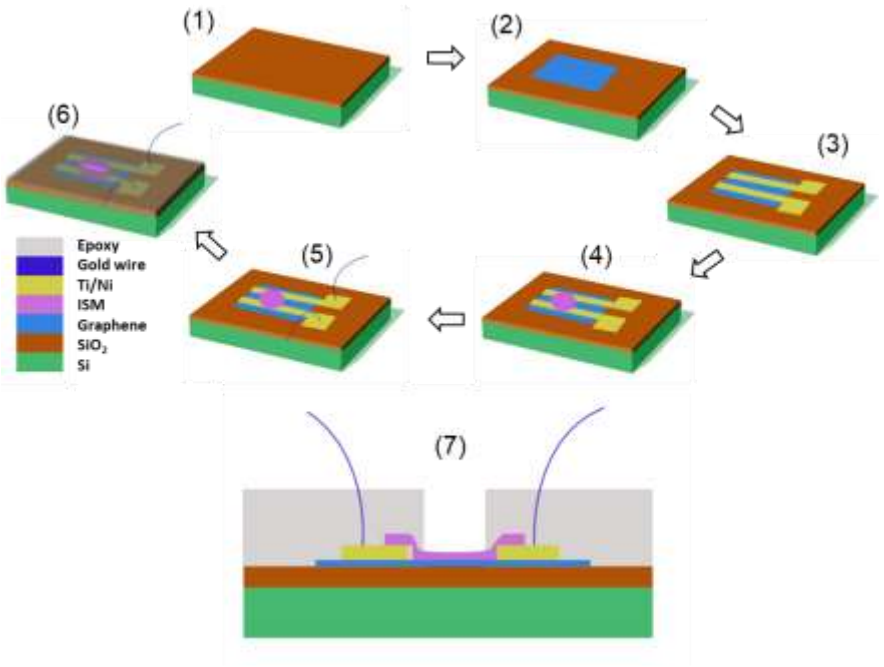

Figure 4.5 ISFET chip fabrication steps. 1. Substrate preparation. 2. Graphene transfer. 3. Source and drain formation. 4. ISM coating. 5. Mounting chip to PCB. 6. Epoxy encapsulation. 7. Schematic diagram of G-ISFET chip cross- section.

used to encapsulate them. The selected epoxy is biocompatible and specially designed for medical electronics with USP Class VI and/or ISO-10993 compliance. After careful mixing of epoxy resin and curing agent (4:1), the mixture was applied to the metal contact, SiO_2/Si chip and bonding wires, leaving a small window (2 × 1 mm in dimension) on the ISM coated graphene (see above discussion) as the active sensing area (to be in contact with the

test solution), and cured for 2 hours at 60 °C on a hot plate. Inset of Fig. 4.6 shows the optical image of a GISFET after encapsulated by epoxy.

4.3.2 Measurement Setup

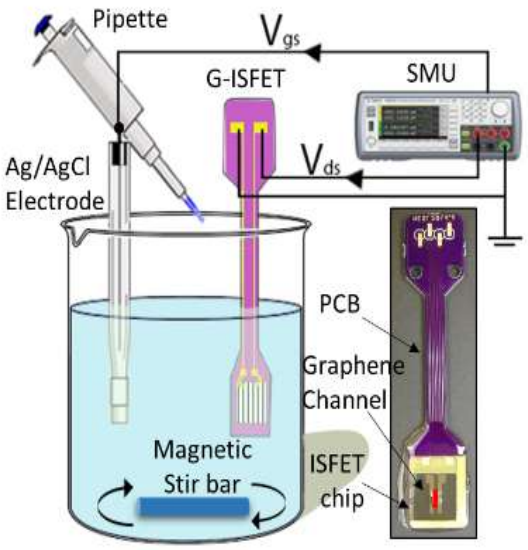

Figure 4.6 Ion concentration sensing set up. Picture of real ISFET device (right bottom) with the sensor chip mounted on PCB head.

The experimental setup for measurements in the electrolytic solution is schematically illustrated in Figure 4.6. The Ag/AgCl reference electrode was used to apply a top-gate bias for obtaining the I_{ds}-V_{tg} characteristics of the GISFET in solution. For the I-V measurement, dc bias for V_{ds} and V_{gs} were supplied by a precision source measure unit (SMU, Keysight B2902A), while simultaneously measuring I_{ds}. The device response was studied by varying the K^+ ion concentration from 1 μM to 20 mM in distilled water, in the Tris-HCl solution, as well as in 140 mM NaCl solution (imitating the Na^+ ion concentration in a typical physiological solution). Test electrolytes with desired ionic concentrations

were realized using carefully prepared stock solutions transferred using micropipettes. The measured I_{ds} - V_{tg} curves show typical V-shaped I-V characteristic underlining sharp transition from p- to n-type graphene upon application of top-gate bias.

4.4 Valinomycin-based K^+ Ion Selective Membrane

To perform selective detection of K^+ ions, valinomycin ($C_{54}H_{90}N_6O_{18}$) based ion selective membrane (ISM) with 5 µm nominal thickness was spin-coated on the entire transferred graphene area and kept at room temperature for 20 minutes for complete solvent volatilization and stable film formation. The K^+ ISM was prepared [102] by dissolving 8 mg valinomycin (VAL), 1.10 mg potassium tetrakis (4-chlorophenyl) borate (K-TCPB), 390 mg acrylic matrix copolymer (made of methyl methacrylate (MMA) and n-butyl acrylate (nBA) monomers in the proportion of 1:10) [103] in 2.0 ml of tetrahydrofuran. [104]

To ensure optimum device performance and reliability, we have developed a self-plasticized methacrylate and nBA based copolymer. This block copolymer is a two-phase system; mostly containing nBA, which consists of a continuous amorphous phase through which molecular transportation occurs rapidly, while the methacrylate block forms a discontinuous, crystalline phase that cross-links the structure. In addition, the higher molecular weight of 151,000 Da of methacrylate and nBA copolymer provide sufficient polymer chain entanglement to make the membrane more mechanically robust in harsh operating conditions, while maintaining very low predominant glass transition temperature

(-43.05 °C) that enables easy ion transportation across the membrane towards the graphene surface.[105]

Furthermore, mobile cation-exchange sites such as potassium tetrakis (4-chlorophenyl) borate [K-TCPB] has been dispersed in the polymer membrane, which reduces the membrane resistance and activation barrier for the cation-exchange reaction at the membrane/solution interface resulting in a significant reduction in ionic interfaces, thereby increasing the ion-detection sensitivity. [106-108] Taken together, the polymer membrane formulation uniquely offers all the necessary attributes for a highly sensitive, selective, reliable non-plasticized polymer membrane for biomedical and solid-state microfabrication ion sensors.

The valinomycin structure consists of alternately bound amide and ester bridges (shown as an inset of Figure 4.7). The presence of the carbonyl group, coupled with its unique doughnut-shaped structure enables valinomycin to easily bind metal ions. Due to the size of the potassium ion (1.33 Å radius), valinomycin exhibits a very high stability constant ($K = 10^6$) toward it compared to other metal ions. This results in a high degree of selectivity compare to other complexes; i.e. Na^+ with 0.95-angstrom radius forms 10,000 fold weaker valinomycin-Na^+ complexes, and thus valinomycin is 10,000 more times selective to K^+. [108] While the K^+ by itself is able to cross single lipid bilayer, it has been shown that the presence of valinomycin in the lipid layers makes it freely permeable through multiple lipid bilayers.[109] This property was utilized in our design of the ion selective layer to make it specifically permeable to K^+ ions. Figure 4.7 shows a schematic summarizing the operation of the ion-selective membrane. Another important advantage

of using valinomycin is that it can act as a functionalization layer on the graphene surface of the ISFET enhancing its sensitivity. Since pristine graphene is chemically inert,[79] many research groups have adopted different kinds of oxide layers (SiO_2, HfO_2[110],

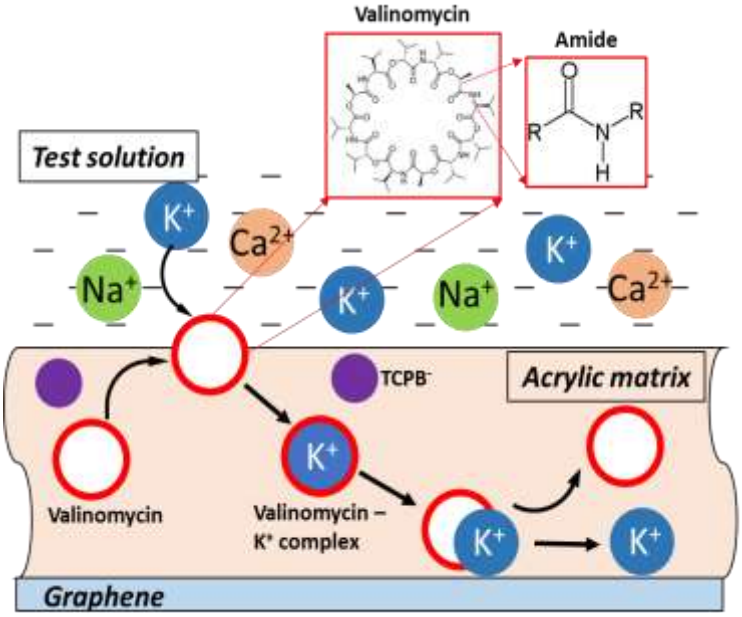

Figure 4.7 Schematic illustration for K^+ ion diffuse through K^+ ion selective membrane.

Ta_2O_5[111]) as well as aromatic molecules as a functionalization layer on top of the graphene surface to enhance its ion sensing capabilities. The valinomycin layer coated on the graphene surface can enhance the ISFET sensitivity, similar to other aromatic molecule functionalization. [112-113]

4.5 G-ISFET Ion Sensing Performance

4.5.1 Sensing of K^+ Ionic Concentration in Distilled Water

After fabrication of the GISFET, we performed detailed electrical characterization and investigated the K^+ sensitivity of the GISFET in a distilled water based K^+ ion solution. The variation in drain current with top gate voltage ($I_{ds} – V_{tg}$ characteristics) was measured using a standard Ag/AgCl reference electrode (where the gate voltage was applied), in a test electrolyte solution of variable KCl concentration, and the results are plotted in Figure 4.8. The Dirac point in the $I_{ds} – V_{tg}$ plots can be seen to vary from 0.2 – 0.7 V, which is a dramatic reduction compared to the Dirac point of ~41.6 V measured for the same FET in the air prior to valinomycin coating (please refer to Figure 4.4 (a)). This large change in Dirac point can be attributed primarily to the strong electron donating nature of the valinomycin molecule which possesses 6 amides ($RnE(O)xNR'_2$) functional groups. Indeed, separate experiments conducted on back gated FETs in ambient conditions indicate that a large Dirac point shift, by 20 – 30 V, can be caused by valinomycin coating, which donates electrons to p-type graphene to shift the Dirac point closer to 0 V. Another important point to note here is that the high capacitance of the electrical double layer (EDL), formed at the interface of graphene and the electrolytic solution,[114] enables the ISFET device to operate at a much narrower voltage range (i.e. charge density and Fermi level changes much more rapidly with applied top gate voltage; g_m change from ~10^{-5} S for back-gate FET to ~10^{-4} S for top-gate FET), which offers a significant advantage for practical sensor design. Indeed, the capacitance for a back-gated FET can change by orders of magnitude from nF/cm^2 range in the air (closely matching our extracted capacitance of

11.5 nF/cm^2) to μF/cm^2 range in the electrolytic environment as shown by Ye et al.[114] From Fig. 4.8 we also observe that the Dirac point shifts very significantly, from 0.57 V to 0.29 V, as the K^+ concentration increases from 1 μM to 20 mM. Such a movement of the Dirac point to lower values is expected since the K^+ ions near or at the graphene surface induces higher electron concentration (i.e. reduces hole concentration in p-type graphene), thereby moving the Fermi level closer to the charge neutrality point, and consequently lowering the Dirac point. Such a lowering of Dirac point due to adsorption of positively charged ions is also observed commonly for H^+ ions in a pH ISFET.[112][115]

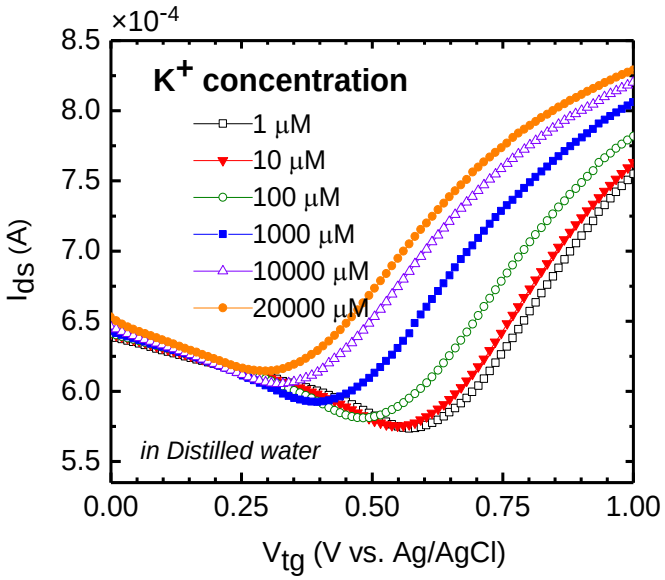

Figure 4.8 K^+ sensing in distilled water based electrolyte solution. Dirac points can be seen to shift very significantly as the K^+ concentration increases from 1 μM to 20 mM.

Since sensitivity and response time are two critical parameters for any sensor, we carefully examined these parameters for our graphene ISFETs. A commonly used method to determine the sensitivity of ISFETs (i.e. commercial Si ISFETs) is to look at the shift in

threshold voltage (equivalent to the shift in Dirac point of the ISFET) as a function of the change in K^+ ion concentration.[116] The change in Dirac point as the K^+ ion concentration

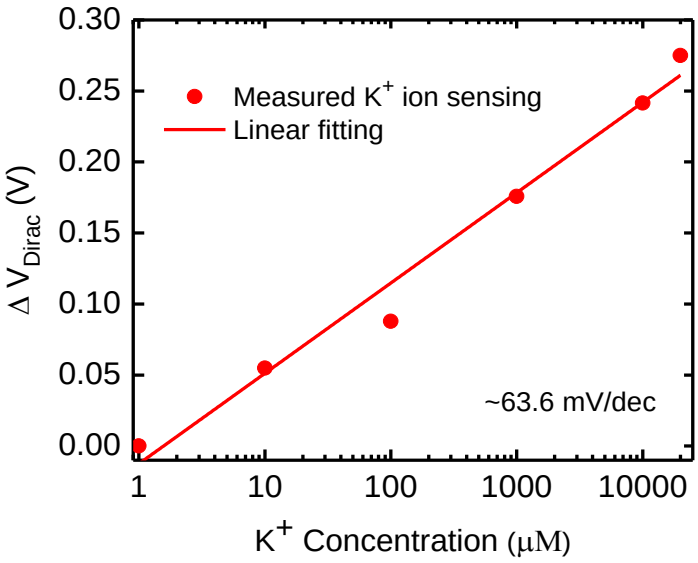

Figure 4.9 Dirac point shift varies with K^+ concentration change fairly linearly, showing an average sensitivity of ~64 mV/dec for the least square fit.

was varied from 1 μM to 20 mM (this includes the range of interest for cellular efflux of 10 μM – 1 mM [117]) can be determined from Fig. 4.9 to be ~280 mV, and hence the sensitivity can be calculated as 64 mV/decade (= 280 mV/4.3 decade), which is very comparable to that obtained from the Si-based ISFET devices. [118]

Another method (commonly used for chemical sensors) to determine the sensitivity and the response time is to determine the magnitude and temporal variation of the ISFET drain current as the K^+ ion concentration is changed in steps. To this end, we recorded the I_{ds} as a function of time for various K^+ concentrations (for a fixed value of V_{tg}) using a data acquisition unit (DAQ, Keysight 34972A); and the results are shown in Fig. 4.10. A plot

of the concentration change from 100 µM to 1 mM (corresponding to typical cellular efflux) is shown in the inset of Fig. 4.10 to calculate the response time and current change based sensitivity (ΔI/I, similar to the sensitivity calculated for chemical sensors). As can

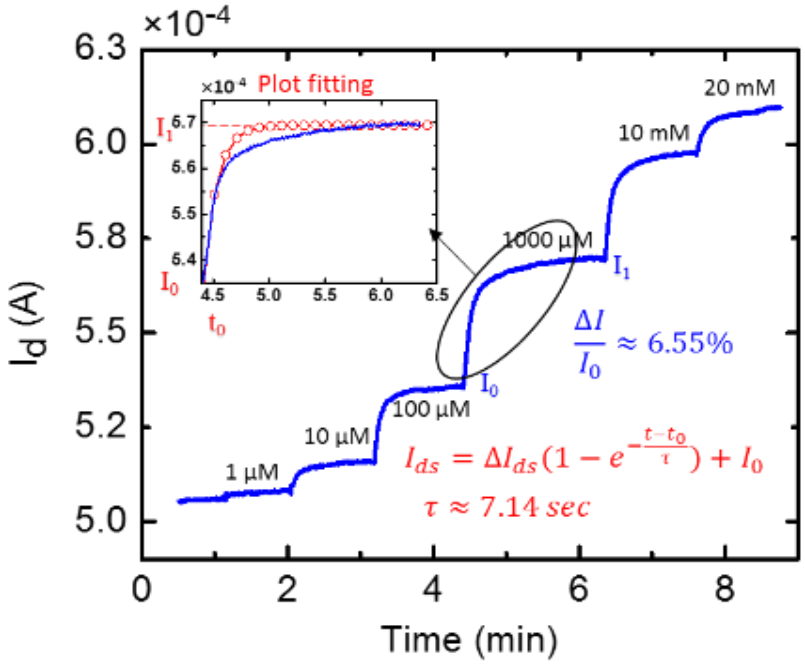

Figure 4.10 Current change response as the by K^+ concentration was changed in steps from distilled water to 20 mM. Fractional change in current used to calculate sensitivity and time constant for sensing response are calculated from exponential fits to the response transients corresponding to each concentration change.

be seen, the current changes from 528 to 563 to µA, corresponding to a fractional change in the current of ~6.6 % per decade change in K^+ ion concentration. Fitting the time-dependent response plot with an exponential function, a time constant of $\tau \approx 7.1$ seconds can be extracted, which is very close to the best values of ~5 seconds observed for commercial pH sensors (Topac, S1600 Advanced pH meter).

4.5.2 Ion Selectivity of GISFETs

Although graphene-based ISFETs have been extensively studied for pH sensing or Na^+ sensing [110][119] by many research groups, the ion-selectivity aspect is generally not investigated in detail, although it is one of the most important characteristics of any sensor. In this research, we have made the ISFETs selective to K^+ ions by coating them with valinomycin based ISM. Details of the mechanism and preparation for the ISM coating have been discussed in section 4.4. In a device structure, when the device is interfacing with an electrolyte solution, valinomycin in ISM selectively traps only K^+ ion from the solution, forming a valinomycin-K^+ complex, which can further transit to the vicinity of graphene surface (as illustrated in Fig. 4.7). The electrical field exerted from the captured K^+ ions affects the conductivity of the graphene channel and thus induces an electrical sensing signal. The ion selectivity of the sensor was studied by comparing the responses of the ISFET to common background ions Ca^{2+} and Na^+ vis-a-vis the K^+ ions. Figure 4.11 presents the responses to Na^+ and Ca^{2+} ions over the range of 1 µM – 1 mM. We found that even though the concentration of these ions changed by 3 orders of magnitude the Dirac point did not shift, clearly highlighting the high selectivity of our ISFET with respect to these interfering ions. In contrast, a large response was observed for K^+ ions in distilled water based solution and also in presence of high interfering ionic concentration (i.e. 140

mM Na^+) as already discussed in detail above. This clearly underlines the high selectivity of the proposed ISFET sensor.

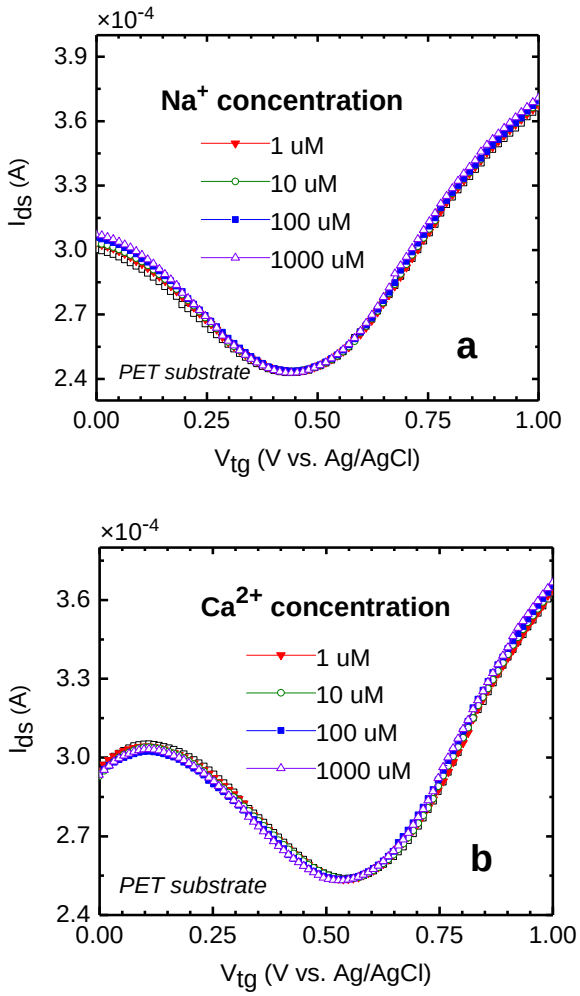

Figure 4.11 The GISFET with Valinomycin polymer matrix coating is effectively insensitive to Na^+ ions (a) or Ca^{2+} ions (b) over the concentration range of 1 ~ 1000 µM NaCl or $CaCl_2$ (measurement performed in distilled water-based solution), as can be inferred from the overlapping I-V plots.

4.5.3 Repeatability and Reliability of The GISFET Device

For robust ion sensing applications, the ionic concentration measurements by the ISFET need to be reliable and repeatable. To study this, the performance of a GISFET was

recorded over a period of two months by periodically measuring its sensitivity to K^+ ion concentration. The results are shown in Fig. 4.12, which shows an average sensitivity of 61 mV/dec over a course of two months with a standard deviation of 4.6 mV/dec. It should

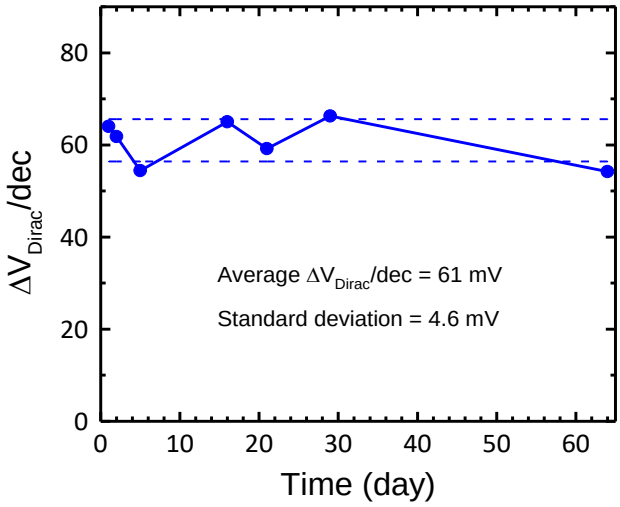

Figure 4.12 Sensitivity of the GISFET sensor measured over a duration of two months shows a stable response with an average sensitivity of 61 mV/dec and a standard deviation of 4.6 mV/dec.

be noted that the sensitivity of the device exhibits a range bound fluctuation over the course of the month instead of exhibiting any monotonically varying trend, which rules out steady degradation of the ISFET device over time, unlike widely observed for its Si counterparts. The cause for such small fluctuations are still under investigation but likely contributed by randomly varying experimental and environmental factors. For a given measurement the ionic concentration was measured at least 3 times by the ISFET sensor, which was found to be highly repeatable, with only 1% deviation from the mean sensitivity value.

4.6 G-ISFET on Flexible Substrate

Fabrication of ISFETs on flexible substrates is highly attractive for implantable biosensing applications. Unlike Si-based ISFETs, graphene is inherently compatible with flexible substrates due to its own flexible nature and easy transfer process of CVD graphene to various substrates without undergoing any cumbersome fabrication process. Polyethylene terephthalate (PET) is a material widely used for numerous applications

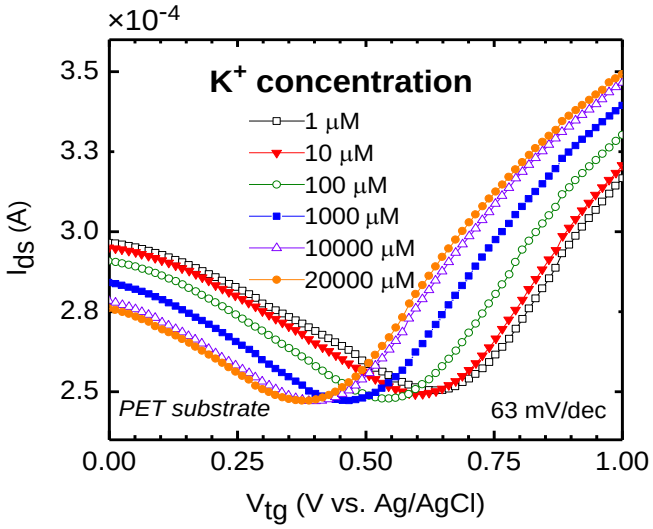

Figure 4.13 GISFET fabricated on flexible substrate PET shows an average K^+ ion sensitivity of ~63 mV/dec over the concentration range of 1 μM to 20 mM.

involving our daily life (i.e. in bottles, packaging materials, etc.) due to its extremely low toxicity and low cost. It is also a material of choice for technical applications (i.e. automotive and electronics) owing to its excellent dielectric strength and chemical inertness.[120] In this work, therefore, investigated the feasibility of fabricating high-performance graphene-based ISFETs on PET substrate. The fabrication steps and materials

used are very similar to the GISFET on SiO_2/Si substrate, except the substrate itself is replaced with PET. The performance of GISFET on PET was determined in the same way as discussed above, and the result is shown in Fig. 4.13. We find the K^+ ion sensitivity to be ~63 mV/dec (= 272 mV/4.3 decade), which is essentially unchanged compared to that measured for Si/SiO_2 substrate (~64 mV/dec). The selectivity of the graphene ISFET on

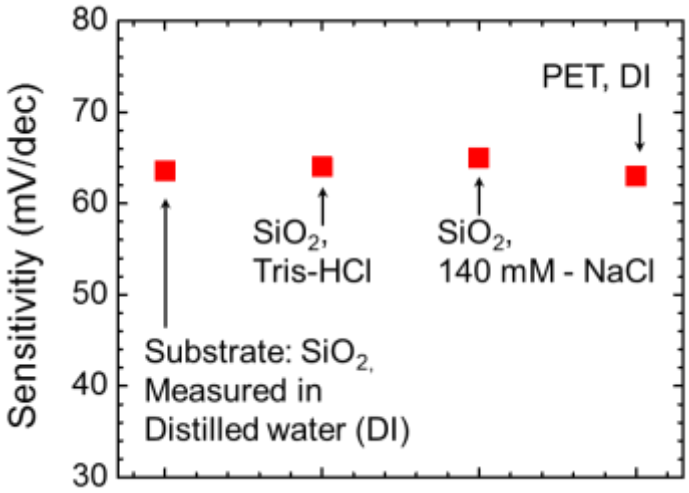

Figure 4.14 GISFET's stable sensitivity in different solution bases or fabricated on different substrates.

PET, with respect to Ca^{2+} and Na^+ ions, also turns out to be very similar to that observed for the ISFET on SiO_2/Si substrate. Both the selectivity and sensitivity results clearly indicate the strong promise of PET substrate for realizing high-performance graphene ISFETs for implantable biosensing applications. The stable performance of GISFETs in different solution or fabricated on different substrates are shown in Fig. 4.14.

In conclusion, this chapter has demonstrated a novel ISFET device capable of performing highly sensitive and selective detection of K^+ ions in various media over a wide

ionic concentration range of 1 μM – 20 mM. The sensitivity exhibited by the sensor of 61 ± 4.6 mV/decade over a duration of two months is very comparable to the best Si-based ISFETs available commercially, while the sensor response to interfering Na^+ and Ca^{2+} ions were found to be negligible. The sensor performance also did not change significantly with repeated testing over a period of one month highlighting its robustness and reliability. When fabricated on a PET substrate, the sensor very similar performance, which is highly encouraging for developing flexible bio-implantable graphene-based ISFETs.

CHAPTER FIVE

G-ISFET FOR IMPLANTABLE BIO-SENSING APPLICATION

Elevations in biological levels of K^+ ions precede the onset of sudden cardiac death, epileptic seizures, and other clinical problems. [121-122] However, the time course and magnitude of these changes in extracellular K^+ ions is yet unknown. Therefore, the development of implantable K^+-sensitive sensor devices could be of great use in predicting the onset of myocardial infarctions and seizures. In addition, ISFETs present a non-invasive and bio-compatible technology for measuring K^+ efflux from primary and stem-cell derived cells that are used for toxicological and drug discovery testing.

Si-based ISFETs are already commercially available, although they suffer from several drawbacks. One of the major challenges with the Si-based ISFETs is that ions (i.e. H^+, OH^-) typically migrate into the oxide (accumulating at the SiO_2/Si interface) and change the threshold voltage of the FET,[123-124] leading to their degradation over time with repeated usage. Graphene offers an excellent opportunity to address this limitation of Si-based sensors offering a surface that is impervious to ions. Even more significantly, graphene synthesized by chemical vapor deposition (CVD) on Cu foil can be transferred to various substrates of choice (other than SiO_2/Si), which helps to avoid this issue of ion accumulation and associated device degradation completely (demonstrated in this work by realizing graphene ISFET on PET substrate).

5.1 G-ISFET Performance in Tris–HCl Solution and High Na^+ Concentration Background

To determine the applicability of the GISFETs for K^+ ion measurements in physiological solution, its performance was investigated in a 0.1 M tris-HCl solution with pH 7.4 (from VWR), which is commonly used in buffer solutions for biochemistry and molecular biology experiments (i.e. Protein Electrophoresis, Western Blotting and Nucleic Acid Agarose Electrophoresis [125]). The results for K^+ ion sensing are illustrated in Fig. 4.9 where the Dirac point is found to shift by 0.275 V for a 4.3-decade change in K^+ concentration, exhibiting a sensitivity of 64 mV/decade, which is exactly the same as that obtained for K^+ concentration variation in distilled water discussed above.

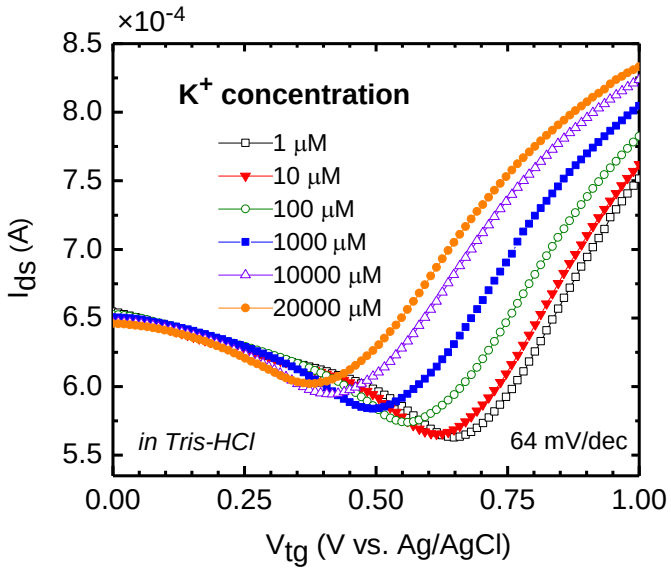

Figure 5.1 K^+ sensing in 0.1 M Tris-HCl solution (pH 7.4). The result shows good sensitivity exhibiting similar value as obtained from distilled water based solution.

To further test the suitability of our sensor for usage in physiological solution, where typically very high (~150 mM) background concentration of Na^+ is present, we

tested the performance of the device in concentrated NaCl solution (140 mM). The sensitivity is found to be 65 mV/decade in the sensing range of 10 μM - 20 mM, showing very similar sensitivity to the distilled water based solution. Below 10 μM, reliable sensing of the K^+ ion variation was found to be difficult as the high Na^+ concentration increased the K^+ ion sensing baseline (this is actually expected based on the expected selectivity of 10,000 for K^+ ions relative to Na^+ ions as discussed above). Nonetheless, the operational range of the sensor completely covers the concentration range of interest for cellular efflux measurements of 100 μM to 1 mM (see discussion above).

5.2 GISFET Array Fabrication Using CMOS Compatible Technique

The G-ISFETs fabrication process demonstrated in the previous chapter had used a shadow mask for source/drain patterning, also a manual application of epoxy had carried out for encapsulation. With these process techniques, the fabricated devices showed very good sensing performance. However, the process consumes much bigger size of graphene compared to the size actually used in the device operation and it is unsuitable for fabrication in large numbers or in arrays. In this section, a new G-ISFET fabrication process flow will be demonstrated which is compatible with regular photolithographic processes, and a designed 5 × 5 micro G-ISFET array can lead it to advanced applications in simultaneous multi-well and multi-functional testing.

The fabrication steps include (1) graphene transferring, (2) graphene patterning, (3) source/drain electrode patterning using metal lift-off technique (4) SU-8 encapsulation layer patterning, (5) ISM coating, (6) and lastly wire-bonding electrodes on a chip carrier.

Three photo-mask designs used in the fabrication (Figure 5.2) are drawn in three different colors with their names marked as Metal, Graphene, and Encapsulation, which will be used in the patterning step (2), (3) and (4), respectively. The design includes 25 micro-GISFETs

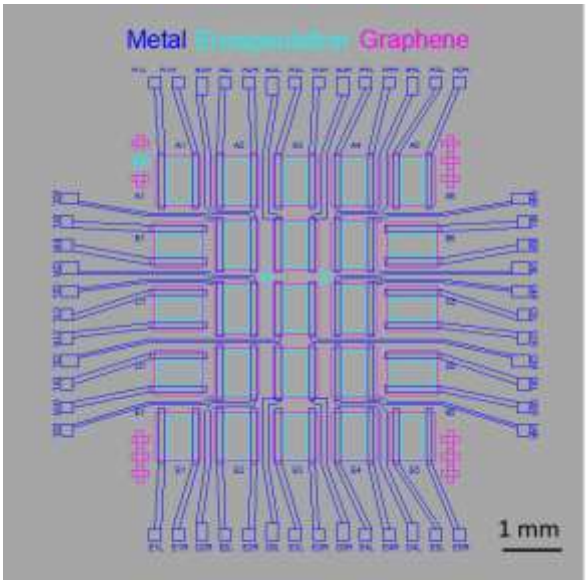

Figure 5.2 G-ISFET array photo-mask design (overlapped). The three mask layers are graphene patterning, electrode patterning, and encapsulation layer patterning.

in a 5 × 5 array with 375 × 750 μm active graphene sensing window on each device. Also, 50 electrode pads are arranged in lines at 4 sides for the later chip packaging process.

Figure 5.3 shows optical microscope images taken after each major process step. For graphene patterning, a large area graphene film (8 × 8 mm) was transferred first on Si/SiO_2 substrate using the technique that has been introduced in Chapter 2. Then, photoresist (PR) AZ-701(MicroChemicals GmbH) was used for photolithography with spin coated protection layer LOR 3A (MicroChemicals GmbH) on the graphene. Without this protective layer, the graphene can be easily peeled off or contaminated by photoresist

during the patterning process. Oxygen plasma (PE25-JW, Plasma Etch, Inc) with power of 75 W was exposed for 3 min to etch away graphene after PR formed pattern on it. The patterned graphene can be seen in Figure 5.3 (a).

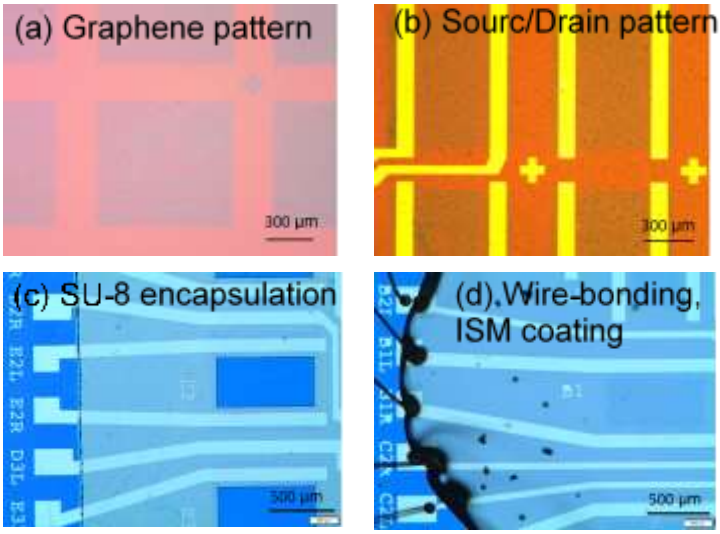

Figure 5.3 G-ISFET array fabrication steps. (a) Graphene patterning, (b) Source/drain electrode patterning, (c) SU-8 encapsulation, defining active sensing area, (d) ISM coating and wire bonding on chip carrier.

Step (3) metal lift-off patterning was processed using photoresist NR71-3000P (Futurrex, Inc.) and again the LOR 3A protective layer. Ti/Ni (30/150 nm) metal stack was deposited using an E-beam evaporator system on top of patterned PR. After metal layer lift-off process using solvent and developer AZ 300MI (to remove LOR 3A), a patterned electrode on the graphene can be obtained (Figure 5.3(b)). Then, an epoxy-based PR SU-8 was used to encapsulate the chip by photolithography process only leaving active graphene sensing window open (Figure 5.3(c)). Lastly, ion selective membrane is coated and the chip was wire-bonded on a chip carrier (CSB04840, Spectrum Semiconductor Materials, Inc.) as shown in Figure 5.3(d).

A reservoir to fill analyte solution while sensor testing was produced using a 3D printer, and attached on top of the chip carrier with epoxy glue. The top view and side view of them and the optical image of the fabricated chip are shown in Figure 5.4. A precision

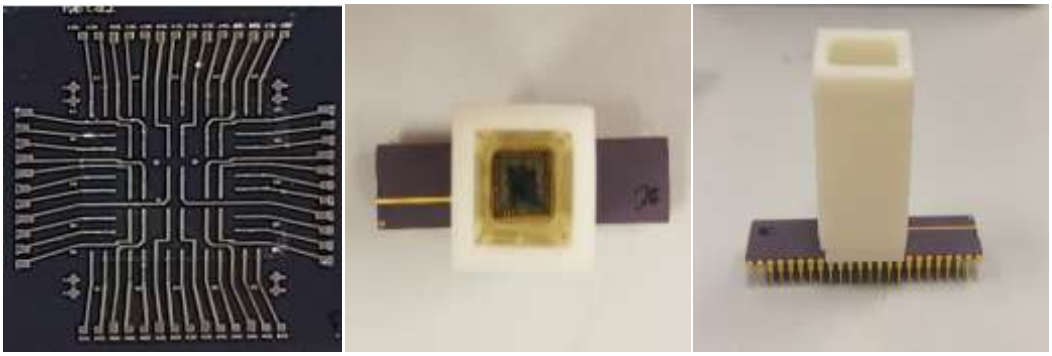

(a) (b) (c)

Figure 5.4 (a) G-ISFET array chip. (b) Top view and (c) side view of chip packaged on the chip carrier with a 3D printed solution reservoir.

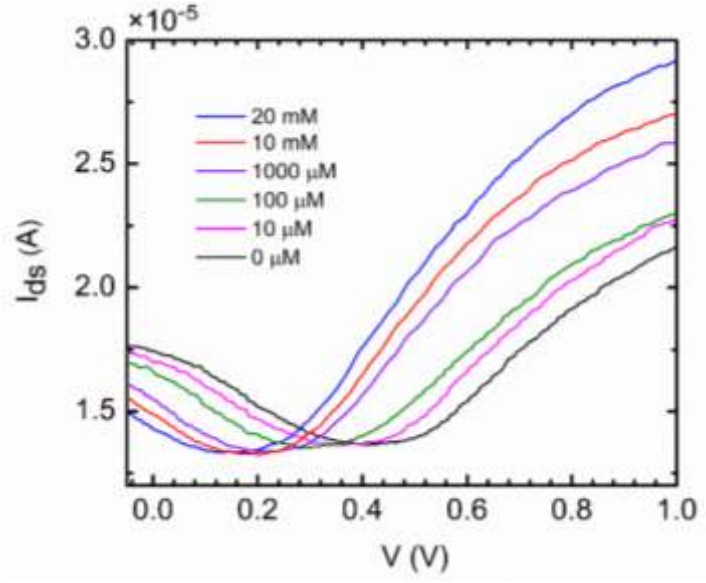

Figure 5.5 K^+ ion sensing performance of the fabricated ISFET-array device. Large variation in Dirac point is observed by ~260 mV with 4.3 orders of magnitude change in K^+ concentration.

source/measurement unit was used to characterize the device and record the sensing performance. An Ag/AgCl reference electrode was used to apply constant voltage to the solution and measure the current. The performance of the fabricated ISFET is shown in Figure 5.5. We find that the Dirac point shifted 270 mV corresponding to K^+ ion concentration change from 1 μM to 20 mM (4.3 orders of magnitude). The sensitivity is calculated to be ~62.8 mV/decade which is similar to the value (average ~63 mV/decade) of earlier G-ISFET devices fabricated individually without using CMOS fabrication technique. These results are indeed promising and pave the way for the realization of the larger arrays of graphene based GISFET devices for simultaneous multi-well testing.

5.3 GISFET Performance Evaluation with Cellular Efflux of Living Cell

Cell-based ion efflux assay is essential in biomedical research and drug discovery processes by providing the primary insight into ion channels' activities of cell membranes that responded to external stimulation. As a result, a large number of cell-based assay to screen ion channels are demanded in the laboratory. The patch-clamp technique has been considered as a "gold standard" method to investigate ion channel activity due to its direct, real-time measurement advantages. However, its complex handling procedure and low-throughput are practically not applicable in large amounts of screening process which has introduced in Chapter 4. Thus, various measurement techniques have been developed. Among those techniques, ion sensitive field effect transistor (ISFET) -based ion flux assay is one of the most popular ones because of its fast and simple electrical signal measurement.

Compared to other techniques such as binding assays [126] and fluorescent dyes assisted assays [127], ISFET doesn't need any additional scintillation assist or require huge imaging artifacts as they carry out ion channel activity measurement indirectly by analyzing images. Also, the device mass production capability by traditional CMOS fabrication process made ISFET a more attractive technique for multi-well and multi-functional assay in the future. However, the commercial Si-based ISFETs that are available in the market have a significant reliability issue with a very short lifetime (1~2 months). This is due to unintended ion penetration into the SiO_2/Si stack interface during sensor operation in the aqueous measurement environment, which consequently causes an irrecoverable sensing performance degradation (consider detailed discussion in Chapter 4). To solve the problem, this section demonstrated the feasibility of using GISFETs for ion efflux measurement, which is a direct measurement involving living cells. The cells observed in the study are U251 MG human glioma cells cultured in a pharmacological lab in Universtiy of South Carolina (Dr. Walsh). A chemical of A23187 is used to activate cells' NSC channels. The activation will induce potassium ion (K^+) efflux from cells and therefore increase the extracellular K^+ concentration in the buffer solution.

To characterize GISFET's sensing performance to live cells ion efflux, a measurement setup has been designed and assembled as Figure 5.6. In a 3 mL well, a specially casted PDMS mold has been placed to provide a space for cell-coated glass coverslip at the bottom of well and a notch where the GISFET device and a reference electrode can be inserted. Thus, through the notch, the GISFET sensing head and a reference electrode can be dipped in the buffer solution to where the cell is immersed. An

Ag/AgCl reference electrode was used to apply constant voltage to the solution during measurement using the same SMU.

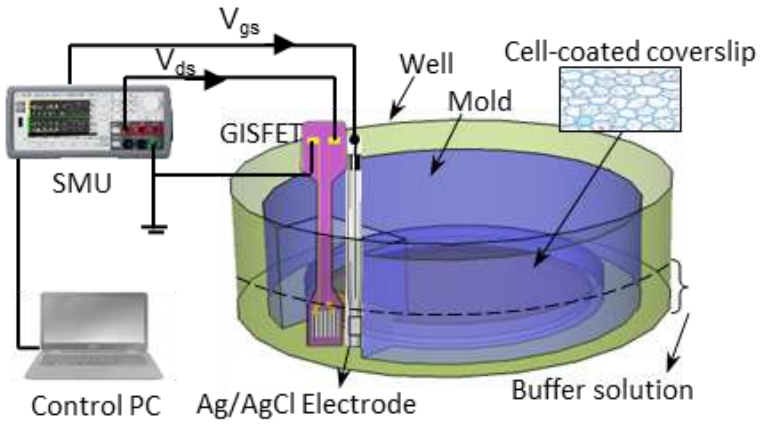

Figure 5.6 Schematic diagram of Graphene ISFET cell efflux measurement setup.

To characterize the G-ISFET sensor in a mimicked environment first prior to the live-cell assay, a 50 μM K^+ ion detecting test was carried out in the same measurement setup (shown in Figure 5.6) with the same background solution that will be used later. The background buffer solution consists of 140 mM NaCl, 1 mM $CaCl_2$ and 1 mM $MgCl_2$ was filled in the well, and a K^+ ion stock solution was prepared for the test. The measurement result is shown in Figure 5.7. From the plot, after ~1 min of stabilization time prepared K^+ stock solution was dropped into the buffer solution increasing the K^+ concentration to 50 μM. In less than 1 min, we observed a stabilized 20.9 uA increase in drain current.

A chemical of A23187 can activate cell's NSC channels which will induce K^+ efflux and therefore increase the extracellular K^+ concentration in the buffer solution. To test GISFET's ion sensing directly on live cells, a glass coverslip (25 mm diameter) with

cells plated on top side was placed at the bottom of the well in measurement setup (consider Figure 5.6). Then, the well is filled with 3 mL of buffer solution and the G-ISFET sensor and reference electrode were dipped in the solution. After ~2 min of stabilizing time, A23187 was dropped into the well to stimulate the cells, which resulted in a rise in current as shown in Figure 5.8. The data logger kept recorking the following ~20 min. After 20

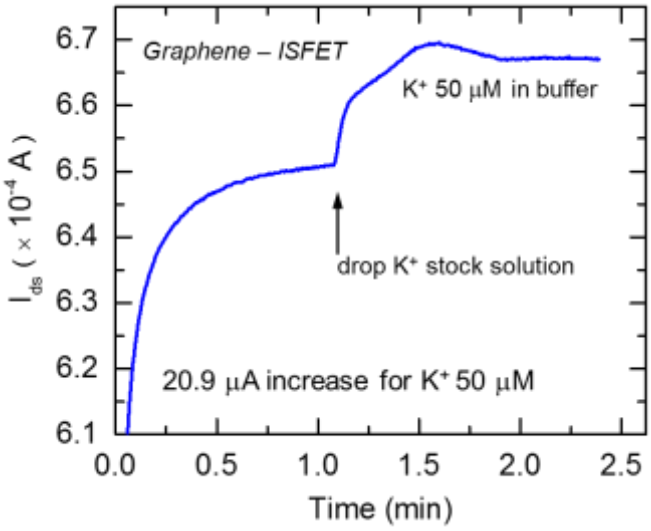

Figure 5.7 G-ISFET's response to 50 μM K^+ ion sensing in physiological buffer solution.

min, we observed the current increased ~26 μA since when A23187 dropped in the solution. Compared to the control plot and the one in Figure 5.8, we concluded that the simulate caused a ~50 uM K^+ concentration increase in the buffer solution due to the cell's efflux of K^+ ions. The result is comparable to a test conducted by Walsh et al. in a previous report (Walsh KB, etc. Biosensors and Bioelectronics. 2014 54, 448.) where they used a commercial Si-ISFET sensor instead of GISFET.

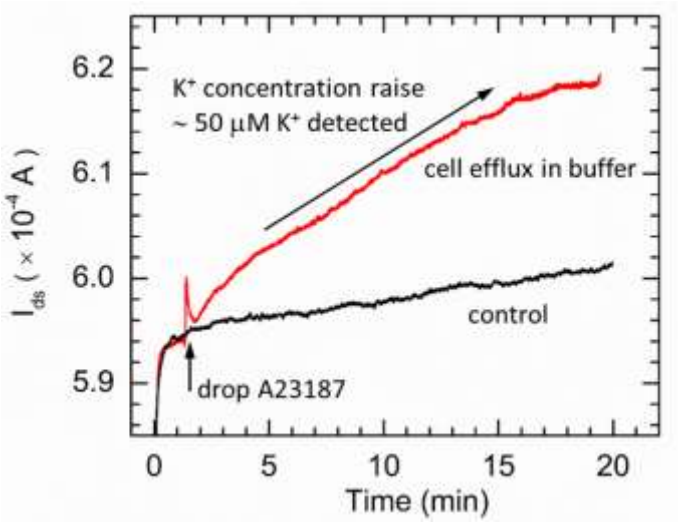

Figure 5.8 G-ISFET and Si-ISFET comparison of detecting K^+ ion concentration of cell efflux response, inset is optical microscope image of the cell.

This section successfully demonstrated a direct testing on live cells using GISFETs by measuring ion concentration change of extracellular solution. Which confirms GISFETs bio-compatible sensing possibility and its potential for advanced applications in bio-technology in the future such as multi-well, multi-functional bio assay.

5.4 Fabrication and Sensing Performance of G-ISDiode

There is a large number of ion sensors have been developed for wide range of ion sensing applications, e.g. water quality monitoring, food and beverage condition monitoring and wastewater treatment. While most of the sensors operate with a linear sensing relationship with analyte (its amount or the concentration) by shifting threshold voltage (Si-based MOS) or potential drift (ISE), in a certain application it requires an especially high and accurate sensitivity at the desired concentration range. [1-4] As

mentioned in the last chapter, cell efflux monitoring is becoming more and more important in biological and pharmaceutical research. In the investigation of cells response excited by chemicals or drugs needs high accuracy in which the ion concentration also normally shifts in a relatively narrow range. Graphene is a perfect material for using as a sensor due to its high surface to volume ratio, high carrier mobility and unsaturated sp^2 bonds at the surface. With such extraordinary advantages, many research groups have investigated graphene's potential as ion sensors, though none of them proposed Schottky junction based ion sensing devices so far [7-8]. This section will demonstrate an ultra-high sensitivity in the range of 10 uM – 10 mM for potassium ions or sodium ions with graphene/silicon Schottky diode structure.

5.4.1 Graphene/Silicon Schottky Diode

Prior to the investigation of G-ISDiode, a simple graphene/silicon Schottky diode structure will be introduced briefly including its structure, fabrication, and electrical characteristic. In graphene-based FET sensors or chemiresistor sensors, the carrier transport in the devices follows the simple Ohm's law with conductivity equation $\sigma = q \cdot \mu \cdot n$, where q is electronic charge, μ is carrier mobility, and n is carrier concentration. Therefore, the resistivity or conductivity change caused by interactions between graphene and outside molecules is linearly proportional to interacted gas/ion concentration. Which are usually expressed in relations such as $\Delta\sigma \sim \Delta n$, $\Delta\sigma \sim \Delta\mu$, or $\Delta V_{Dirac} \sim \Delta n$. However, in graphene to silicon Schottky diode, the carrier transport across the junction is following an exponential relation. The diode equation governed by thermionic emission model is [128]:

$$I = I_s \left[\exp\left(\frac{qV}{\eta kT} - 1\right)\right] \tag{5.1}$$

where I is junction current, I_s is the reverse saturation current, q is the electronic charge, k is the Boltzmann constant, η is the diode ideality factor, T is the temperature, and V is the applied voltage to the diode. While I_s is defined as:

$$I_s = AA^*T^2\exp(-\frac{\Phi_B}{kT}) \tag{5.2}$$

where A is the contact area, A* is the effective Richardson Constant, and Φ_B is the Schottky barrier height (SBH). SBH is determined by the difference of graphene Fermi level and semiconductor electron affinity. So, in sensing application, we can obtain an exponential

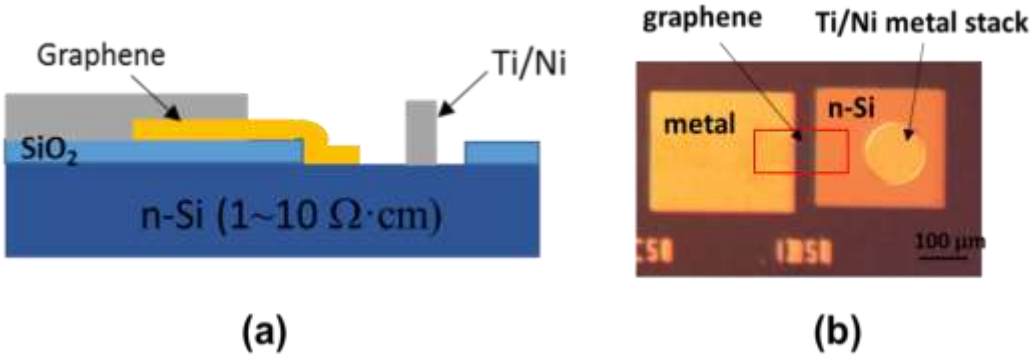

Figure 5.9 (a) Graphene/Silicon diode structure, (b) Optical image of fabricated graphene/silicon Schottky diode.

change in graphene/semiconductor junction current as a result of analytical interaction caused graphene's Fermi level shift.

Graphene/Si Schottky diode is fabricated on n-Si/SiO_2 substrate where silicon is a low doped one showing resistivity of 1-10 Ω·cm. SiO_2 patterning is performed using photolithography and HF wet etching of SiO_2. Then, graphene is transferred and patterned

using previously introduced wet-transferring technique (discussed in Chapter 2) and patterning process(discussed in Chapter 5), respectively to form a graphene/silicon junction (area of 150 × 150 μm) with the silicon substrate. Lastly, Ti/Ni metal stack is evaporated and patterned following lift-off process steps forming Ohmic contact individually on graphene and on silicon. The schematic of the diode cross section and a microscope image of a completed diode device is shown in Figure 5.9 (a), (b).

A representative I-V characteristic of the fabricated graphene/n-Si Schottky diode is shown in Figure 5.10. From the half logarithmic I-V plot, the Schottky junction shows a

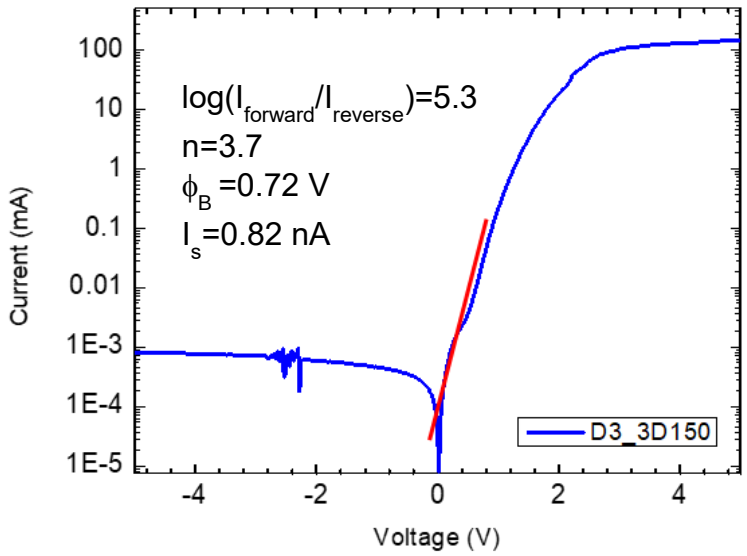

Figure 5.10 I-V characteristic of graphene/Silicon Schottky diode.

good current rectifying property with the ratio of forward to reverse current over 5. The saturation current I_s is less than 1 nA, and using equations 5.1 and 5.2, we find $\eta = 3.7$, and $\Phi_B = 0.7$ eV, which are in close agreement with earlier reports. [129-130]

5.4.2 G-ISDiode Fabrication

Most steps of the G-ISDiode fabrication process are the same as those steps have discussed in graphene/silicon diode fabrication except the encapsulation step. An n-type 1~10 ohm·cm n-Si substrate with 300 nm SiO_2 layer grown on top of it was prepared. Two 800 μm wide SiO_2 lines were patterned exposing bare Si surface by the photo-lithographical method. CVD grown graphene was chemically released from copper foil and transferred onto the SiO_2/Si substrate covering both Si and SiO_2 surface area. The transferred graphene normally attaches on both Si and SiO_2 surfaces quite firmly, it doesn't detach or peel off easily unless we scratch it away. Two Ti/Ni (30/150 nm) metal stacks were evaporated on the graphene and on the Si individually forming ohmic contacts as shown in Figure 5.11. After the chip fabrication is completed, the chip was mounted on a

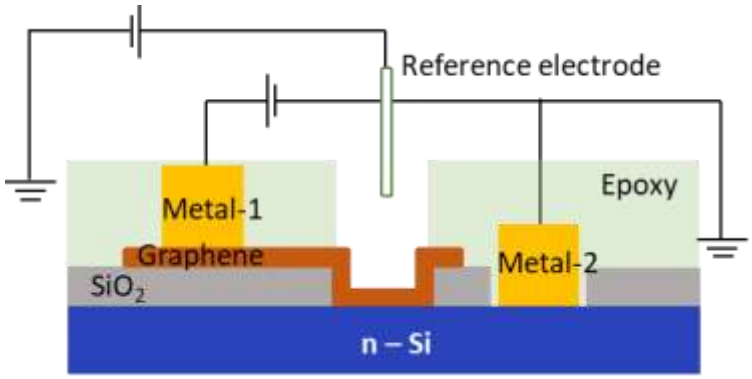

Figure 5.11 Schematic diagram of the G-ISDiode chip structure. Metal-1 forms Ohmic contact with graphene while Metal-2 is for silicon.

printed circuit board (PCB) and the Ti/Ni metal stacks (both on graphene and Si) were wire bonded to two electrodes of the PCB, respectively. As the devices will work in an aqueous

environment, all of the chip surface area and wired contact bondings were encapsulated with epoxy resin except a 2.5 mm long graphene/Si junction area as active sensing window. Figure 5.11 shows the device structure and circuit we used for characterization. To apply a constant voltage to the solution and measure the gate current, an Ag/AgCl reference electrode was dipped in the analytic solution to apply a constant bias. A beaker of DI water was used as the base solution, while a range of 1 μM – 10,000 μM ionic concentration were obtained by adding ion stock solution into the beaker with micro-pipette. All the solutions were kept in the same temperature environment to make sure the device performance was not affected by temperature variation.

5.4.3 Sensing Performance of G-ISDiode

When a reverse bias is applied to the Schottky junction, the fermi level of graphene rises as its charge density changes. [131] While positive metal ions present at the graphene surface, the graphene Fermi level will shift even higher by the bias caused by ion concentration, as a result, the Schottky barrier height (Φ_B) reduces accordingly. Thus the junction current will increase exponentially due to Equation 5.1 and 5.2 giving rise to ultra-high sensitivity.[23]

The fabricated G-ISDiode's ion sensing performance is measured by applying graphene (Metal-1) a bias of -2 V in a step function, applying the solution constant voltage of 0 V. The gate current is recorded by the time while the potassium concentration of the solution was increased from 1 uM to 10 mM. Figure 5.12 shows the result of the measurement. In plot (a), the current increased 1.2%, 11%, 58%, 590%, 3,706% at the basis of current got in deionized water (DI) when the potassium ion concentration shifted to 1

μM, 10 μM, 100 μM, 1,000 μM and 10,000 μM respectively (the inset is the curve plotted in an adjusted scale to show current change with the ion concentration up to 100 μM). The current vs. ion concentration is plotted in full log scale in Figure 5.12 (b). From the plot, a better exponential increase at the higher ion concentration range is found, while at the lower

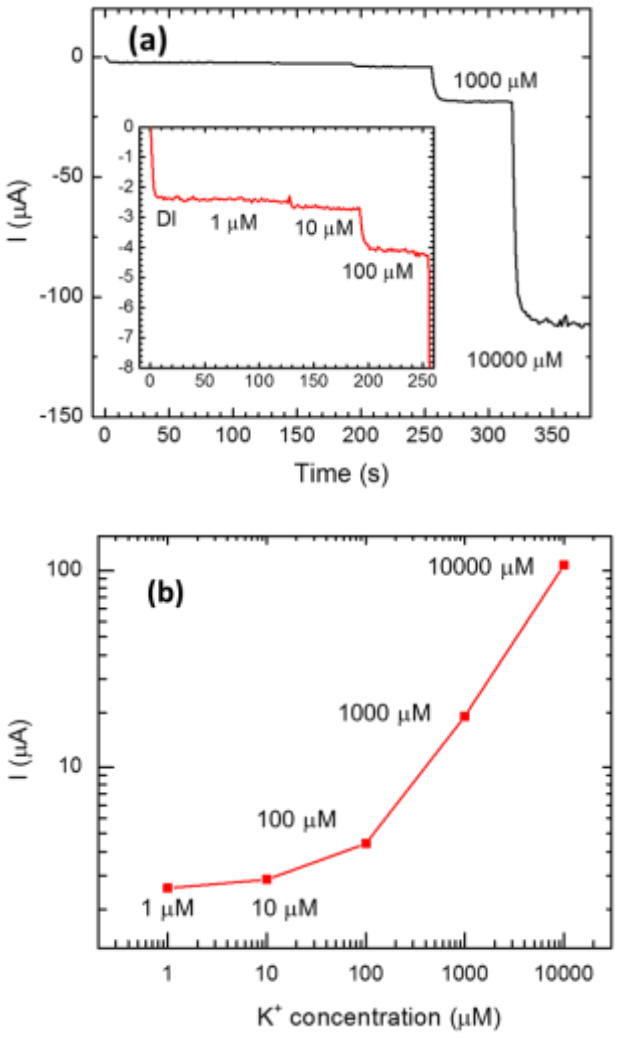

Figure 5.12 Graphene/Si Schottky junction ion sensing characteristics. (a). Device performance with constantly applied voltage (Vg =0). (b). Exponentially changing current with ion concentration change from 1 to 10^4 μM in full log scale.

range it increases not as fast as the higher range. This is assumed caused by parasitic resistance existing in the system, and it influences the device's performance stronger at the lower current range. In Figure 5.13, the sensor's I-V characteristics are plotted with the ion concentration change in the range of 0 μM and 1,000 μM. As seen in Fig. 4, the sensor showed extremely high sensing of potassium ion concentration in the range of 100 μM – 10,000 μM. A similar result was also shown for sodium ion sensing. Following the excellent results and ultra-high sensitivity, currently, the research is on the way to the selective detection of ions using ion-selective membrane coating.

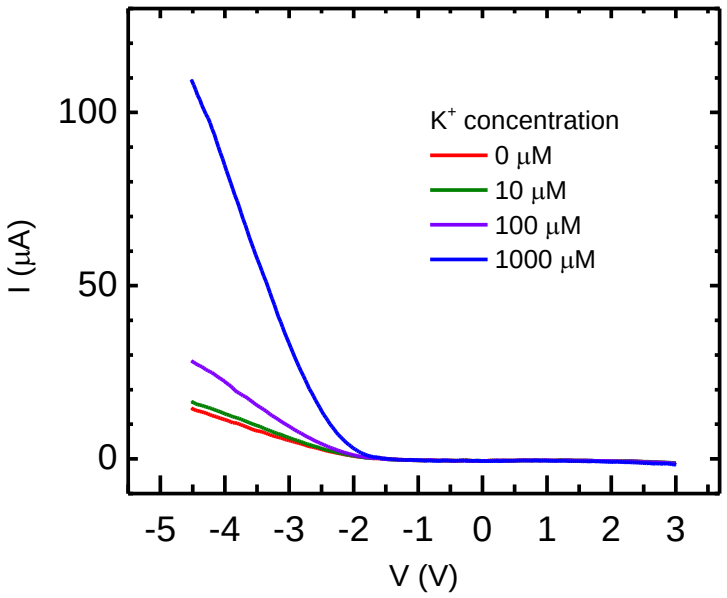

Figure 5.13 G-ISDiode I-V response to different ion concentration of analytic solution.

CHAPTER SIX

CONCLUSIONS AND FUTURE DIRECTIONS

6.1 Summary of This Work

Graphene is a new material discovered in 2004. Its exceptional material properties drew a huge interest in 2-dimensional (2D) research and started a new era of 2D materials and devices. In this dissertation, the study focused on graphene related investigation, research and development. It included graphene synthesis, characterization, investigation of its carrier transport properties, studies of its interaction with surface adsorbates, graphene-based device fabrication and characterization, its applications in ion detection and the feasibility in bio-technology.

To obtain high quality graphene for studying graphene's unique properties and graphene-based devices, a CVD system was built in the lab by installing a thermal furnace, pump, gas delivery tubes, gas cylinders, mass flow controllers, and pressure gauges. To control the process steps and monitor various parameters during the over 5 hours synthesis procedure, an automatic control panel was built using LabVIEW program. It integrated gas flow rate controlling, furnace controlling, temperature monitoring, chamber pressure monitoring, and recipe saving and loading functions. The automatic system greatly saved time and effort in conducting experiments and recording parameters during the whole process. With this home-built automatic CVD, we found the optimum synthesis condition and obtained high quality graphene. The obtained graphene was characterized using Raman spectroscopy, atomic force microscopy (AFM), Hall measurement, and X-ray photoelectron spectroscopy (XPS) as discussed in Chapter 2. From the characterization

result, we can determine that the synthesized graphene is high quality mono-layer graphene which is comparable to what reported in many other earlier studies.

Graphene's outstanding properties such as high mobility, low electronic noise, and high surface-to-volume ratio make it very attractive to explore its sensing applications. However, the change of carrier transport properties while the graphene interacting with surface adsorbates has not been investigated thoroughly. Most previously published studies are limited to observe and demonstrate graphene's sensing performance, present the response to an analytic absorbate in a single physical parameter's change such as in conductivity change, resistance change, or Dirac point shift. So, to provide a deeper insight into the graphene's interacting with molecular adsorbates, graphene's three most important electrical characteristics – carrier mobility, carrier concentration, and sheet conductivity – were collected simultaneously using Hall measurement system in Chapter 3. By investigating individual variations of three electrical properties while the graphene interacts with a typical donor (NH_3), acceptor (NO_2), and large molecules with very strong donating nature the study proposed a physical model explaining how the ionic adsorption effects on graphene's surface charge states and changes its electrical properties.

Recently, one of the hottest topics in graphene's sensing is sensing performance enhancement using surface functionalization method. In this study, a simple, clean, and very effective functionalization approach – plasma treatment functionalization was demonstrated. Plasma treatment has many advantages compared to other functionalization methods such as organic film coating, nanomaterial dispersion, or metal oxide decoration due to their processing complexity, bad uniformity. This technique showed a great

enhancing effect in graphene's sensitivity both in response magnitude and response time. To have a deep insight into the mechanism, its impact on carrier transport and on the molecular adsorption in graphene are investigated systematically using various analyzing tools.

With the knowledge obtained from graphene property investigation and its interaction mechanism with ionic adsorbates, a graphene-based ion sensitive field effect transistor was demonstrated in Chapter 4. A valinomycin-based membrane with excellent selectivity, stability and robustness were synthesized to apply on the device for exclusive K^+ ion selectivity. Fabricated GISFET device was packaged to be able to work at an aqueous environment and it demonstrated a highly sensitive and selective K^+ ion detecting performance. The sensor showed a high sensitivity of 61 ± 4.6 mV/pK in a wide range of ionic concentrations (1 μM – 20 mM) with good stability over a duration of two months. Also, it showed a negligible response to interfering Na^+ and Ca^{2+} ions owing to a good selectivity function of the ion selective membrane. To confirm its concept and potential, the same structure was fabricated on a flexible PET substrate, which exhibited very similar performance to the one fabricated on SiO_2/Si substrate.

In Chapter 5, in order to determine the applicability of GISFETs for implantable bio-sensing applications, several preliminary tests were conducted as well as an evaluation with real cells. GISFETs demonstrated good sensing performance in both tris-HCl solution and one with a very high Na^+ concentration without sensitivity degradation. Those background solutions were selected to mimic physiologic results that will be used in the real cell-based test. A real-cell based GISFETs performance evaluation was carried out

using cultured U251 MG human glioma cells and stimulation chemical A23187. A rise of K^+ ion concentration (50 μM) in the extracellular was detected, which confirms GISFETs bio-compatible sensing possibility for advanced applications in bio-technology in future. To explore the sensor's mass production possibility, a GISFETs array was designed and fabricated using CMOS compatible micro processing technique. The packaged sensor array chip on a chip carrier also showed a good sensing performance. Lastly, G-ISDiode was demonstrated based on graphene/Si Schottky junction. Unlike the GISFET's linear response to ion concentration G-ISDiode showed an exponential response to ionic concentration. This is due to exponential relation between device current to graphene's Fermi level shift. G-ISDiode has advantages in applications where an ultra-high sensitivity is required.

6.2 Future Outlook

6.2.1 Advanced GISFET Array Sensor on Flexible Substrate with Various Ion Selectivity

The GISFET sensor has demonstrated impressive performance in detecting K^+ ions with excellent sensitivity, selectivity, and repeatability. During the study and development, it has established a proper device structure and the stable fabrication process also indicated many potential applications. On the basis of these findings, advanced GISFET sensors with various ion selectivity can be developed as an extension of this research. First, a greater focus on ion selective membrane should be needed to develop selectivity for other ions such as Ca^{2+}, Na^+ or Mg^{2+}. In most of the physiological solution or human plasma, they also contain many other electrolytes involve in various important body functions.

Therefore, it can be very effective and useful if an ion sensor is capable of detecting various types of ion using just one drop of sample solution. As the final goal of this application is an implantable sensor in human body, a flexible substrate is preferable which is also in the interest of graphene's mechanical robustness and thin-film flexibility. The established fabrication technique using CMOS compatible process will be useful to develop GISFETs array on flexible substrate. Moreover, the sensor also can be combined with an integrated circuit chip having measurement and recording function as well as a wireless communication capability. By integrating all of these extra functions in addition to various ion sensing capabilities, the GISFETs array sensor on flexible substrate will be closer to the goal of implantable bio-sensing applications.

6.2.2 Direct Cell Growth on GISFET

In addition to bio assays of many physiological solutions, for a better resolution in dynamic biological behavior, continuous real-time observations of living cells' ionic variation are very important and necessary in many applications in fields of bio research, drug discovery, and medical diagnosis. For example, cell cycle analysis is a key drug discovery target and of significant importance for both cancer and regenerative medicine research. During cell growth, a cell undergoes series of development steps and by studying its dynamic changes we can obtain deep insight into cell cycle progression, cell differentiation, and drug treatment effects to cells. [132-133] Thus, the direct growth of cells on GISFETs will become another great application of what found in this research. To explore graphene's direct living cell analysis application, a preliminary study was carried out and the result was quite promising. We found that rat cardio myocytes cells can be

cultured directly on CVD grown graphene, and the number of cells didn't show any difference to the ones cultured on the glass. Additionally, a further investigation concluded that although the unique structural and electrical features of graphene alter the biophysical properties of the cells Ca2+ channels, a poly-l-lysine-and collagen-coated graphene restores its normal behavior. [30] With the basis of the knowledge gained from preliminary research, further work needs to be done to establish a reliable technique to grow cells directly on GISFETs array while without affecting sensors high sensing performance.

APPENDICES

Appendix A

Block Diagram of the LabVIEW Program for CVD Control Panel

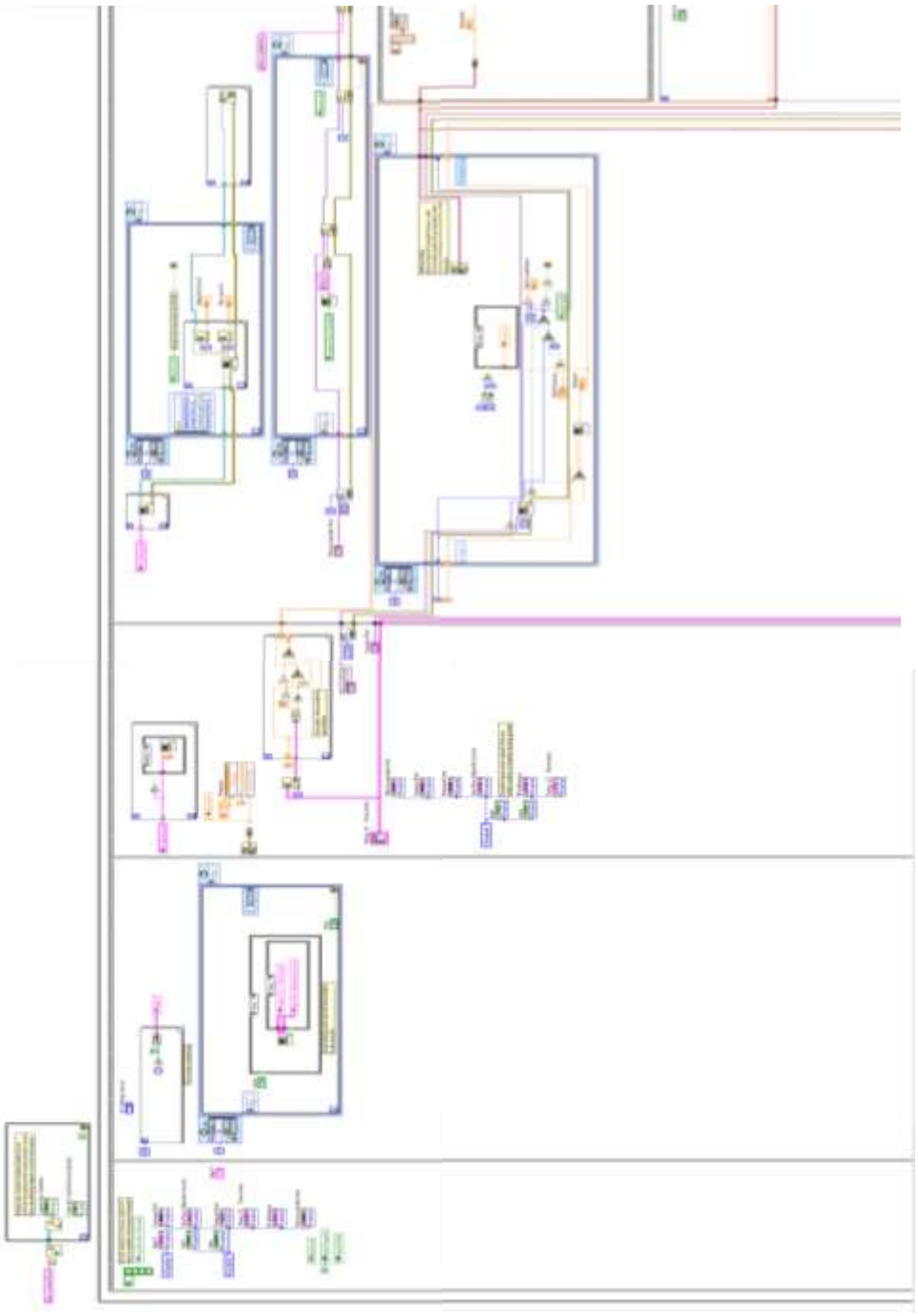

Figure A-1: The LabVIEW block diagram of Graphene CVD control panel. The full diagram is divided into 4 parts. This is the top left part.

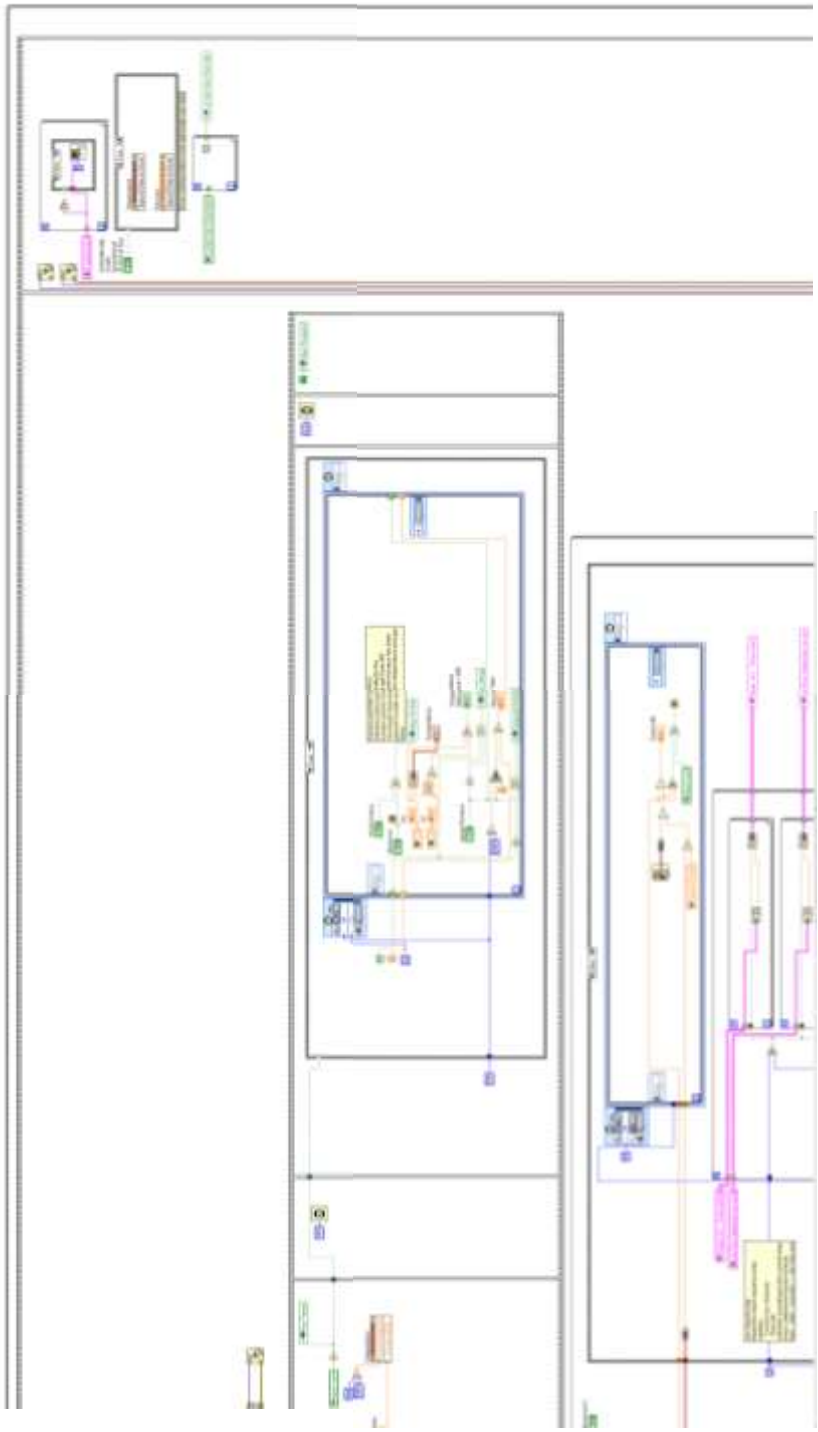

Figure A-2: The LabVIEW block diagram of Graphene CVD control panel. The full diagram is divided into 4 parts. This is the top right part.

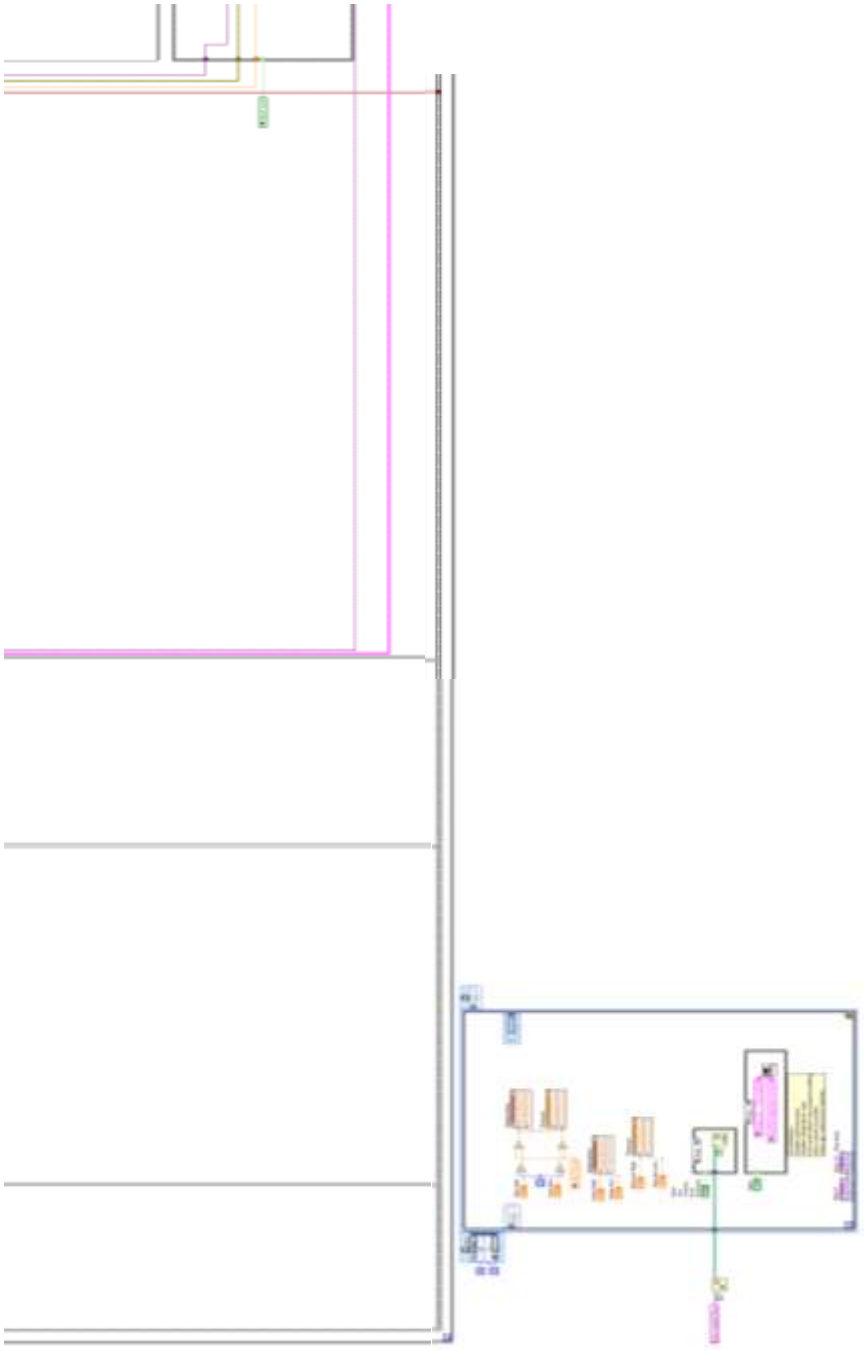

Figure A-3: The LabVIEW block diagram of Graphene CVD control panel. The full diagram is divided into 4 parts. This is the bottom left part.

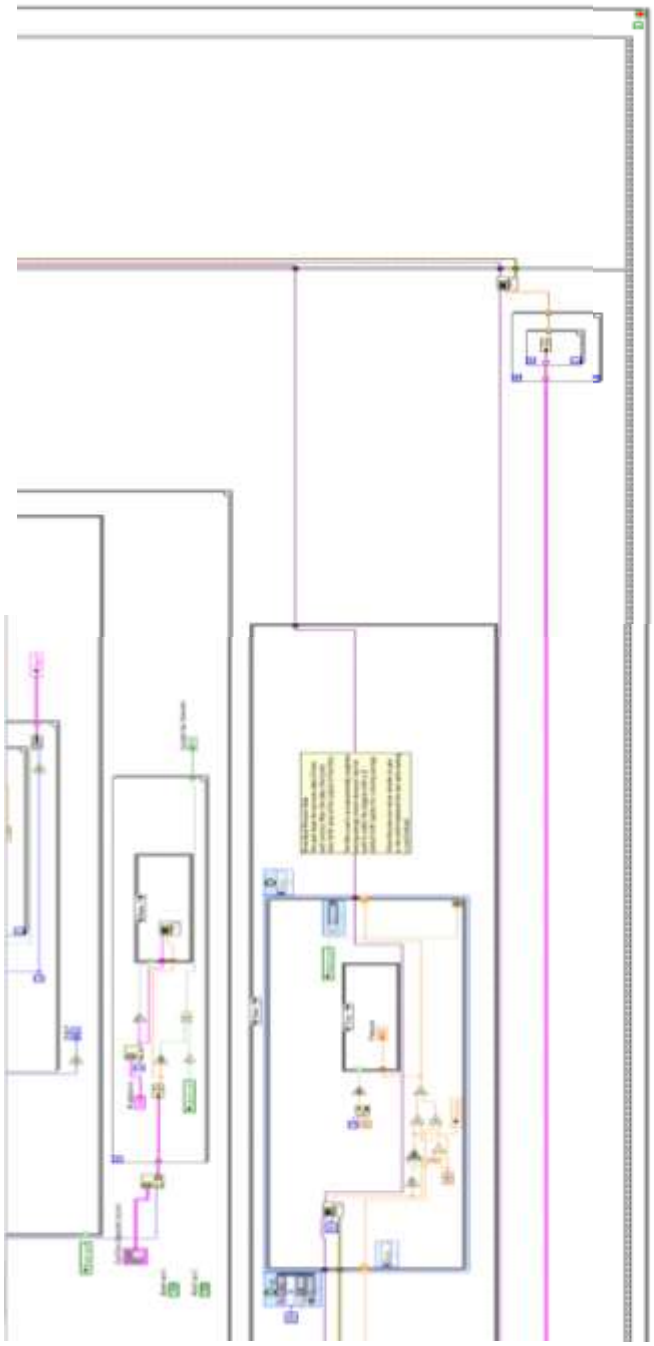

Figure A-4: The LabVIEW block diagram of Graphene CVD control panel. The full diagram is divided into 4 parts. This is the bottom right

Reference

[1] H. M. Pouran, “Engineered Nanomaterials in the Environment, their Potential Fate and Behaviour and Emerging Techniques to Measure Them,” no. October, 2018.

[2] I. D. and A. La Magna, “Coherent electron transport in quasi one-dimensional carbon-based systems,” *Eur. Phys. J. B*, vol. 81, no. 1, pp. 15–36, 2011.

[3] G. D. GF Dresselhaus, R Saito, *Raman Spectroscopy in Graphene Related Systems*. Wiley-VCH, Europe, 2011.

[4] S. G. Maffucci A, Maksimenko SA, Miano G, *Electrical Conductivity of Carbon Nanotubes: Modeling and Characterization.* Springer, Cham, 2017.

[5] J.-N. Fuchs and M. O. Goerbig, “Introduction to the Physical Properties of Graphene,” *Carbon N. Y.*, p. 69, 2008.

[6] D. Van Tuan, *Charge and Spin Transport in Disordered Graphene-Based Materials*. 2016.

[7] J.-N. Fuchs, “Dirac fermions in graphene and analogues: magnetic field and topological properties,” 2013.

[8] H. Jussila, H. Yang, N. Granqvist, and Z. Sun, “Surface plasmon resonance for characterization of large-area atomic-layer graphene film,” *Optica*, vol. 3, no. 2, p. 151, 2016.

[9] C. Lee, X. Wei, J. W. Kysar, and J. Hone, “Measurement of the elastic properties and intrinsic strength of monolayer graphene,” *Science*, vol. 321, no. July, pp. 385–388, 2008.

[10] Q. Bao and K. P. Loh, “Graphene photonics, plasmonics, and broadband optoelectronic devices,” *ACS Nano*, vol. 6, no. 5, pp. 3677–3694, 2012.

[11] S. Ghosh *et al.*, “Dimensional crossover of thermal transport in few-layer graphene,” *Nat. Mater.*, vol. 9, no. 7, pp. 555–558, 2010.

[12] R. Murali, Y. Yang, K. Brenner, T. Beck, and J. D. Meindl, “Breakdown current density of graphene nanoribbons,” *Appl. Phys. Lett.*, vol. 94, no. 24, pp. 2007–2010, 2009.

[13] M. Allen, V. Tung, and R. Kaner, “Honeycomb carbon -- A study of graphene,” *Am. Chem. Soc.*, vol. 110, pp. 132–145, 2010.

[14] M. Stoller, S. Park, Y. Zhu, J. An, and R. Ruoff, “Graphene-based ultracapacitors,” *Nano Lett.*, vol. 8, no. 10, pp. 3498–3502, 2008.

[15] K. Duan, L. Li, Y. Hu, and X. Wang, “Pillared graphene as an ultra-high sensitivity mass sensor,” *Sci. Rep.*, vol. 7, no. 1, pp. 1–8, 2017.

[16] A. Sakhaee-pour, A. Sakhaee-pour, M. T. Ahmadian, and A. Vafai, “Application of Single-Layered Graphene Sheets as Mass Sensors and Atomistic Dust Detectors Applications of single-layered graphene sheets as mass sensors and,” vol. 145, no. January 2008, pp. 168–172, 2016.

[17] A. Sakhaee-Pour, M. T. Ahmadian, and A. Vafai, “Potential application of single-layered graphene sheet as strain sensor,” *Solid State Commun.*, vol. 147, no. 7–8, pp. 336–340, 2008.

[18] C. L. Wong, M. Annamalai, Z. Q. Wang, and M. Palaniapan, “Characterization of nanomechanical graphene drum structures,” *J. Micromechanics Microengineering*,

vol. 20, no. 11, 2010.
[19] Z. H. Khan, A. R. Kermany, A. Öchsner, and F. Iacopi, “Mechanical and electromechanical properties of graphene and their potential application in MEMS,” *J. Phys. D. Appl. Phys.*, vol. 50, no. 5, 2017.
[20] X. Zang, Q. Zhou, J. Chang, Y. Liu, and L. Lin, “Graphene and carbon nanotube (CNT) in MEMS/NEMS applications,” *Microelectron. Eng.*, vol. 132, pp. 192–206, 2015.
[21] A. M. Van Der Zande *et al.*, “Large-scale arrays of single-layer graphene resonators,” *Nano Lett.*, vol. 10, no. 12, pp. 4869–4873, 2010.
[22] and S. D. Ming Zhou, Yueming Zhai, “Electrochemical Sensing and Biosensing Platform Based on Chemically Reduced Graphene Oxide,” *Anal. Chem.*, vol. 81, no. 4, pp. 5603–5613, 2009.
[23] A. Singh, M. A. Uddin, T. Sudarshan, and G. Koley, “Tunable reverse-biased graphene/silicon heterojunction Schottky diode sensor,” *Small*, vol. 10, no. 8, pp. 1555–1565, Apr. 2014.
[24] S. Basu and P. Bhattacharyya, “Recent developments on graphene and graphene oxide based solid state gas sensors,” *Sensors Actuators, B Chem.*, vol. 173, pp. 1–21, 2012.
[25] J. A. Phys, “Adsorption kinetics of ammonia sensing by graphene films decorated with.pdf,” vol. 094317, no. May 2012, 2017.
[26] N. Lei, P. Li, W. Xue, and J. Xu, “Simple graphene chemiresistors as pH sensors: Fabrication and characterization,” *Meas. Sci. Technol.*, vol. 22, no. 10, 2011.
[27] P. K. Ang, W. Chen, A. Thye, S. Wee, and K. P. Loh, “Solution-Gated Epitaxial Graphene as pH Sensor,” pp. 14392–14393, 2008.
[28] H. Li, Y. Zhu, M. S. Islam, M. A. Rahman, K. B. Walsh, and G. Koley, “Graphene field effect transistors for highly sensitive and selective detection of K+ions,” *Sensors Actuators, B Chem.*, vol. 253, pp. 759–765, 2017.
[29] N. Zhou, J. Li, H. Chen, C. Liao, and L. Chen, “A functional graphene oxide-ionic liquid composites-gold nanoparticle sensing platform for ultrasensitive electrochemical detection of Hg2+,” *Analyst*, vol. 138, no. 4, pp. 1091–1097, 2013.
[30] K. B. Walsh, H. Li, and G. Koley, “Graphene alters the properties of voltage-gated Ca2+ channels in rat cardiomyocytes,” *Biomed. Phys. Eng. Express*, vol. 4, no. 6, 2018.
[31] M. Zhang, B. C. Yin, X. F. Wang, and B. C. Ye, “Interaction of peptides with graphene oxide and its application for real-time monitoring of protease activity,” *Chem. Commun.*, vol. 47, no. 8, pp. 2399–2401, 2011.
[32] P. A. Rasheed and N. Sandhyarani, “Graphene-DNA electrochemical sensor for the sensitive detection of BRCA1 gene,” *Sensors Actuators, B Chem.*, vol. 204, pp. 777–782, 2014.
[33] R. Yue, Q. Lu, and Y. Zhou, “A novel nitrite biosensor based on single-layer graphene nanoplatelet-protein composite film,” *Biosens. Bioelectron.*, vol. 26, no. 11, pp. 4436–4441, 2011.
[34] K. Xu, X. Meshik, B. M. Nichols, E. Zakar, M. Dutta, and M. A. Stroscio, “Graphene- and aptamer-based electrochemical biosensor,” *Nanotechnology*, vol.

25, no. 20, 2014.
[35] L. Wang, Y. Zhang, A. Wu, and G. Wei, “Designed graphene-peptide nanocomposites for biosensor applications: A review,” *Anal. Chim. Acta*, vol. 985, pp. 24–40, 2017.
[36] V. C. Sanchez, A. Jachak, R. H. Hurt, and A. B. Kane, “Biological interactions of graphene-family nanomaterials: An interdisciplinary review,” *Chem. Res. Toxicol.*, vol. 25, no. 1, pp. 15–34, 2012.
[37] M. Savchak *et al.*, “Highly Conductive and Transparent Reduced Graphene Oxide Nanoscale Films via Thermal Conversion of Polymer-Encapsulated Graphene Oxide Sheets,” *ACS Appl. Mater. Interfaces*, vol. 10, no. 4, pp. 3975–3985, 2018.
[38] H. S. Bhuyan MS, Uddin MN, Islam MM, Bipasha FA, “Synthesis of graphene,” *Int. Nano Lett.*, vol. 6, no. 2, pp. 65–83, 2016.
[39] H. C. Lee *et al.*, “Review of the synthesis, transfer, characterization and growth mechanisms of single and multilayer graphene,” *RSC Adv.*, vol. 7, no. 26, pp. 15644–15693, 2017.
[40] L. Ci *et al.*, “Graphene shape control by multistage cutting and transfer,” *Adv. Mater.*, vol. 21, no. 44, pp. 4487–4491, 2009.
[41] A. S. P. Chang *et al.*, “Electrostatic Force Assisted Exfoliation of Prepatterned Few-Layer Graphenes into Device Sites,” *Nano Lett.*, vol. 9, no. 2, pp. 919–919, 2009.
[42] X. Liang, Z. Fu, and S. Y. Chou, “Graphene transistors fabricated via transfer-printing in device active-areas on large wafer,” *Nano Lett.*, vol. 7, no. 12, pp. 3840–3844, 2007.
[43] A. B. Bourlinos, V. Georgakilas, R. Zboril, T. A. Sterioti, and A. K. Stubos, “Liquid-Phase Exfoliation of Graphite Towards Solubilized Graphenes,” *Small*, vol. 5, no. 16, pp. 1841–1845, 2009.
[44] R. K. Singh, R. Kumar, and D. P. Singh, “Graphene oxide: Strategies for synthesis, reduction and frontier applications,” *RSC Adv.*, vol. 6, no. 69, pp. 64993–65011, 2016.
[45] H. Bai, C. Li, and G. Shi, “Functional composite materials based on chemically converted graphene,” *Adv. Mater.*, vol. 23, no. 9, pp. 1089–1115, 2011.
[46] Y. Chen, X. L. Gong, and J. G. Gai, “Progress and Challenges in Transfer of Large-Area Graphene Films,” *Adv. Sci.*, vol. 3, no. 8, pp. 1–15, 2016.
[47] R. S. Ruoff, X. Li, W. Cai, and L. Colombo, “Evolution of graphene growth on Ni and Cu by carbon isotope labeling,” *Nano Lett.*, vol. 9, no. 12, pp. 4268–4272, 2009.
[48] M. S. Dresselhaus, A. Jorio, M. Hofmann, G. Dresselhaus, and R. Saito, “Perspectives on carbon nanotubes and graphene Raman spectroscopy,” *Nano Lett.*, vol. 10, no. 3, pp. 751–758, 2010.
[49] F. Tuinstra and J. L. Koenig, “Raman Spectrum of Graphite,” *J. Chem. Phys.*, vol. 53, no. 3, pp. 1126–1130, 1970.
[50] F. M. Etzler and J. Drelich, “Developments in Surface Contamination and Cleaning,” R. Kohli and K. . Mittal, Eds. William Andrew Publishing, 2011, p. 307.
[51] L. M. Malard, M. A. Pimenta, G. Dresselhaus, and M. S. Dresselhaus, “Raman spectroscopy in graphene,” *Phys. Rep.*, vol. 473, no. 5–6, pp. 51–87, 2009.
[52] C. J. Shearer, A. D. Slattery, A. J. Stapleton, J. G. Shapter, and C. T. Gibson,

"Accurate thickness measurement of graphene," *Nanotechnology*, vol. 27, no. 12, 2016.
[53] M. A. Uddin, Y. Zhu, A. Singh, H. Li, M. S. Islam, and G. Koley, "Effect of epoxy exposure on the electronic properties of graphene," *J. Phys. D. Appl. Phys.*, vol. 49, no. 46, 2016.
[54] D. K. Schroder, *Semiconductor Material and Device Characterization*, 2nd Editio. New York: John Wiley & Sons, 1998.
[55] L. J. van der PAUW, "A method of measuring the resistivity and hall coefficient on lamellae of arbitrary shape," vol. 20, no. I, pp. 220–224, 1958.
[56] H. Konno, "X-ray Photoelectron Spectroscopy," in *Materials Science and Engineering of Carbon*, Elsevier, 2016, p. 153.
[57] R. Al-Gaashani, A. Najjar, Y. Zakaria, S. Mansour, and M. A. Atieh, "XPS and structural studies of high quality graphene oxide and reduced graphene oxide prepared by different chemical oxidation methods," *Ceram. Int.*, vol. 45, no. 11, pp. 14439–14448, 2019.
[58] Y. Shao, J. Wang, H. Wu, J. Liu, I. A. Aksay, and Y. Lin, "Graphene based electrochemical sensors and biosensors: A review," *Electroanalysis*, vol. 22, no. 10, pp. 1027–1036, 2010.
[59] R. J. Young, I. A. Kinloch, L. Gong, and K. S. Novoselov, "The mechanics of graphene nanocomposites: A review," *Compos. Sci. Technol.*, vol. 72, no. 12, pp. 1459–1476, 2012.
[60] X. Li, M. Rui, J. Song, Z. Shen, and H. Zeng, "Carbon and Graphene Quantum Dots for Optoelectronic and Energy Devices: A Review," *Adv. Funct. Mater.*, vol. 25, no. 31, pp. 4929–4947, 2015.
[61] X. Zhou, J. Qiao, L. Yang, and J. Zhang, "A review of graphene-based nanostructural materials for both catalyst supports and metal-free catalysts in PEM fuel cell oxygen reduction reactions," *Adv. Energy Mater.*, vol. 4, no. 8, pp. 1–25, 2014.
[62] F. Schedin *et al.*, "Detection of individual gas molecules adsorbed on graphene," *Nat. Mater.*, vol. 6, no. 9, pp. 652–655, 2007.
[63] M. A. Uddin, G. Koley, A. Singh, K. Daniels, and T. Vogt, "Impedance spectroscopic analysis of nanoparticle functionalized graphene/p-Si Schottky diode sensors," *Jpn. J. Appl. Phys.*, vol. 55, no. 11, 2016.
[64] H. Xu, Y. Chen, J. Zhang, and H. Zhang, "Investigating the mechanism of hysteresis effect in graphene electrical field device fabricated on SiO2 substrates using raman spectroscopy," *Small*, vol. 8, no. 18, pp. 2833–2840, 2012.
[65] M. Ishigami, J. H. Chen, W. G. Cullen, M. S. Fuhrer, and E. D. Williams, "Atomic structure of graphene on SiO 2," *Nano Lett.*, vol. 7, no. 6, pp. 1643–1648, 2007.
[66] K. Morokuma, "Why Do Molecules Interact ? The Origin of Electron Donor-Acceptor Complexes , Hydrogen Bonding , and Proton Affinity," vol. 1325, no. 1973, pp. 294–300, 1977.
[67] O. Leenaerts, B. Partoens, and F. M. Peeters, "Adsorption of H 2 O, NH 3 , CO, NO 2 , and NO on graphene: A first-principles study," no. 2, pp. 1–6, 2020.
[68] W. K. Nomani, V. Shields, G. Tompa, N. Sbrockey, M. G. Spencer, and R. A. Webb,

"Correlated conductivity and work function changes in epitaxial graphene Correlated conductivity and work function changes in epitaxial graphene," vol. 092113, no. 2012, pp. 1–5, 2017.

[69] A. A. F. Novoselov, A. K. Geim, S. V. Morozov, D. Jiang, Y. Zhang, S. V. Dubonos, I. V. Grigorieva, "Electric Field Effect in Atomically Thin Carbon Films," vol. 666, no. 2004, pp. 666–669, 2013.

[70] A. K. Singh *et al.*, "Electrically tunable molecular doping of graphene," *Appl. Phys. Lett.*, vol. 102, no. 4, 2013.

[71] S. Adam, E. H. Hwang, V. M. Galitski, and S. Das Sarma, "A self-consistent theory for graphene transport," *Proc. Natl. Acad. Sci.*, vol. 104, no. 47, pp. 18392–18397, 2007.

[72] J. H. Chen, C. Jang, S. Xiao, M. Ishigami, and M. S. Fuhrer, "Intrinsic and extrinsic performance limits of graphene devices on SiO 2," *Nat. Nanotechnol.*, vol. 3, no. 4, pp. 206–209, 2008.

[73] S. Z. Liang, G. Chen, A. R. Harutyunyan, and J. O. Sofo, "Screening of charged impurities as a possible mechanism for conductance change in graphene gas sensing," *Phys. Rev. B - Condens. Matter Mater. Phys.*, vol. 90, no. 11, pp. 1–7, 2014.

[74] J. Mach, J. H. , P Procházka, M Bartošík , D Nezval, J Piastek, and L. K. and T. Š. V Švarc, M Konecˇný, "Electronic transport properties of graphene doped by gallium," *Nanotechnology*, vol. 28, no. 41, 2017.

[75] T. Kuila, S. Bose, P. Khanra, A. K. Mishra, N. H. Kim, and J. H. Lee, "Recent advances in graphene-based biosensors," *Biosens. Bioelectron.*, vol. 26, no. 12, pp. 4637–4648, 2011.

[76] E. Singh, M. Meyyappan, and H. S. Nalwa, "Flexible Graphene-Based Wearable Gas and Chemical Sensors," *ACS Appl. Mater. Interfaces*, vol. 9, no. 40, pp. 34544–34586, 2017.

[77] I. J. Luxmoore, P. Q. Liu, P. Li, J. Faist, and G. R. Nash, "Graphene-Metamaterial Photodetectors for Integrated Infrared Sensing," *ACS Photonics*, vol. 3, no. 6, pp. 936–941, 2016.

[78] E. Cazalas, B. K. Sarker, I. Childres, Y. P. Chen, and I. Jovanovic, "Modulation of graphene field effect by heavy charged particle irradiation," *Appl. Phys. Lett.*, vol. 109, no. 25, 2016.

[79] W. Fu *et al.*, "Graphene transistors are insensitive to pH changes in solution," *Nano Lett.*, vol. 11, no. 9, pp. 3597–3600, 2011.

[80] M. A. Uddin, A. K. Singh, T. S. Sudarshan, and G. Koley, "Functionalized graphene/silicon chemi-diode H2sensor with tunable sensitivity," *Nanotechnology*, vol. 25, no. 12, 2014.

[81] X. Wang, S. M. Tabakman, and H. Dai, "Atomic layer deposition of metal oxides on pristine and functionalized graphene," *J. Am. Chem. Soc.*, vol. 130, no. 26, pp. 8152–8153, 2008.

[82] T. Kuila, S. Bose, A. K. Mishra, P. Khanra, N. H. Kim, and J. H. Lee, "Chemical functionalization of graphene and its applications," *Prog. Mater. Sci.*, vol. 57, no. 7, pp. 1061–1105, 2012.

[83] H. Li, X. Han, A. S. Childress, A. M. Rao, and G. Koley, “Investigation of carrier density and mobility variations in graphene caused by surface adsorbates,” *Phys. E Low-Dimensional Syst. Nanostructures*, vol. 107, no. November 2018, pp. 96–100, 2019.
[84] I. Childres, L. A. Jauregui, J. Tian, and Y. P. Chen, “Effect of oxygen plasma etching on graphene studied using Raman spectroscopy and electronic transport measurements,” *New J. Phys.*, vol. 13, 2011.
[85] M. M. Lucchese *et al.*, “Quantifying ion-induced defects and Raman relaxation length in graphene,” *Carbon N. Y.*, vol. 48, no. 5, pp. 1592–1597, 2010.
[86] B. K. Daas, G. Koley, and T. S. Sudarshan, “Molecular Doping on Epitaxial Graphene by Gaseous Surface Adsorbents : Influence of Interband Scattering,” vol. 216, no. 9, pp. 29–37, 2017.
[87] A. Nourbakhsh *et al.*, “Bandgap opening in oxygen plasma-treated graphene,” *Nanotechnology*, vol. 21, no. 43, 2010.
[88] W. Choi *et al.*, “Relaxation of Plasma Carriers in Graphene: An Approach by Frequency-Dependent Optical Conductivity Measurement,” *Adv. Opt. Mater.*, vol. 6, no. 14, pp. 1–7, 2018.
[89] A. Goto, G. Takeuchi, R. Yamachi, T. Tanaka, T. Takahashi, and K. Uchida, “Impact of hydrogen on carrier mobility and concentration in graphene decorated with Pd nanoparticle,” *ECS Trans.*, vol. 72, no. 14, pp. 7–12, 2016.
[90] M. Z. Iqbal, A. Rehman, and S. Siddique, “Ultraviolet-light-driven carrier density modulation of graphene based field effect transistors under oxygen- and argon atmosphere,” *Appl. Surf. Sci.*, vol. 451, pp. 40–44, 2018.
[91] G. Lee, G. Yang, A. Cho, J. W. Han, and J. Kim, “Defect-engineered graphene chemical sensors with ultrahigh sensitivity,” *Phys. Chem. Chem. Phys.*, vol. 18, no. 21, pp. 14198–14204, 2016.
[92] Z. Zhang *et al.*, “Study on adsorption and desorption of ammonia on graphene,” *Nanoscale Res. Lett.*, vol. 10, no. 1, 2015.
[93] “Fluid, Electrolyte, and Acid-base Balance,” in *Anatomy and physiology*, OpenStax, 2013.
[94] S. I. Xu H, Martinoia E, “Organellar Channels and Transporters,” *Cell Calcium*, vol. 58, no. 1, pp. 1–10, 2015.
[95] H. R. Polder, M. Weskamp, K. Linz, and R. Meyer, “Voltage-clamp and patch-clamp techniques,” in *Practical Methods in Cardiovascular Research*, 2005, pp. 272–323.
[96] C. JJ, “Targeting Ion Channels for Drug Discovery,” *Discov. Med.*, vol. 9, no. 46, pp. 253–260, 2010.
[97] P. Bergveld, “Development , Operation , and Application of the Tool for Electrophysiology,” *IEEE Trans. Biomed. Eng.*, vol. 19, no. 5, pp. 342–351, 1972.
[98] P. Bergveld, “Development of an ion-sensitive solid-state device for neurophysiological measurements,” *IEEE Trans. Biomed. Eng.*, vol. 21, no. January, pp. 70–71, 1970.
[99] P. Bergveld, “Thirty years of ISFETOLOGY: What happened in the past 30 years and what may happen in the next 30 years,” *Sensors Actuators B Chem.*, vol. 88, no.

1, pp. 1–20, 2003.
[100] S. Chen *et al.*, "A graphene field-effect capacitor sensor in electrolyte," *Appl. Phys. Lett.*, vol. 101, no. 15, 2012.
[101] J. L. Qi, K. Nagashio, T. Nishimura, and A. Toriumi, "The crystal orientation relation and macroscopic surface roughness in hetero-epitaxial graphene grown on Cu/mica," *Nanotechnology*, vol. 25, no. 18, 2014.
[102] C. C. Cid, J. Riu, A. Maroto, and F. X. Rius, "Ion-sensitive field effect transistors using carbon nanotubes as the transducing layer.," *Analyst*, vol. 133, no. 8, pp. 1001–4, 2008.
[103] L. Y. Heng and E. A. H. Hall, "Methacrylic-acrylic polymers in ion-selective membranes: Achieving the right polymer recipe," *Anal. Chim. Acta*, vol. 403, no. 1–2, pp. 77–89, 2000.
[104] C. Z. Lai, M. M. Joyer, M. A. Fierke, N. D. Petkovich, A. Stein, and P. Bühlmann, "Subnanomolar detection limit application of ion-selective electrodes with three-dimensionally ordered macroporous (3DOM) carbon solid contacts," *J. Solid State Electrochem.*, vol. 13, no. 1, pp. 123–128, 2009.
[105] R. He and T. Kyu, "Effect of Plasticization on Ionic Conductivity Enhancement in Relation to Glass Transition Temperature of Crosslinked Polymer Electrolyte Membranes," *Macromolecules*, vol. 49, no. 15, pp. 5637–5648, 2016.
[106] T. Masadome, T. T. Kie, S. Wakida, and K. Higashi, "Evaluation of Effect of Additive Salts on Response of Potassium-selective Neutral Carrier Based Electrodes Using Ion-sensitive Field-effect Transistor," *Anal. Commun.*, vol. 34, no. 12, pp. 389–390, 1997.
[107] O. H. LeBlanc and W. T. Grubb, "Long-lived potassium ion selective polymer membrane electrode," *Anal. Chem.*, vol. 48, no. 12, pp. 1658–1660, 1976.
[108] M. Siskin, "Stability of sodium and potassium complexes of valinomycin," *J. Anal. Appl. Pyrolysis*, vol. 287, pp. 173–196, 1983.
[109] T. E. Andreoli, "The Effect of Valinomycin on the Ionic Permeability of Thin Lipid Membranes," *J. Gen. Physiol.*, vol. 50, no. 11, pp. 2527–2545, 1967.
[110] B. Wang, K. L. Liddell, J. Wang, B. Koger, C. D. Keating, and J. Zhu, "Oxide-on-graphene field effect bio-ready sensors," *Nano Res.*, vol. 7, no. 9, pp. 1263–1270, 2014.
[111] I. Fakih, S. Sabri, F. Mahvash, M. Nannini, M. Siaj, and T. Szkopek, "Large area graphene ion sensitive field effect transistors with tantalum pentoxide sensing layers for pH measurement at the Nernstian limit," *Appl. Phys. Lett.*, vol. 105, no. 8, 2014.
[112] W. Fu *et al.*, "High mobility graphene ion-sensitive field-effect transistors by noncovalent functionalization.," *Nanoscale*, vol. 5, no. 24, pp. 12104–10, 2013.
[113] D. W. Boukhvalov and M. I. Katsnelson, "Chemical functionalization of graphene," *J. Phys. Condens. Matter*, vol. 21, no. 34, 2009.
[114] J. Ye *et al.*, "Accessing the transport properties of graphene and its multilayers at high carrier density," *Proc. Natl. Acad. Sci. U. S. A.*, vol. 108, no. 32, pp. 13002–13006, 2011.
[115] T. K. Truong *et al.*, "Reduced graphene oxide field-effect transistor with indium tin oxide extended gate for proton sensing," *Curr. Appl. Phys.*, vol. 14, no. 5, pp. 738–

743, 2014.
[116] P. F. Cmos, N. Nikkhoo, S. Member, P. G. Gulak, S. Member, and K. Maxwell, “Rapid Detection of E . coli Bacteria Using,” vol. 7, no. 5, pp. 621–630, 2013.
[117] K. B. Walsh, N. DeRoller, Y. Zhu, and G. Koley, “Application of ion-sensitive field effect transistors for ion channel screening,” *Biosens. Bioelectron.*, vol. 54, pp. 448–454, 2014.
[118] N. A. and A. B. C. Jimenez, A. Bratov, “ISFET based sensors: fundamentals and applications,” *Encycl. Sens.*, pp. 151–196, 2006.
[119] Z. Chen and J. Appenzeller, “Mobility extraction and quantum capacitance impact in high performance graphene field-effect transistor devices,” *Tech. Dig. - Int. Electron Devices Meet. IEDM*, no. L, pp. 2–5, 2008.
[120] G. Schwartz *et al.*, “Flexible polymer transistors with high pressure sensitivity for application in electronic skin and health monitoring.,” *Nat. Commun.*, vol. 4, no. May, p. 1859, 2013.
[121] O. Devinsky, A. Vezzani, S. Najjar, N. C. De Lanerolle, and M. A. Rogawski, “Glia and epilepsy: Excitability and inflammation,” *Trends Neurosci.*, vol. 36, no. 3, pp. 174–184, 2013.
[122] M. Rubart and D. P. Zipes, “Mechanisms of sudden cardiac death,” *J. Clin. Invest.*, vol. 115, no. 9, pp. 2305–2315, 2005.
[123] A. Topkar and R. Lal, “Effect of electrolyte exposure on silicon dioxide in electrolyte-oxide-semiconductor structures,” *Thin Solid Films*, vol. 232, no. 2, pp. 265–270, 1993.
[124] S. Libertino, S. Conoci, A. Scandurra, and C. Spinella, “Biosensor integration on Si-based devices: Feasibility studies and examples,” *Sensors Actuators, B Chem.*, vol. 179, pp. 240–251, 2013.
[125] R. A. Durst and B. R. Staples, “Tris-tris-HCl: a standard buffer for use in the physiologic pH range.,” *Clin. Chem.*, vol. 18, no. 3, pp. 206–208, 1972.
[126] A. Ds, F. Mw, and K. Sd, “Receptor Binding Assays for HTS and Drug Discovery Flow Chart of Steps to Assay Development for SPA Format Flow Chart of Steps to Assay Development for Filter Format,” no. Md, pp. 1–27, 2017.
[127] W. Zheng, R. H. Spencer, and L. Kiss, “High Throughput Assay Technologies for Ion Channel Drug Discovery,” in *Assay and Drug development technologies*, vol. 2, no. 5, 2004.
[128] S. M. Sze and K. K. Ng, *Physics of Semiconductor Devices*. John Wiley & Sons, 2006.
[129] A. K. Singh, “TUNABLE GRAPHENE CHEM-FET AND GRAPHENE/SI HETEROJUNCTION CHEMI-DIODE SENSORS.”
[130] S. Tongay, M. Lemaitre, X. Miao, B. Gila, B. R. Appleton, and A. F. Hebard, “Rectification at graphene-semiconductor interfaces: Zero-gap semiconductor-based diodes,” *Phys. Rev. X*, vol. 2, no. 1, pp. 1–10, 2012.
[131] A. Di Bartolomeo, “Graphene Schottky diodes: An experimental review of the rectifying graphene/semiconductor heterojunction,” *Phys. Rep.*, vol. 606, no. June 2015, pp. 1–58, 2016.
[132] P. S. Rabinovitch, R. M. Torres, and D. Engel, “Simultaneous cell cycle analysis

and two-color surface immunofluorescence using 7-amino-actinomycin D and single laser excitation: Applications to study of cell activation and the cell cycle of murine Ly-1 B cells," *J. Immunol.*, vol. 136, no. 8, pp. 2769–2885, 1986.

[133] J. Gerdes, H. Lemke, H. Baisch, H. Wacker, U. Schwab, and H. Stein, "Cell cycle analysis of a cell proliferation-associated human nuclear antigen defined by the monoclonal antibody Why The JI ? Submit online . • Rapid Reviews ! 30 days * from submission to initial decision" *J. Immunol.*, vol. 133, no. 4, pp. 1710–1715, 1984.